Universidade de São Paulo
Instituto de Física

Modelagem da evolução de cenários de plasmas no tokamak TCABR

Yuri Peres Asnis

Orientador: Prof. Dr. Gustavo Paganini Canal

Dissertação de mestrado apresentada ao Instituto de Física como requisito parcial para a obtenção do título de Mestre em Ciências.

Banca Examinadora:

Prof. Dr. Gustavo Paganini Canal (Instituto de Física da Universidade de São Paulo)
Dr. Vinícius Njaim Duarte (Laboratório de Física de Plasmas de Princeton)
Dr. Diego Sales de Oliveira (Centro Suíço de Plasma)

São Paulo
2023

FICHA CATALOGRÁFICA
Preparada pelo Serviço de Biblioteca e Informação
do Instituto de Física da Universidade de São Paulo

Asnis , Yuri Peres

Modelagem da evolução de cenários de plasma no tokamak TCABR/ Modeling the evolution of plasma scenarios in the TCABR tokamak. São Paulo, 2023.

Dissertação (Mestrado) - Universidade de São Paulo. Instituto de Física. Depto. de Física Aplicada.

Orientador: Prof. Dr. Gustavo Paganini Canal

Área de Concentração: Física de Plasmas.

Unitermos: 1. Física de Plasmas; 2. Magnetohidrodinâmica; 3. Equilíbrio MHD; 4. Tokamak; 5. Computação numérica.

USP/IF/SBI-032/2023

University of São Paulo
Physics Institute

Modeling the evolution of plasma scenarios in the TCABR tokamak

Yuri Peres Asnis

Supervisor: Prof. Dr. Gustavo Paganini Canal

Dissertation submitted to the Physics Institute of the University of São Paulo in partial fulfillment of the requirements for the degree of Master of Science.

Examining Committee:

Prof. Dr. Gustavo Paganini Canal (Institute of Physics of the University of São Paulo)
Dr. Vinícius Njaim Duarte (Princeton Plasma Physics Laboratory)
Dr. Diego Sales de Oliveira (Swiss Plasma Center)

São Paulo
2023

Let everything happen to you
Beauty and terror
Just keep going
No feeling is final.
- *Rainer Maria Rilke*

Essa dissertação é dedicada à José Augusto Weber...

Agradecimentos

Essa dissertação de mestrado não existiria sem o suporte, ajuda e contribuição daqueles que fazem parte da minha vida e do meu dia a dia. Aqui, agradeço

- À minha familia – em especial aos meus pais Laerte e Valéria e ao meu irmão Gabriel Zissi – por simplesmente serem a base e a razão da minha existência. Obrigado por me ensinarem que, para ser feliz, basta apenas um pedacinho de papel.
- Ao meu orientador e amigo, professor Gustavo Paganini Canal, por estar desde 2018 comigo nessa empreitada científica. Gustavo é um físico tão brilhante que a cada conversa, não importa o quão complexo seja o tema em discussão, ele sempre preza primeiro pela intuição física, e depois aos cálculos. Às vezes acho que ele também é formado em marketing, só não conta pra ninguém.
- À toda a equipe do TCABR, em especial ao André Bouzan – que foi meu companheiro de mesa durante o período pós pandemia e que me proporcionou uma visão muito maior do lado experimental e prático de um laboratório. Vocês sabiam que até a cabeça do parafuso precisa ser modelada? Eu não sabia. Então de agora em diante toda vez que eu for comprar um parafuso, eu vou ver o rosto do André. Agradeço também ao Felipe Salvador, o chefinho, pelas inúmeras contribuições e discussões sobre o projeto.
- Às demais pessoas que também tiveram uma parte importante nessa jornada. Menciono aqui Ben-Hur Martins Portella e Júlia Schenatto, uma amizade que surgiu da disciplina de eletrodinâmica clássica durante meu primeiro semestre do mestrado (ainda em pandemia) e que sempre os guardarei dentro do peito. E à Adriana Testa, por ter me acolhido em sua casa e tornado a minha vivência em São Paulo mais agradável.
- À banca avaliadora, por ter aceitado ler e arguir sobre o projeto.
- Por fim, agradeço à Comissão Nacional de Energia Nuclear, agência que financiou este presente trabalho através do Processo 01341.001295/2021-76.

I am guided by the knowledge that everything I am doing, I am doing for the well-being of the human kind.

Abstract

A significant upgrade is being designed for the TCABR tokamak - a machine operated at the Institute of Physics of the University of São Paulo, Brazil. As part of this upgrade, two additional poloidal field (PF) coils will be installed, increasing its number from 14 to 16. This will allow TCABR to create plasmas with a large variety of shapes, including wall-limited plasmas with significant elongation, positive and negative triangularity, and squareness, as well as diverted plasmas such as single-nulls, double-nulls and snowflakes. The creation of a plasma with a particular shape requires the prior knowledge of the evolution of each magnetic coil current. In this work, we present the development of a computational model that calculates these coil current evolution's based on a small set of input parameters that must be given at specified values of time, such as plasma current, normalised beta, the location of the last closed flux surface, and constraint points such as X-points. This model, therefore, allows for the design of the plasma evolution during the entire discharge. The core of this model consists of circuit equations that represent the electromagnetic coupling between magnetic coils, vacuum vessel and the plasma. The inclusion of the vacuum vessel in the modeling allows for a more realistic prediction of the toroidal electric field attenuation in the plasma region, the self-consistent calculation of induced vessel currents and their impact on the plasma shape, which must be somehow compensated by the PF coil current. Moreover, this model, coupled with an MHD equilibrium code, enables the generation of synthetic MHD equilibria for TCABR, ensuring a better estimation of the time evolution of each coil current and voltage. These MHD equilibria also account self-consistently for the presence of the bootstrap current. Eight plasma scenarios were designed and it was observed that to maintain a flat top plasma current of up to I_p = 110 kA for up to 1 s, the OH and the PF coils power supplies will have to operate in the four quadrants of a current-voltage operational space and provide voltages and currents, respectively, up to ±2.3 kV/±24 kA, for controlling the plasma current, and up to ±300 V/±9.0 kA, for controlling plasma position and shape.

Key words: Plasma Physics; Magnetohydrodynamics; MHD equilibrium; Tokamaks; Numerical computation.

Resumo

Uma modernização significativa do tokamak TCABR - uma máquina operada pelo Instituto de Física da Universidade de São Paulo, está sendo projetada. Parte dessa modernização está na instalação de duas bobinas de campo poloidal (PF) adicionais, aumentando esse número de 14 para 16. Isso permitirá ao TCABR criar plasmas com uma vasta variedade de formatos, incluindo plasmas limitados pela parede bem como plasmas com desviadores com pontos-X únicos, pontos-X duplos e desviadores *snowflakes*. A criação de um plasma com um determinado formato requer o conhecimento prévio da evolução das correntes elétricas em cada uma das bobinas magnéticas. Neste trabalho, apresentamos o desenvolvimento de um modelo computacional que calcula a evolução dessas correntes tendo como base um pequeno conjunto de parâmetros de entrada que devem ser fornecidos em pontos específicos no tempo, como a corrente de plasma, o beta normalisado, a posição da última superfície de fluxo fechada, e pontos de restrição como pontos-X. Esse modelo, portanto, nos permite projetar a evolução do plasma durante toda a descarga. O núcleo desse modelo consiste em equações de circuito que representam o acoplamento eletromagnético entre as bobinas magnéticas, a câmara de vácuo e o plasma. A inclusão da câmara de vácuo no modelo nos permite uma previsão mais realista da atenuação do campo elétrico toroidal na região do plasma e o cálculo auto-consistente das correntes induzidas na câmara de vácuo, cujo impacto no formato do plasma deve ser compensado pelas bobinas PF. Ainda mais, esse modelo, acoplado com um código de construção de equilíbrio, permite a geração de um equilíbrio MHD para o TCABR, garantindo uma melhor estimativa da evolução temporal de cada corrente e voltagem. Neste trabalho, a evolução temporal de oito cenários de plasma foram modelados utilizando o código desenvolvido. Durante essa modelagem, foi observado que para manter uma corrente de plasma no *flat top* de até I_p = 110 kA por até 1 s, as fontes de potência do sistema ohmico e das bobinas PF terão que operar nos quatro quadrantes de um espaço operacional tensão-corrente e fornecer, respectivamente, tensões e correntes de até ±2.3 kV/±24 kA, para controle da corrente plasma, e ±300 V/±9 kA, para controle de posição e formato do plasma.

Palavras-chave: Física de Plasmas; Magnetohidrodinâmica; Equilíbrio MHD; Tokamak; Computação numérica.

Contents

Acknowledgements i

Abstract (English/Portuguese) iii

List of figures ix

1 Introduction 1
- 1.1 The thermonuclear fusion energy . . . 2
- 1.2 The tokamak concept . . . 4
- 1.3 The need for plasma scenario control in tokamaks . . . 7
- 1.4 Outline of this dissertation . . . 8

2 Theoretical background 11
- 2.1 Plasma startup . . . 12
- 2.2 The ideal MHD model in tokamaks . . . 14
- 2.3 The TCABR electromagnetic model . . . 18
  - 2.3.1 Modelling active coils . . . 20
  - 2.3.2 Modelling the vacuum vessel . . . 22
  - 2.3.3 Modeling the plasma . . . 24

3 Numerical methods 27
- 3.1 Solving the Grad-Shafranov equation . . . 27
- 3.2 The Lagrange multipliers method . . . 29
- 3.3 The Newton-Raphson method . . . 30
- 3.4 The Crank-Nicholson method . . . 31

4 The Plasma Scenario Design code 35
- 4.1 Computational domains . . . 35
- 4.2 Iterative Picard method . . . 36
- 4.3 The free boundary equilibrium solver . . . 38
  - 4.3.1 Prescribing the plasma boundary and constraint points . . . 38
  - 4.3.2 Initial guess for the plasma current density and its poloidal magnetic flux 40
  - 4.3.3 The optimisation method for obtaining the PF coil currents . . . 41
  - 4.3.4 Parameterisation of the kinetic profiles . . . 42

5 Simulations of plasma scenarios in TCABR **47**
5.1 Magnetic configuration for plasma breakdown 47
5.2 The kinetic profiles 49
5.2.1 Total plasma pressure 49
5.2.2 Poloidal current function 50
5.2.3 Effect of the kinetic profiles on the PF coil currents and diamagnetism . 51
5.3 Time evolution of plasma scenarios 53
5.3.1 Limited plasmas 54
5.3.2 Diverted plasmas 65
5.3.3 The impact of the vacuum vessel on the PFC currents 73
5.3.4 Summary and discussion 74

6 Conclusions and outlook **75**

A Magnetic flux coordinates in a torus **77**
A.1 Metric element 78
A.2 Flux averages 78
A.3 Safety factor 79

Bibliography **81**

List of Figures

1.1 World population growth from 1700-2100. Source: https://ourworldindata.org/world-population-growth. . . . 1
1.2 Global energy consumption separated by energy resource. Source: https://ourworldindata.org/energy-production-consumption. . . . 2
1.3 Difference in energy between nuclear fission and nuclear fusion. Source: by Sarah Harman | U.S. Department of Energy. . . . 3
1.4 Representation of (left) a tokamak and (right) a stellarator. Source: Reproduced from M. Wischimeir: The tokamak principle-magnetic fusion (2016). . . . 4
1.5 Illustration of the tokamak concept. Source: Reproduced from M. Wischimeir: The tokamak principle-magnetic fusion (2016). . . . 5
1.6 Magnetic flux contours of (left) a limited plasma and (right) a diverted plasma configuration. Adapted from [8] . . . 6
1.7 Overview of the Plasma Physics Laboratory where TCABR is installed. . . . 7
1.8 Schematic illustration of a typical tokamak experiment. . . . 8

2.1 Coordinate system (R, ϕ, Z) and some plasma quantities. . . . 14
2.2 Two-wire system. . . . 19
2.3 Representation of the TCABR coils: the blue filaments belong to the Ohmic coils while the red filaments belong to the PF coils. . . . 21
2.4 Vacuum vessel filament model of TCABR. It is modelled by 160 toroidal filaments represented by the circles. The white area represents the vacuum vessel volume delimited by the graphite tiles walls represented by the grey area. . . . 22
2.5 Vacuum vessel (left) eigenvalues and (right) eigenvectors. . . . 24
2.6 Example of a toroidal current distribution $J_\phi(R, Z)$ for TCABR with $I_p = 90\,\text{kA}$. . 24

3.1 Time evolution of the Ohmic and vacuum vessel currents for a circular plasma scenario. . . . 33

4.1 Computational domains in the poloidal plane of TCABR: Plasma domain Ω_{pl} (yellowish region) delimited by the LCFS (continuous red line); The computational domain Ω_c (blueish region) composed by the plasma and the vacuum vessel (dark-grey region) domains, and delimited by its boundary (continuous blue line); Active coils region (reddish region). . . . 36

4.2 (a) Examples of plasma boundaries obtained from Equation 4.1: circular (red line), elongated (blue line), with negative triangularity (green line) and with an X-point (black line). (b) Example of a prescribed plasma boundary with an X-points imposed (red cross). 39
4.3 (a) Example of an initial guess of plasma current density. (b) Poloidal flux distribution produced by the plasma current density shown in (a) and the prescribed boundary points (blue dots) and X-point (red cross). 40
4.4 Poloidal fluxes: (left) due to the plasma, (centre) due to the PF coil currents and (right) total. Electric current estimated in each coil to have the shape as in the right-top panel 43
4.5 Examples of L-mode (first row) and H-mode (second row) pressure, temperature and density radial profiles, for different species, obtained from Equations 4.15, 4.16 and 4.17. 44

5.1 Plasma shapes envisaged for TCABR. Limited configurations: (a) circular, (b) elongated, (c) with squareness, (d) positive triangularity and (e) negative triangularity. Diverted configurations: (f) lower single-null, (g) upper single-null, (h) double-null, and (i) snowflake. 48
5.2 Magnetic configuration used for inducing breakdown at $(R_{\mathrm{br}}, Z_{\mathrm{br}}) = (0.51\ ,\ 0)$ m and $I_{\mathrm{OH}} = 24$ kA with a second order null-point at that location. 49
5.3 Static simulation for a prescribed pressure profile given by $p(\Psi_N) = p_0\left(\frac{1}{1+\Psi_N} - \frac{\Psi_N}{2}\right)$. 52
5.4 Static simulation for a prescribed pressure profile given by $p(\Psi_N) = p_0\left(\frac{1}{1+\Psi_N^2} - \frac{\Psi_N^2}{2}\right)$. 52
5.5 Static simulation for a prescribed pressure profile given by $p(\Psi_N) = p_0\left(\frac{1}{1+\Psi_N^3} - \frac{\Psi_N^3}{2}\right)$. 52
5.6 Static simulation for a characteristic L-mode pressure profile. 53
5.7 Static simulation for a characteristic H-mode pressure profile. 53
5.8 Schematic of a typical tokamak discharge. The magnetic configuration of breakdown is expected to occur at $t_0 = 0$ s where the Ohmic coil is charged with a current $I_{\mathrm{OH}}(t_0) \neq 0$. 54
5.9 Time evolution of a circular plasma at three points in time. 55
5.10 Time evolution of the voltage, current, and power on the Ohmic and vacuum vessel (induced) for a circular plasma. 56
5.11 Time evolution of the voltage, current, and power on each PF coil for a circular plasma. 56
5.12 Time evolution of an elongated plasma at three points in time. 57
5.13 Time evolution of the voltage, current, and power on the Ohmic and vacuum vessel (induced) for an elongated plasma. 58
5.14 Time evolution of the voltage, current, and power on each PF coil for an elongated plasma. 58
5.15 Time evolution of a limited plasma with positive triangularity at three points in time. 59
5.16 Time evolution of the voltage, current, and power on the Ohmic and vacuum vessel (induced) for a plasma with positive triangularity. 60

5.17 Time evolution of the voltage, current, and power on each PF coil for a plasma with positive triangularity. 60
5.18 Time evolution of a limited plasma with negative triangularity at three points in time. 61
5.19 Time evolution of the voltage, current, and power on the Ohmic and vacuum vessel (induced) for a plasma with negative triangularity. 62
5.20 Time evolution of the voltage, current, and power on each PF coil for a plasma with negative triangularity. 62
5.21 Time evolution of a squared plasma at three points in time. 63
5.22 Time evolution of the voltage, current, and power on the Ohmic and vacuum vessel (induced) for a squared plasma. 64
5.23 Time evolution of the voltage, current, and power on each PF coil for a squared plasma. 64
5.24 Time evolution of a diverted plasma at three points in time. 65
5.25 Time evolution of the voltage, current, and power on the Ohmic and vacuum vessel (induced) for a diverted plasma. 66
5.26 Time evolution of the voltage, current, and power on each PF coil for a diverted plasma. 66
5.27 Time evolution of a diverted plasma at three points in time. 67
5.28 Time evolution of the voltage, current, and power on the Ohmic and vacuum vessel (induced) for a diverted plasma. 68
5.29 Time evolution of the voltage, current, and power on each PF coil for a diverted plasma. 68
5.30 Time evolution of a diverted plasma at three points in time. 69
5.31 Time evolution of the voltage, current, and power on the Ohmic and vacuum vessel (induced) for a diverted plasma. 70
5.32 Time evolution of the voltage, current, and power on each PF coil for a diverted plasma. 70
5.33 Time evolution of a snowflake plasma at three points in time. 71
5.34 Time evolution of the voltage, current, and power on the Ohmic and vacuum vessel (induced) for a snowflake plasma. 72
5.35 Time evolution of the voltage, current, and power on each PF coil for a snowflake plasma. 72
5.36 PF coil currents with and without the inclusion of the vacuum vessel for the circular plasma 73
5.37 Difference on the PF coil currents when the vacuum vessel is included. Here $\Delta = I_{\text{with VV}} - I_{\text{no VV}}$. 74

A.1 General toroidal coordinates 77

1 Introduction

The course of humanity's wealth and well-being over the last centuries has rapidly increased due to the availability of new sources of energy. As a consequence of the increase of the world average standard of living, the global population more than quadrupled over the last 100 years, Figure 1.1, amplifying humanity's impact on the natural environment.

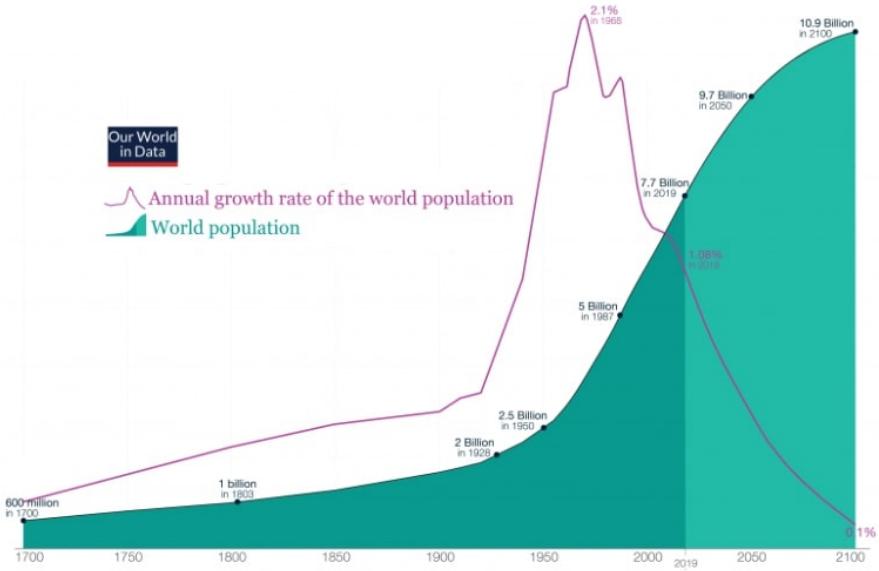

Figure 1.1: World population growth from 1700-2100. Source: https://ourworldindata.org/world-population-growth.

Presently, the energy demand is supplied by a combination of many sources, in which about 80% of the global energy consumption comes from the burning of fossil fuels (coal, oil, and gas), Figure 1.2, and whose burn releases carbon dioxide, among other greenhouse gases, which are the fundamental driver for the global climate change. The rapidly growing of the energy consumption makes the challenge of transitioning the world's energetic matrix away from fossil fuels towards low-carbon energy sources more difficult.

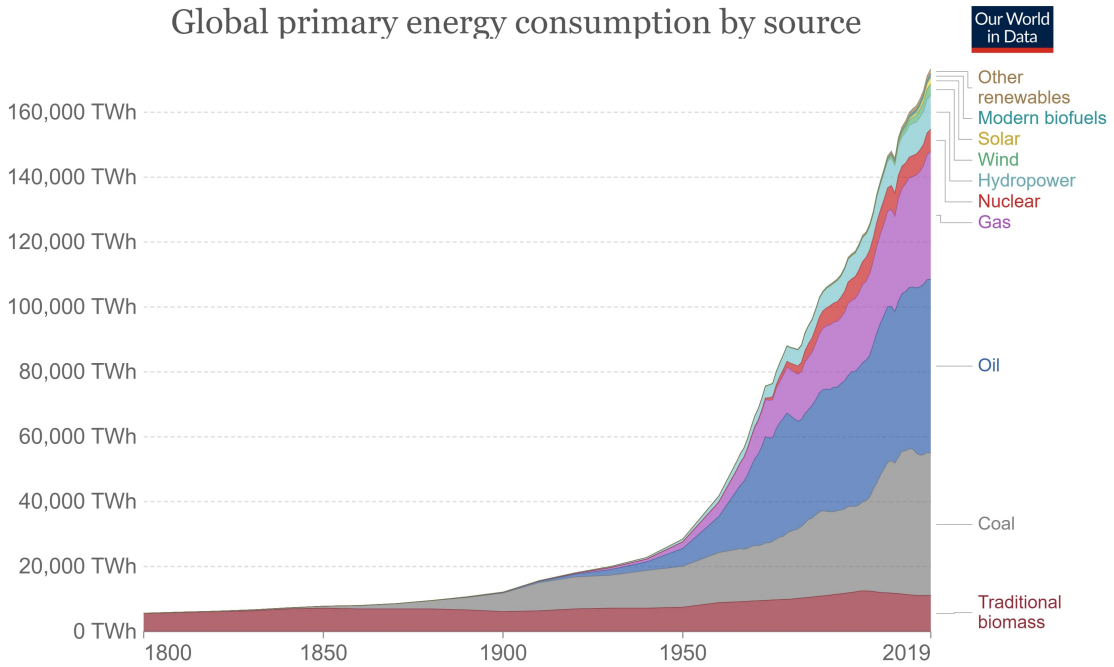

Figure 1.2: Global energy consumption separated by energy resource. Source: https://ourworldindata.org/energy-production-consumption.

Although there are few realistic scenarios, the world needs to shift away from fossil fuels to an energy mix dominated by low-carbon sources of energy – renewable technologies and nuclear power.

1.1 The thermonuclear fusion energy

When the BBC Future, at the launch of Cambridge University's Big Data Institute, asked Professor Stephen Hawking what world-changing idea he would like to see implemented by humankind, he said, "the development of fusion power to give an unlimited supply of clean energy" [1]. Professor Hawking was talking about the most basic energy production mechanism in the Universe – nuclear fusion –, which is the process that powers stars whereby two or more nuclei fuse together to form a heavier one. And the reason why he said such a thing is because since the early 1950s, research on thermonuclear controlled fusion has been conducted to provide a sustainable and environment friendly energy source that could provide humanity with virtually millions of years of clean energy.

For elements with atomic number masses lower than iron as the reagents, the total final mass is slightly lower than the total initial mass. The mass difference (Δm) appears as energy according to Einstein's equation, $E = \Delta m\, c^2$. Usually, these two light nuclei are hydrogen isotopes and among all the possible fusion reactions, the one with the largest cross-section at

lower temperature is the one between deuterium $\left({}^{2}_{1}D\right)$ and tritium $\left({}^{3}_{1}T\right)$:

$$ {}^{2}_{1}D^{1+} + {}^{3}_{1}T^{1+} \rightarrow {}^{4}_{2}H_{e}^{2+}\,(3.5\text{ MeV}) + {}^{1}_{0}n^{0}\,(14.1\text{ MeV}), \tag{1.1} $$

where ${}^{4}_{2}H_{e}^{2+}$ and ${}^{1}_{0}n^{0}$ represent helium nuclei (or known as alpha particle), and neutron, respectively. The fusion of hydrogen isotopes, such as the one shown in Equation 1.1, creates relatively high amounts of energy - about one order of magnitude greater than nuclear fission, and it also does not produce long-lived radioactive products [2]. One can see in Figure 1.3 the difference between the two nuclear process that produce energy. On the left panel, there is the controlled fission as in today's nuclear reactors, in which a neutron collides with a larger atom (generally uranium and plutonium) forcing it to excite and split into two smaller atoms. It releases about a million times more energy than other carbon-based sources. On the other hand, its radioactive byproducts must be properly and safely stored for tens of thousands of years. On the right panel of Figure 1.3 is controlled fusion as currently being studied by scientists. The process releases around four times more energy than fission with byproduct Helium: an inert and non-toxic gas. Fusion fuels are widely available and nearly inexhaustible. Deuterium can be distilled from all forms of water. Tritium, however, because of its natural occurrence is extremely rare on Earth, will be produced inside the reactor plant as fusion-born neutrons react with lithium located in the surrounds of the reactor. Terrestrial reserves of lithium would permit the operation of fusion power plants for more than 1000 years, while sea-based reserves of deuterium would fulfill needs for millions of years [3].

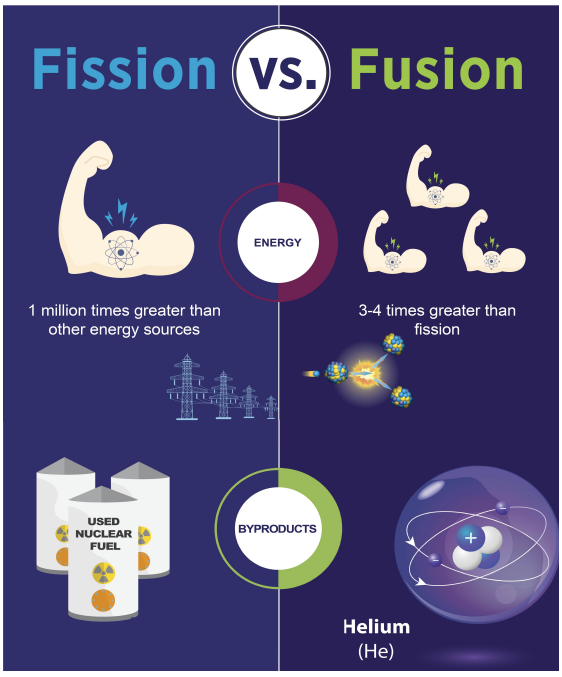

Figure 1.3: Difference in energy between nuclear fission and nuclear fusion. Source: by Sarah Harman | U.S. Department of Energy.

Reproducing the star-power source in laboratories is still a matter of intense study and research all around the world. This is because the fusion process can only occur under specific extreme conditions, where atoms must be subjected to immense heat and pressure to overcome the Coulomb repulsion between the nuclei. Over the past decades, two method has shown positive results to yield sustained fusion reactions in laboratories: the use of magnets to confine a hot plasma, and as the use of intense lasers to target a grain-sized capsule filled with deuterium and tritium. Among the latter, the National Ignition Facility (NIF), at the Lawrence Livermore National Laboratory, have demonstrated net energy gain in inertial confinement fusion, achieving a yield of more than 1.3 MJ, a 25 times increase over NIF's record experiment conducted in 2018 [4].

Although the major achievements in inertial confinement fusion, the leading global approach in confining fusion fuel is the magnetic confinement fusion (MCF). Here, the fuel needs to be sufficiently hot - hotter than the sun's core temperature of 15 million °C - such that matter can exist only in the plasma state, where negatively-charged electrons are separated from the positively-charged atomic nuclei. This makes MCF ideal for confining such a hot plasmas as electrical charges follow the magnetic field lines due to the Lorentz force. The most effective magnetic configuration for plasma confinement is a torus, in which the magnetic field is curved around to form a closed loop. There are several types of toroidal confinement system, with the most important being tokamaks and stellarators devices, Figure 1.4.

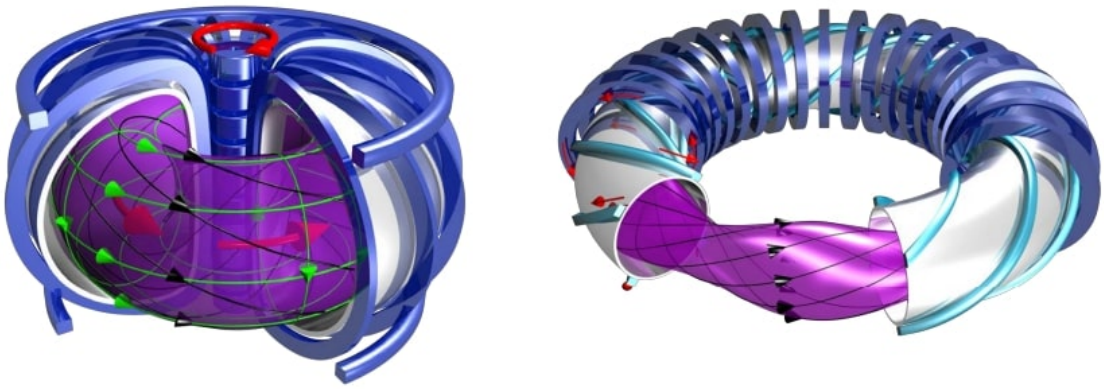

Figure 1.4: Representation of (left) a tokamak and (right) a stellarator. Source: Reproduced from M. Wischimeir: The tokamak principle-magnetic fusion (2016).

1.2 The tokamak concept

A tokamak - a Russian acronym for torus-shaped vacuum chamber surrounded by magnetic coils - is a toroidal magnetic confinement device in which plasmas act as the secondary of a one-turn, short-circuited transformer and it was first conceptualized by the Soviet physicists Igor Tamm and Andrei Sakharov in the early 1950s. A schematic diagram of the main magnetic fields and current configuration in a tokamak is presented in Figure 1.5.

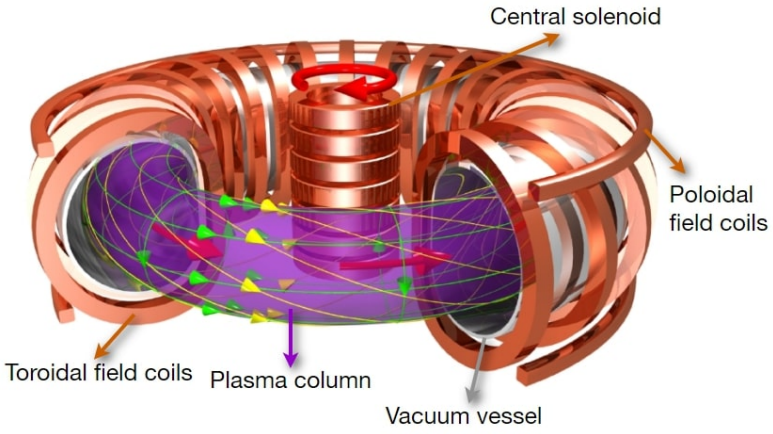

Figure 1.5: Illustration of the tokamak concept. Source: Reproduced from M. Wischimeir: The tokamak principle-magnetic fusion (2016).

The main magnetic field component is the one in the toroidal direction, which is generated by the toroidal field coils, Figure 1.5. This field has a characteristic $B_\phi \propto R^{-1}$ dependence, where R is the distance from the machine axis of symmetry. The B_ϕ field is not constant in space, resulting in a gradient which give rise to a particle drift in the vertical direction, the so-called ∇B drift, which is charge dependent. Due to the separation of charges, a vertical electric field is generated and another well-known drift appears, the so-called $\mathbf{E} \times \mathbf{B}$ drift, causing a radially outward displacement of the entire plasma column. Therefore, the toroidal magnetic field alone cannot confine the plasma, leading to the need of a second, weaker, poloidal magnetic field, $\mathbf{B}_\theta$, created by the plasma itself through transformer action. The combination of the toroidal and poloidal magnetic fields results in helically twisted field lines which, in average, cancel those vertical drifts and improves particle confinement.

Since the plasma current is crucial for plasma confinement, it must be sustained for the duration of the experiment. The main way used in tokamaks to sustain a plasma current is to vary the magnetic flux of the Ohmic coil (the primary transformer coil in Figure 1.5), or Central Solenoid, which allows tokamak operation only in a pulsed mode. One main issue with this process is that the Ohmic coil current cannot be ramped indefinitely, thus driving the need of alternatives to drive the plasma current non-inductively. It is possible to develop plasma scenarios that allow steady-state operation using the so-called bootstrap current, a self-generated current that flows parallel to the field lines [6, 14], and also through auxiliary current drive systems [5, 7].

The helically twisted magnetic field lines in tokamaks form closed magnetic flux surfaces, within which the plasma is confined. There are two main plasma configurations responsible for preventing the hot plasma from touching the vacuum vessel walls. The first is called *limited* plasma configuration, characterised by the intersection of the last closed flux surface (LCFS) with a solid material (left panel of Figure 1.6). The second is called *diverted* configuration and is characterised by a null-point (or X-point) - a point in the poloidal plane where the

poloidal magnetic field component vanishes. In diverted plasmas, the LCFS is determined by the magnetic flux surface passing through the X-point and it is called *separatrix*.

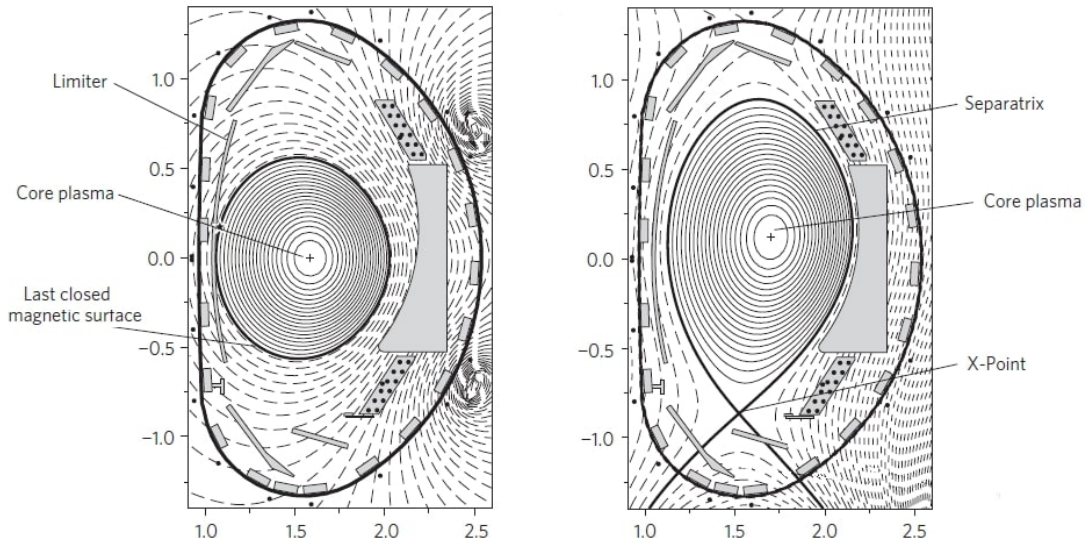

Figure 1.6: Magnetic flux contours of (left) a limited plasma and (right) a diverted plasma configuration. Adapted from [8]

The diverted plasmas are good for many reasons. The confined region is not in direct contact with the wall, turning the plasma hotter and "cleaner". Also, the local low poloidal field near the x-point creates a toroidally elongated trajectories for particles so they can cool down before reaching the divertor.

The TCABR tokamak

The Tokamak Chauffage Alfvén Brésilien (TCABR), Figure 1.7, is a small-size tokamak operated by the Plasma Physics Laboratory (LFP) of the Institute of Physics of the University of São Paulo (IFUSP). It was originally designed and built in 1979 and operated until 1992 by the Centre de Recherches en Physique des Plasmas at the Ecole Polytechnique Fédérale de Lausanne, in Switzerland. The main objective of the TCA (the french word *Brésilien* was added to the machine's name after it was transferred to Brazil) was to investigate the possibility of plasma heating by dissipation of Alfvén waves [15]. After being decommissioned and transferred to IFUSP, the device was rebuilt with a new control, wave excitation, and plasma diagnostic systems.

In its current configuration, TCABR plasmas are made of hydrogen and are wall-limited with circular shape. Its major and minor radii are $R_0 = 0.62$ m, and $a \leq 0.2$ m, respectively. Its central electron temperature can be as high as $T_e \leq 800$ keV and its mean electron density $\bar{n}_e \leq 5.0 \times 10^{19}$ m^{-3}. Also, in order to create its toroidal magnetic field of $B_0 \leq 1.1$ T and plasma current of $I_p \leq 120$ kA, TCABR has 18 toroidal field coils, equally spaced in the toroidal direction, and

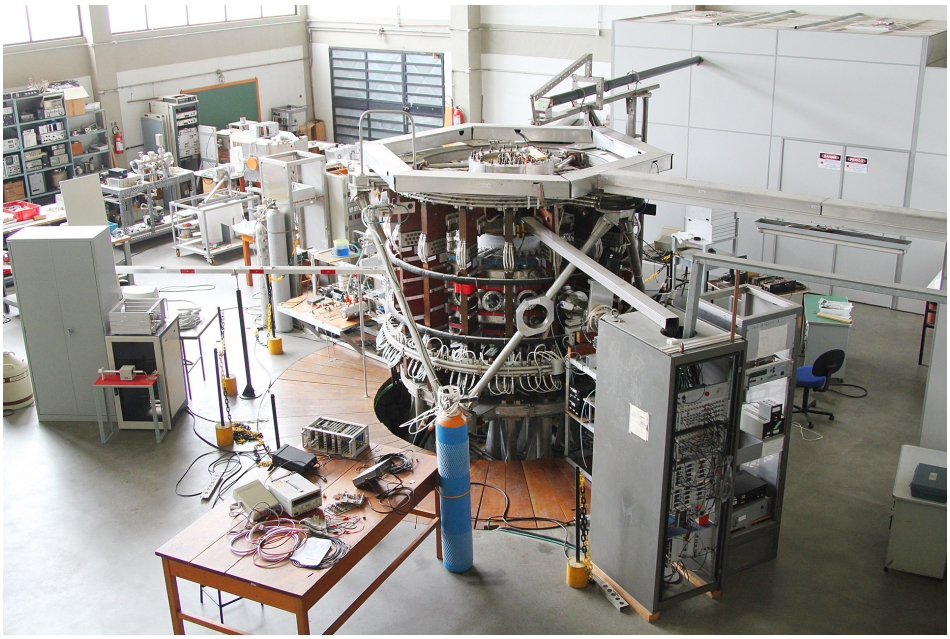

Figure 1.7: Overview of the Plasma Physics Laboratory where TCABR is installed.

7 Ohmic magnetic field coils: the central solenoid and 6 stray-field compensation coils. To control the position and shape of the plasma, TCABR has 14 poloidal field (PF) coils: 10 coils located in the inner part of the tokamak and other 4 coils located in its outer part. Since TCABR does not have an auxiliary heating system, it operates only with Ohmically heated discharges and in the so-called low confinement mode (L-mode).

Being a machine that has been operating for over thirty years, a major revision and upgrade of its main systems are necessary to keep TCABR contributing to international-relevant modern plasma physics and fusion researches. Among the possible upgrades proposed for TCABR, one has decided to increase the number of plasma shapes that TCABR can produce by increasing the number of poloidal field coils from 14 to 16, and to make it suitable for investigating the physics of resonant magnetic perturbations, rotation of the plasma column, and plasma edge turbulence in different equilibrium configurations.

1.3 The need for plasma scenario control in tokamaks

Tokamaks are pulsed machines, meaning that it is necessary to vary the magnetic flux of the central solenoid to create the plasma current. In each discharge, the plasma is initiated through a process called *breakdown*, then the plasma current is ramped up to a reference value, the so-called current flat-top, which is maintained constant for a sufficiently along time during the discharge, and finally the current is ramped down until the plasma is terminated, Figure 1.8.

The time evolution of the poloidal field coil currents and of some key parameters define the so-called plasma scenario. Some of these parameters are: electron plasma density, plasma current,

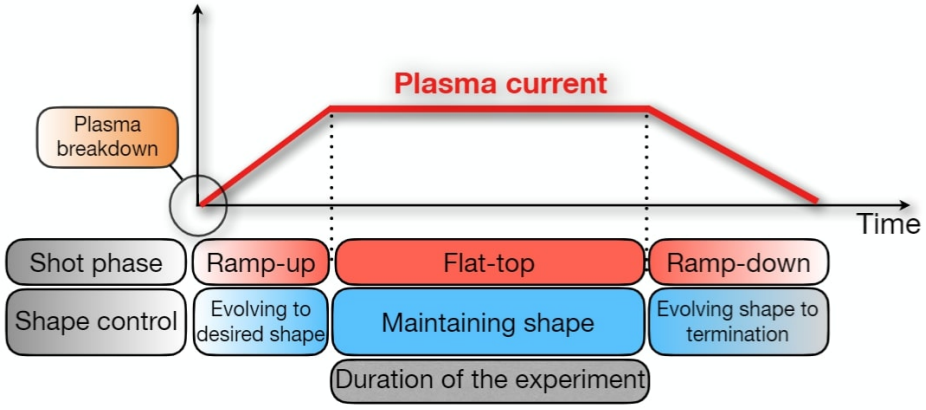

Figure 1.8: Schematic illustration of a typical tokamak experiment.

toroidal magnetic field, total plasma pressure, plasma shape and position, number of X-points and their locations, among others. Each scenario has its distinct properties, advantages and disadvantages. The overall objective of a plasma control system is to conduct the plasma state towards a desired operational point and keep it there for the duration of the discharge. Therefore, feedback control has emerged as an essential and mandatory component in the tokamak operation. To improve plasma control, the plasma boundary must be kept as close as possible to the nearby conducting walls to increase plasma stability. In this scenario, any undesired plasma movement induces eddy currents in the walls that, in turn, generate a magnetic field that opposes the original plasma movement thus ensuring passive stabilization [9]. The main issue when modeling plasma control is how to create a physical model that is simple enough so that the solutions can be found using approximate numerical methods that catch the principal phenomena, but still simple enough to make it useful for de design of plasma control systems [10].

1.4 Outline of this dissertation

In this chapter, a brief introduction to nuclear fusion and the tokamak concept is presented along with some highlights of plasma scenarios and control.

- Chapter 2 enlightens the fundamental theoretical background needed for comprehension of this work. The plasma formation process is described in a simplified way in order to obtain the expression for the effective connection length. An introduction of the ideal MHD model is followed to describe the plasma equilibrium with the Grad-Shafranov equation. Lastly, the derivation of the electromagnetic model of a tokamak is presented.

- Chapter 3 addresses the numerical methods used in this work. They are needed to invert the elliptic operator in the Grad-Shafranov equation, to minimise a cost function of the poloidal field coil currents, to find the minimum/maximum and saddle points of a 2D surface, and to solve an 1D ordinary differential equation (ODE).

- Chapter 4 presents the overview of the developed Plasma Scenario Design code. It focuses on the classification of equilibrium followed by describing a method for solving the non-linear Grad-Shafranov equation known as Iterative Picard method.
- Chapter 5 summarises the main results and conclusions of this work.

2 Theoretical background

Describing the plasma state is not an easy task. Roughly speaking, plasmas are ionized gases where charged particles - ions and electrons - are moving around in response to the long-range Coulomb forces produced by other charged particles in the system. However, these moving charged particles also creates electromagnetic fields that can affect their own trajectories. The most commonly used model used to describe plasmas is the so-called ideal MHD model which assumes that the plasma can be represented by a single fluid with infinite electrical conductivity and zero ion gyro radius [9]. The set of MHD equations are obtained by taking the moments of the Boltzmann equation and each of them contains a higher moment thus forming an infinite set of fluid equations. One of the most fundamental studies in plasma physics is the dynamics of the system. However, before rushing to solve the general time-dependent MHD equations, one must recall that the fixed points in the phase space gives important information about the evolution and the stability of the system [11]. Therefore, the equilibrium configurations, i.e., the time-independent solutions of the MHD model, must be known first. Generally, tokamak plasmas are described using the following approximations:

- The plasma is fully ionized and composed of electrons and positive ions;
- The displacement current in Ampère's law is neglected, i.e. $\nabla \times \mathbf{B} = \mu_0 \mathbf{J}$;
- Quasi-neutrality is assumed, i.e. the electron and ion densities are equal ($n_e = n_i = n$) thus leading to $\nabla \cdot \mathbf{E} = 0$.

This set of assumptions, along with others, are required for the formulation of the ideal MHD model. However, even though some of the assumption made in this model are never satisfied in real tokamak experiments, it has shown to give reasonably accurate predictions of the macroscopic behavior of tokamak plasmas.

2.1 Plasma startup

Plasma initiation, or breakdown, is a well-established part of the tokamak operation. It starts with a pre-charging of the central solenoid, with current in a direction according to the desired plasma current, and the injection of a prefill hydrogen or deuterium gas into the vacuum vessel. The central solenoid current is then ramped down to induce a toroidal electric field that accelerates free electrons that eventually collides with the neutral gas, ionizing them. In succession, this process produces more electrons, which are again accelerated by the toroidal electric field inducing further ionization processes, leading to an exponential increase of the number of electrons. The most common used model to describe this process is the so-called Townsend avalanche [12].

The plasma start-up process can be divided into three phases [13]: *(i)* the breakdown or avalanche phase, *(ii)* the impurity burn-through phase, and *(iii)* the controlled plasma current ramp-up phase. During the avalanche phase, a significant part of the heating power is lost through the ionization of the neutral gas and through the line-radiation from impurities that might be present in the plasma. The power loss due to radiation has a maximum at a certain level of ionization, called radiation barrier. In order to raise the plasma temperature via Ohmic heating, the plasma needs to burn through this radiation barrier, allowing the plasma to reach a complete degree of ionization. Once this stage is surpassed, the plasma current is rampep up until the flat-top is reached.

The breakdown phase

The inductive ionization phase, also known as breakdown phase, is dominated by collisions between free electrons and neutral particles that compose the gas. This phase can be modelled by a Townsend-like model [12], which assumes that the ions are stationary due their higher mass. The evolution of the electron density, n_e, is determined by the difference between the ionization frequency, ν_{ion}, and the electron loss rate, ν_{loss},

$$\frac{d\,n_e}{d\,t} = (\nu_{\text{ion}} - \nu_{\text{loss}})\; n_e. \tag{2.1}$$

This equation can be easily integrated and yields the electron density evolution during this phase, which is expressed as

$$n_e(t) = n_{e0} \exp\left[(\nu_{\text{ion}} - \nu_{\text{loss}})\; t\right], \tag{2.2}$$

where n_{e0} is the electron density at $t = 0$. Therefore, the ionization phase is the result of an avalanche process, which occurs when $\nu_{\text{ion}} > \nu_{\text{loss}}$. These electrons are then accelerated in the toroidal direction by the toroidal electric field up to a characteristic velocity parallel to the toroidal magnetic field, $v_{\text{e},\parallel}$. The ionization frequency may be written as a function of the

ionization mean free path, λ_{ion},

$$\nu_{\text{ion}} = \frac{v_{\text{e},\parallel}}{\lambda_{\text{ion}}}. \tag{2.3}$$

Here, λ_{ion} represents the distance required for electrons to travel among two successive ionizing collisions. This quantity can be expressed in terms of the First Townsend coefficient,

$$\alpha_T = \frac{1}{\lambda_{\text{ion}}} = a\, p_n\, e^{-\frac{b\, p_n}{E_\phi}}. \tag{2.4}$$

In this equation, a and b are constants that depend on the gas and are determined experimentally, p_n is the neutral gas pressure in units of Pa and E_ϕ is the toroidal electric field in units of V/m. For a given value of E_ϕ, there is an optimum value of the neutral gas pressure corresponding to the maximum of the First Townsend coefficient. One obtain this by calculating:

$$\frac{d\alpha_T}{d\, p_n} = 0 \implies a\, e^{-\frac{b\, p_n}{E_\phi}} \left(1 - \frac{b}{E_\phi} p_n\right) \implies p_n = \frac{E_\phi}{b}. \tag{2.5}$$

During the breakdown phase, since the magnetic configuration is characterized by open magnetic field lines, the electrons impinge on the first wall after a certain number of toroidal turns. The electron loss rate may thus be estimated as

$$\nu_{\text{loss}} = \frac{v_{\text{e},\parallel}}{L_\parallel}, \tag{2.6}$$

where $L_\parallel$ is the distance that the electron travels before reaching the wall, called connection length. This equation shows that ν_{loss} decreases at regions where the connection length is larger. And it can also be shown [13] that the effective connection length depends on the magnetic field configuration through

$$L_{\text{eff}} \approx \frac{B_\phi}{|\nabla B_\theta|}. \tag{2.7}$$

Therefore, controlling the PF coil currents to produce a localized null-point in the poloidal field at a desired location within the vacuum vessel can be used to control where the breakdown is expected to be initiated. The condition for the onset of the avalanche is achieve when the ionization rate is at least equal to the electron loss rate, which yields

$$a\, p_n\, e^{-\frac{b p_n}{E_\phi}} \approx \frac{|\nabla B_\theta|}{B_\phi}. \tag{2.8}$$

This equation shows that the breakdown in a tokamak depends on the choice of the gas (a, b, and p_n), the toroidal electric field intensity (E_ϕ), and depends on the poloidal field configuration during the startup phase.

2.2 The ideal MHD model in tokamaks

The first step to develop a model of an axisymmetric tokamak that serves as a first approximation of the MHD equilibrium of a plasma is to describe the static model of the spatial distribution of the magnetic fields and electric current densities present in the system. We start by introducing a right-handed cylindrical coordinate system (R, ϕ, Z) described by the radial coordinate R, the vertical position Z, and the corresponding ignorable toroidal angle ϕ.

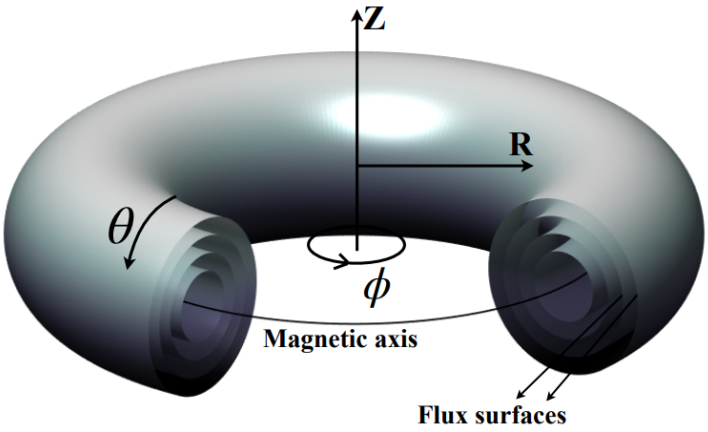

Figure 2.1: Coordinate system (R, ϕ, Z) and some plasma quantities.

Suppose we have a magnetic field that can be decomposed in a poloidal component, $B_\theta(R, Z)$, and in a toroidal component, $B_\phi(R, Z)$. We can define the poloidal magnetic flux as being

$$\Psi(R, Z) = \iint_{S_{\text{pol}}} \mathbf{B} \cdot d\mathbf{S}_{\text{pol}}, \tag{2.9}$$

where $\mathbf{S}_{\text{pol}}$ is any $Z = \text{const}$ circular surface oriented such that $d\mathbf{S}_{\text{pol}} = R\, dR\, d\phi\, \hat{\mathbf{e}}_\mathbf{Z}$. Then, we calculate the poloidal flux accordingly

$$\Psi(R, Z) = \iint_{S_{\text{pol}}} \mathbf{B} \cdot \hat{\mathbf{e}}_\mathbf{Z}\, R\, dR\, d\phi = \int_0^{2\pi} d\phi \int_0^R B_Z(R', Z)\, R'\, dR' = 2\pi \int_0^R B_Z\, R'\, dR'. \tag{2.10}$$

Differentiating with respect to the upper limit radial coordinate gives

$$B_Z(R, Z) = \frac{1}{2\pi R} \frac{\partial \Psi}{\partial R}, \tag{2.11}$$

and using the divergence-free statement of the magnetic field, $\nabla \cdot \mathbf{B} = 0$, leads to

$$B_R(R, Z) = -\frac{1}{2\pi R} \frac{\partial \Psi}{\partial Z}. \tag{2.12}$$

Hence, the sum of both components gives the poloidal contribution of the magnetic field,

which can be expressed as

$$\mathbf{B}_\theta(R,Z) = B_R \nabla R + B_Z \nabla Z = \frac{1}{2\pi R}\left(-\frac{\partial \Psi}{\partial Z}\nabla R + \frac{\partial \Psi}{\partial R}\nabla Z\right) = \frac{1}{2\pi}\nabla\Psi \times \nabla\phi, \tag{2.13}$$

with $\nabla\phi = \hat{\mathbf{e}}_\phi / R$ and $\nabla\Psi$ pointing inward radially.

For the toroidal component of the magnetic field, we can use the definition of the poloidal component of the electric current, where

$$I_\theta = \iint_{S_{\text{pol}}} \mathbf{J}\cdot d\mathbf{S}_{\text{pol}} = \frac{1}{\mu_0}\iint_{S_{\text{pol}}} \nabla\times\mathbf{B}\cdot d\mathbf{S}_{\text{pol}} = \frac{1}{\mu_0}\oint_{\Gamma_{\text{tor}}} \mathbf{B}\cdot d\ell_{\text{tor}}, \text{ where } d\ell_{\text{tor}} = R\,d\phi\,\hat{e}_\phi, \tag{2.14}$$

with Γ_{tor} being an intersection curve between a Z = const-plane with Ψ = const. flux surface, and where we have used the stationary Ampère's law $\mu_0\mathbf{J} = \nabla\times\mathbf{B}$. With this, we obtain

$$\mathbf{B}_\phi(R,Z) = \frac{\mu_0 I_\theta}{2\pi}\nabla\phi. \tag{2.15}$$

Having the poloidal and toroidal component of the magnetic field, and defining the poloidal current function $F = R B_\phi$, the magnetic field can be expressed as

$$\mathbf{B}(R,Z) = \frac{1}{2\pi}\nabla\Psi\times\nabla\phi + F\nabla\phi. \tag{2.16}$$

Regions in space of constant Ψ define what it is called magnetic flux surfaces, and as we can see from Equation 2.16, the dot product of it with $\nabla\Psi$ results in $\mathbf{B}\cdot\nabla\Psi = 0$, which means the magnetic field lines always lie on a given flux surface. We are now interested in understanding how the electrical current densities are distributed with respect to Ψ. From Ampère's law,

$$\mu_0\mathbf{J} = \nabla\times\mathbf{B} = \nabla\times\left(\frac{1}{2\pi}\nabla\Psi\times\nabla\phi + F\nabla\phi\right). \tag{2.17}$$

Using some vectorial properties, and defining the toroidal elliptic operator

$$\Delta^* := R\frac{\partial}{\partial R}\left(\frac{1}{R}\frac{\partial}{\partial R}\right) + \frac{\partial^2}{\partial Z^2}, \tag{2.18}$$

we obtain the electric current density

$$\mathbf{J} = \frac{1}{\mu_0}\nabla F\times\nabla\phi - \frac{1}{2\pi\mu_0}\Delta^*\Psi\,\nabla\phi. \tag{2.19}$$

Taking the dot product of Equation 2.19 with the toroidal direction $\hat{\mathbf{e}}_\phi$, we obtain the relation between the spatial distribution of the magnetic flux and the toroidal component of the electrical current densities,

$$\Delta^*\Psi = -2\pi\mu_0 R J_\phi(R,Z). \tag{2.20}$$

Therefore, we can rewrite Equation 2.19 as

$$\mathbf{J} = \frac{1}{\mu_0}\nabla F \times \nabla\phi + R J_\phi \nabla\phi. \tag{2.21}$$

The Grad-Shafranov equation

A common and important application when considering the plasma as a single-fluid is the calculation of the MHD equilibrium configuration using the momentum conservation equation [16] given by

$$\rho_m \left[\frac{\partial \mathbf{v}}{\partial t} + (\mathbf{v}\cdot\nabla)\,\mathbf{v}\right] = \nabla\cdot\mathbf{P} - \mathbf{J}\times\mathbf{B}, \tag{2.22}$$

where ρ_m is the plasma mass density, $\mathbf{v}$ is the fluid velocity, and $\mathbf{P}$ is the total plasma pressure tensor. An equilibrium state is obtained by setting $\partial_t \to 0$ in the equation. Assuming that the plasma is dominated by collisions, the electron and ion distribution functions can be considered to be nearly Maxwellian, which leads to an isotropic pressure. If plasma flow is also neglected, the above momentum conservation equation reads

$$\nabla p = \mathbf{J}\times\mathbf{B}, \tag{2.23}$$

where p is the scalar plasma (total) pressure. Taking the dot product of Equation 2.23 with the magnetic field yields

$$\mathbf{B}\cdot\nabla p = \mathbf{B}\cdot(\mathbf{J}\times\mathbf{B}) = 0 \Rightarrow \frac{1}{2\pi}\left(\nabla\Psi\times\nabla\phi\right)\cdot\nabla p + F\underbrace{\nabla\phi\cdot\nabla p}_{0,\ \text{once}\ \partial_\phi p = 0} = 0. \tag{2.24}$$

Using the vectorial property $(\mathbf{A}\times\mathbf{B})\cdot\mathbf{C} = (\mathbf{C}\times\mathbf{A})\cdot\mathbf{B}$, we end up with

$$\left(\nabla p\times\nabla\Psi\right)\cdot\nabla\phi = \frac{1}{R}\left(\frac{\partial\Psi}{\partial R}\frac{\partial p}{\partial Z} - \frac{\partial\Psi}{\partial Z}\frac{\partial p}{\partial R}\right) = 0 \Rightarrow \det\left[\frac{\partial(\Psi,p)}{\partial(R,Z)}\right] = 0, \tag{2.25}$$

which means that the pressure is a flux function, i.e. $p = p(\Psi)$. Now, taking the dot product of Equation 2.23 with the electric current density yields

$$\mathbf{J}\cdot\nabla p = \mathbf{J}\cdot(\mathbf{J}\times\mathbf{B}) = \frac{1}{\mu_0}\left(\nabla F\times\nabla\phi\right)\cdot\nabla p - \frac{1}{2\pi\mu_0}\Delta^*\Psi\underbrace{\nabla\phi\cdot\nabla p}_{0} = 0 \tag{2.26}$$

Since we obtained $p = p(\Psi)$, then $\nabla p = \frac{dp}{d\Psi}\nabla\Psi$. Therefore,

$$\left(\nabla F\times\nabla\phi\right)\cdot\nabla p = \frac{dp}{d\Psi}\left(\nabla\Psi\times\nabla F\right)\cdot\nabla\phi = 0 \Rightarrow \det\left[\frac{\partial(\Psi,F)}{\partial(R,Z)}\right] = 0, \tag{2.27}$$

and we can conclude that the poloidal current function is also a flux function, i.e. $F = F(\Psi)$.

With that in hand, inserting the current density **J** and the magnetic field **B** in the force balance equation (Equation 2.23) leads to

$$\nabla p = -\frac{1}{2\pi\mu_0}\left[\left(\nabla F \times \nabla\phi\right)\cdot\nabla\Psi\right]\nabla\phi - \frac{F}{\mu_0 R^2}\nabla F - \frac{1}{4\pi^2 R^2\mu_0}\Delta^*\Psi\,\nabla\Psi \Rightarrow \tag{2.28}$$

$$\Rightarrow \frac{dp}{d\Psi}\nabla\Psi = -\frac{1}{2\pi\mu_0}\left[\left(\frac{dF}{d\Psi}\nabla\Psi\times\nabla\phi\right)\cdot\nabla\Psi\right]\nabla\phi - \frac{F}{\mu_0 R^2}\frac{dF}{d\Psi}\nabla\Psi - \frac{1}{4\pi^2 R^2\mu_0}\Delta^*\Psi\,\nabla\Psi. \tag{2.29}$$

Denoting $()' \equiv d/d\Psi$, and taking the dot product of this equation with respect to $\nabla\Psi$ yields

$$\Delta^*\Psi = -4\pi^2\left(\mu_0 R^2 p' + FF'\right). \tag{2.30}$$

This is the well-known Grad-Shafranov equation. It is a second-order, elliptic, partial differential equation. As the source term depends on the solution $\Psi(R,Z)$, the poloidal magnetic flux Ψ is both an independent and dependent variable, which means it is not possible to establish the plasma boundary before solving the equation, turning this into a free boundary problem.

The electric current density components

Equation 2.21 describes how the spatial distribution of the poloidal magnetic flux (and consequently the magnetic fields) relates with the vectorial electric current density. By using the definition of flux averages (see Appendix A), we can derive and separate how the toroidal, poloidal and parallel (to the magnetic field) components of the electric current vary with the kinetic functions $p(\Psi)$ and $F(\Psi)$. We start by taking the dot product of Equation 2.21 with the magnetic field

$$\mathbf{J}\cdot\mathbf{B} = \frac{1}{\mu_0}\left(\nabla F\times\nabla\phi\right)\cdot\mathbf{B} + R\,J_\phi\left(\nabla\phi\cdot\mathbf{B}\right) \Rightarrow \tag{2.31}$$

$$\Rightarrow \mathbf{J}\cdot\mathbf{B} = \frac{1}{\mu_0}\underbrace{\left(\nabla F\times\nabla\phi\right)\cdot\mathbf{B}_\theta}_{\frac{(\nabla F\cdot\nabla\Psi)}{2\pi R^2}} + R\,J_\phi\underbrace{\left(\nabla\phi\cdot\mathbf{B}_\phi\right)}_{\frac{F}{R^2}}. \tag{2.32}$$

Given that $F = F(\Psi)$, its gradient can be calculated as $\nabla F = F'\nabla\Psi$. So

$$\mathbf{J}\cdot\mathbf{B} = \frac{F'}{2\pi R^2\mu_0}\underbrace{\nabla\Psi\cdot\nabla\Psi}_{(2\pi R B_\theta)^2} + \frac{J_\phi F}{R} \Rightarrow \mathbf{J}\cdot\mathbf{B} = F\left(\frac{J_\phi}{R} + \frac{2\pi FF'}{\mu_0 R^2}\frac{B_\theta^2}{B_\phi^2}\right)\times\frac{R_0}{R_0} \Rightarrow \tag{2.33}$$

$$\Rightarrow \frac{\mathbf{J}\cdot\mathbf{B}}{F/R_0} = \frac{J_\phi R_0}{R} + \frac{2\pi}{\mu_0}\frac{R_0}{R^2}\frac{B_\theta^2}{B_\phi^2}FF'. \tag{2.34}$$

Flux averaging Equation 2.34 and remembering that the flux average of any function that depends on Ψ (which is the case for F and consequently FF') yields the function itself, we obtain

$$\frac{\langle \mathbf{J}\cdot\mathbf{B}\rangle}{F/R_0} = \left\langle \frac{J_\phi R_0}{R} \right\rangle + \frac{2\pi}{\mu_0}\left\langle \frac{R_0 B_\theta^2}{R^2 B_\phi^2} \right\rangle FF'. \tag{2.35}$$

The left hand side of the above equation is defined as the averaged parallel-to-**B** current density, j_{par}, while the first term on the right hand side is the averaged toroidal current density, j_{tor}, and the last term on the right hand side is the poloidal component of the current density, j_{pol}. Using equations 2.20 and 2.30, one can obtain how these flux surface averaged components of the current density depend on the kinetic free functions $p(\Psi)$ and $F(\Psi)$:

$$j_{\text{par}} = 2\pi\left(R_0\, p' + \frac{FF'}{\mu_0 R_0}\frac{\langle B^2\rangle}{(F/R_0)^2}\right), \tag{2.36}$$

$$j_{\text{tor}} = 2\pi\left(R_0\, p' + \frac{FF'}{\mu_0 R_0}\left\langle \frac{R_0^2}{R^2}\right\rangle\right), \tag{2.37}$$

$$j_{\text{pol}} = 2\pi\frac{FF'}{\mu_0 R_0}\frac{\langle B_\theta^2\rangle}{(F/R_0)^2}. \tag{2.38}$$

2.3 The TCABR electromagnetic model

The Grad-Shafranov equation described in previous sections represents a force balance equation in the perpendicular-to-**B** direction under the hypothesis of axisymmetry. Given a set of external toroidal currents distribution in the poloidal plane, it finds the solution of the plasma current distribution such that the plasma is an equilibrium state and the pressure gradient force is balanced by the cross product between **J** and **B**. This section provides a model for the evolution of the current in external conductors, and it is assumed that the plasma evolves through a sequence of MHD equilibria represented by the Grad-Shafranov equation. We start by revisiting the basics of mutual inductances between filaments. Suppose we have two loops of wire, at rest, as shown in Figure 2.2. If we run a steady current i_1 around the first loop, it produces a magnetic field $\mathbf{B}_1$, and some of the field lines pass through the second loop. Let Ψ_2 be the flux of $\mathbf{B}_1$ through the second loop,

$$\Psi_2 = \iint_{S_2} \mathbf{B}_1 \cdot d\mathbf{S}_2. \tag{2.39}$$

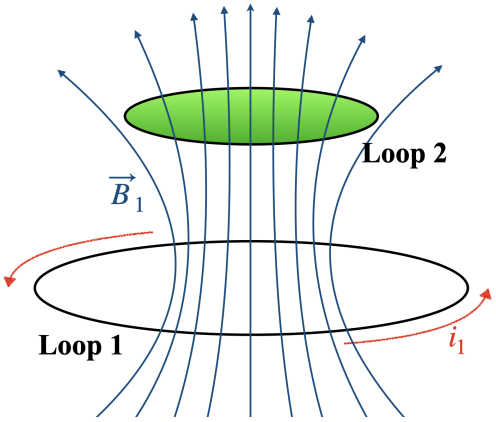

Figure 2.2: Two-wire system.

Depending on the geometry of the filaments, calculating the produced magnetic field $\mathbf{B}_1$ might be a challenge, but a glance at the Biot-Savart law,

$$\mathbf{B}_1 = \frac{\mu_0 i_1}{4\pi} \oint_{\Gamma_1} \frac{d\ell_1 \times (\mathbf{r}_1 - \mathbf{r}_2)}{|\mathbf{r}_1 - \mathbf{r}_2|}, \tag{2.40}$$

revels a significant fact about the field: it is proportional to the electric current i_1. Therefore, so is the flux through the second loop:

$$\Psi_2 = M_{21}\, i_1, \tag{2.41}$$

where

$$M_{21} = \frac{\mu_0}{4\pi} \iint_{S_2} \left[\oint_{\Gamma_1} \frac{d\ell_1 \times (\mathbf{r}_1 - \mathbf{r}_2)}{|\mathbf{r}_1 - \mathbf{r}_2|} \right] \cdot d\mathbf{S}_2 \tag{2.42}$$

is the constant of proportionality known as the mutual inductance between the two loops. The mutual inductance can be written in a better way by using the divergence-free statement of the magnetic field, $\nabla \cdot \mathbf{B}_1 = 0$, and expressing the flux in terms of the magnetic vector potential, $\mathbf{A}_1$, as follows

$$\Psi_2 = \iint_{S_2} (\nabla \times \mathbf{A}_1) \cdot d\mathbf{S}_2 \xRightarrow[\text{theorem}]{\text{Stoke's}} \Psi_2 = \oint_{\partial S_2} \mathbf{A}_1 \cdot d\ell_2. \tag{2.43}$$

Since the magnetic vector potential obeys a Poisson's equation, it can be written as

$$\mathbf{A}_1 = \frac{\mu_0 i_1}{4\pi} \oint \frac{d\ell_1}{|\mathbf{r}_1 - \mathbf{r}_2|}. \tag{2.44}$$

Therefore, the flux can be expressed as

$$\Psi_2 = \left(\frac{\mu_0}{4\pi} \oint \oint \frac{d\ell_1 \cdot d\ell_2}{|\mathbf{r}_1 - \mathbf{r}_2|} \right) i_1 = M_{21}\, i_1, \tag{2.45}$$

which is known as the *Neumann formula*.

For the special case of circular filaments centred around the z-axis, with radii r_1, r_2 and z locations z_1, z_2, the mutual inductance becomes:

$$M_{21} = M_{12} \equiv M(r_1, z_1, r_2, z_2) = \frac{2\mu_0\sqrt{r_1 r_2}}{k}\left[\left(1 - \frac{k^2}{2}\right)\mathscr{K}(k^2) - \mathscr{E}(k^2)\right], \tag{2.46}$$

with $k^2 = \frac{4 r_1 r_2}{(r_1+r_2)^2+(z_1-z_2)^2}$ and $\mathscr{E}(\cdot)$, $\mathscr{K}(\cdot)$ are the complete elliptic integrals of the first and second kind, respectively. Equation 2.46 revels that the mutual inductance is a purely geometrical quantity. The magnetic field per unit of current, in the (r, z) plane, is evaluated using Equations 2.11, 2.12, 2.45 and 2.46.

2.3.1 Modelling active coils

The coil currents in tokamaks are too large for a coil to consist of a single conducting filament. Usually, each of them (PF and Ohmic coils) is made of N_w toroidal wires represented by filamentary windings connected in series such that each filament carries the same electric current I_w, Figure 2.3. The flux generated by a coil a, with N_wa windings and current I_a, at another coil b, with N_wb windings, is given by

$$\Psi = \sum_{i=1}^{N_\mathrm{wa}}\sum_{j=1}^{N_\mathrm{wb}} M(r_j, z_j, r_i, z_i) I_\mathrm{w} = M_\mathrm{ab} I_\mathrm{a}, \tag{2.47}$$

where M_ab is the mutual inductance between the two coils. For a tokamak with N_c PF coils, the evolution of the circuit equations for all the active coils can be written as

$$\begin{aligned} V_1 &= R_1 I_1 + L_1 \dot{I}_1 + \sum_{i=1}^{N_c} M_{1i}\dot{I}_i, \\ &\vdots \\ V_{N_c} &= R_{N_c} I_{N_c} + L_{N_c}\dot{I}_{N_c} + \sum_{i=1}^{N_c-1} M_{N_c i}\dot{I}_i, \end{aligned} \tag{2.48}$$

or in matrix form $\mathbf{V_a} = \mathbf{R_a}\mathbf{I_a} + \mathbf{M_{aa}}\dot{\mathbf{I}}_\mathbf{a}$, where $\mathbf{V_a} \in \mathbb{R}^{N_c\times 1}$, $\mathbf{I_a} \in \mathbb{R}^{N_c\times 1}$ are the applied voltages and the electric currents in each coil, respectively, and

$$\mathbf{M_{aa}} = \begin{pmatrix} L_1 & M_{12} & \dots & M_{1N_c} \\ M_{21} & L_2 & \dots & M_{2N_c} \\ \vdots & \vdots & \ddots & \vdots \\ M_{N_c 1} & M_{N_c 2} & \dots & L_{N_c} \end{pmatrix} \quad \text{and} \quad \mathbf{R_a} = \begin{pmatrix} R_1 & 0 & \dots & 0 \\ 0 & R_2 & \dots & 0 \\ \vdots & \vdots & \ddots & \vdots \\ 0 & 0 & \dots & R_{N_c} \end{pmatrix}, \tag{2.49}$$

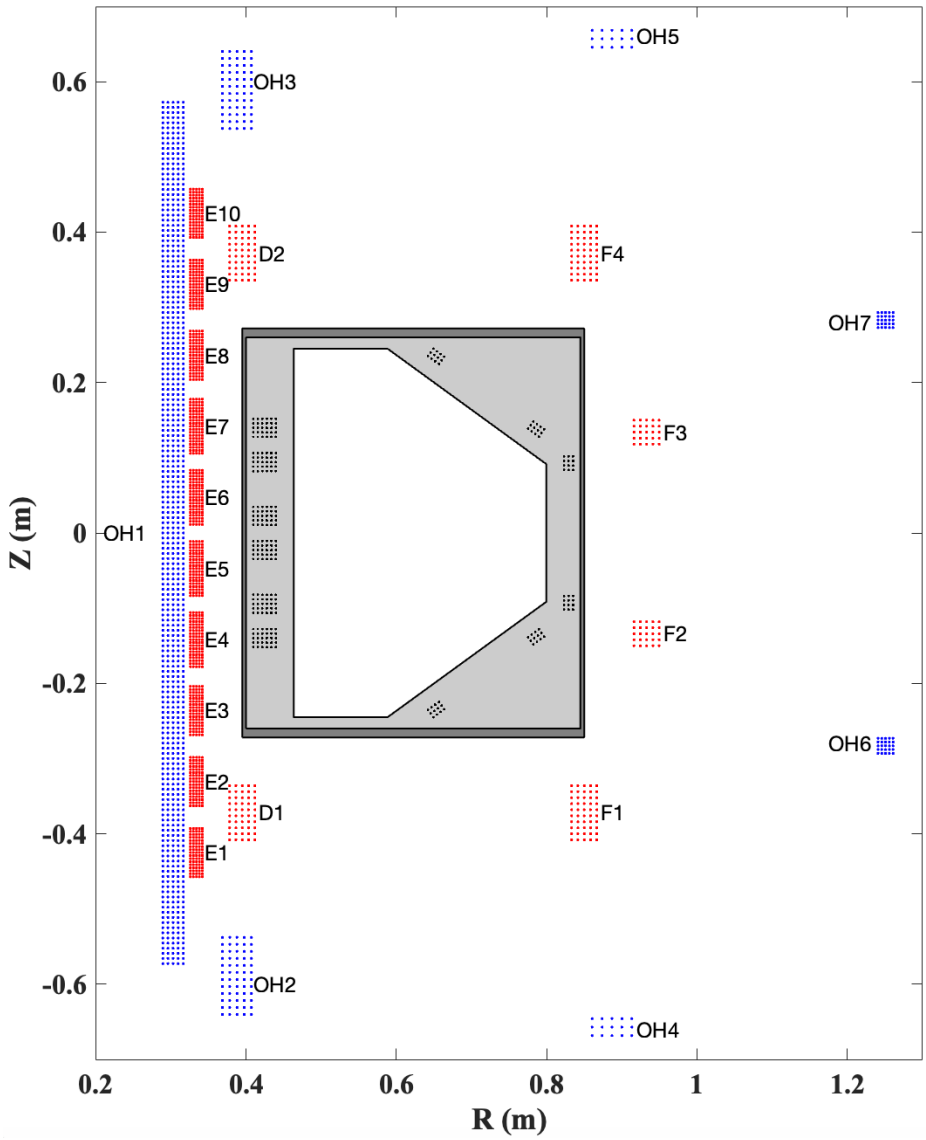

Figure 2.3: Representation of the TCABR coils: the blue filaments belong to the Ohmic coils while the red filaments belong to the PF coils.

with L_n and R_n being the self-inductance and the electric resistance of the coil i, respectively. Since each coil is made of N_w filaments, then we have

$$L_n = \sum_{i=1}^{N_w} L_i + \sum_{i,j,i\neq j}^{N_w} M_{ij}, \quad R_n = \sum_{i=1}^{N_w} R_i, \tag{2.50}$$

with L_i and R_i being the self-inductance and the electric resistance of each filament i, respectively, and M_{ij} the mutual inductance between two filaments of the same coil.

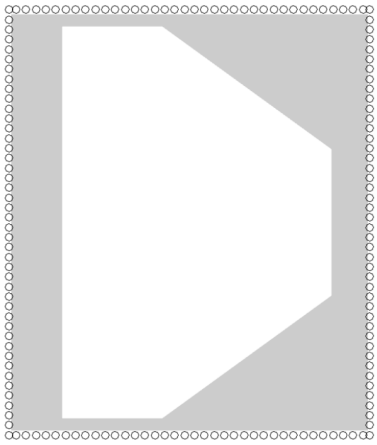

Figure 2.4: Vacuum vessel filament model of TCABR. It is modelled by 160 toroidal filaments represented by the circles. The white area represents the vacuum vessel volume delimited by the graphite tiles walls represented by the grey area.

2.3.2 Modelling the vacuum vessel

Any tokamak experiment takes place inside a vacuum vessel - an hermetically sealed conducting container that houses the plasma and acts as a first safety containment barrier. Also, being a passive structure, it can experience induced currents produced by any temporal changes in magnetic flux. Moreover, it is the vacuum vessel that provides access for diagnostics, heating, and vacuum systems, through its several openings, or ports, making it quite challenging to model. However, if one assumes axisymmetry and ignore the ports, we can assume a continuous vacuum vessel, modelled by a set of N_v individual filaments that can conduct toroidal currents (see Figure 2.4 for the TCABR case).

The total voltage around the vacuum vessel filament is zero, meaning it is a short-circuit, but voltages are induced by changing currents in other components, for example the active coils. The circuit equation for this case is

$$\mathbf{0} = \mathbf{R_v I_v} + \mathbf{M_{vv}}\dot{\mathbf{I}}_\mathbf{v} + \mathbf{M_{va}}\dot{\mathbf{I}}_\mathbf{a}, \tag{2.51}$$

where $\mathbf{M_{vv}} \in \mathbb{R}^{N_v \times N_v}$ is the mutual inductance matrix between the various vacuum vessel filaments, $\mathbf{M_{va}} \in \mathbb{R}^{N_v \times N_c}$ is the mutual inductance matrix between the active coils and the vacuum vessel filaments, $\mathbf{R_v} \in \mathbb{R}^{N_v \times N_v}$ in a diagonal matrix containing the electric resistance of the vessel filaments and $\mathbf{I_v} \in \mathbb{R}^{N_v \times 1}$ is the vector of currents induced in the vessel filaments.

The circuit equation for the active coils ($\mathbf{V_a} = \mathbf{R_a I_a} + \mathbf{M_{aa}}\dot{\mathbf{I}}_\mathbf{a}$) needs to be modified to include the voltage induced by the changing vessel currents:

$$\mathbf{V_a} = \mathbf{R_a I_a} + \mathbf{M_{aa}}\dot{\mathbf{I}}_\mathbf{a} + \mathbf{M_{av}}\dot{\mathbf{I}}_\mathbf{v}. \tag{2.52}$$

Therefore, we can combine Equation 2.51 and Equation 2.52 into

$$\begin{pmatrix} \mathbf{V_a} \\ \mathbf{0} \end{pmatrix} = \begin{pmatrix} \mathbf{M_{aa}} & \mathbf{M_{av}} \\ \mathbf{M_{va}} & \mathbf{M_{vv}} \end{pmatrix} \cdot \begin{pmatrix} \dot{\mathbf{I}}_\mathbf{a} \\ \dot{\mathbf{I}}_\mathbf{v} \end{pmatrix} + \begin{pmatrix} \mathbf{R_a} & 0 \\ 0 & \mathbf{R_v} \end{pmatrix} \cdot \begin{pmatrix} \mathbf{I_a} \\ \mathbf{I_v} \end{pmatrix} \tag{2.53}$$

Eigenmode decomposition

From the circuit equations for the vacuum vessel, Equation 2.51, we can rearrange it to obtain

$$\dot{\mathbf{I}}_\mathbf{v} = \left(-\mathbf{M}_\mathbf{vv}^{-1}\mathbf{R_v}\right)\mathbf{I_v} - \left(\mathbf{M}_\mathbf{vv}^{-1}\mathbf{M_{va}}\right)\dot{\mathbf{I}}_\mathbf{a} \implies \dot{\mathbf{I}}_\mathbf{v} = -\mathbf{A_v}\,\mathbf{I_v} + \mathbf{b_v}\,\dot{\mathbf{I}}_\mathbf{a}, \tag{2.54}$$

where $\mathbf{A_v}$ is a square $n_\mathrm{v} \times n_\mathrm{v}$ matrix with n_v linearly independent eigenvectors q_j. We can factorise this matrix as $\mathbf{A_v} = \mathbf{Q}\cdot\Lambda\cdot\mathbf{Q}^{-1}$, where Λ is a diagonal $n_\mathrm{v} \times n_\mathrm{v}$ matrix with $\Lambda_{j,j} = \lambda_j$ and $\mathbf{Q}$ is the squared $n_\mathrm{v} \times n_\mathrm{v}$ matrix whose j-th column is the eigenvector q_j. Therefore,

$$\dot{\mathbf{I}}_\mathbf{v} = \left(-\mathbf{Q}\cdot\Lambda\cdot\mathbf{Q}^{-1}\right)\mathbf{I_v} - \left(\mathbf{M}_\mathbf{vv}^{-1}\cdot\mathbf{M_{va}}\right)\dot{\mathbf{I}}_\mathbf{a}. \tag{2.55}$$

Neglecting the source terms (second term on the RHS of Equation 2.55),

$$\dot{\mathbf{I}}_\mathbf{v} = -\mathbf{Q}\cdot\Lambda\cdot\left(\mathbf{Q}^{-1}\mathbf{I_v}\right) \implies \mathbf{Q}^{-1}\dot{\mathbf{I}}_\mathrm{v} = -\left(\mathbf{Q}^{-1}\mathbf{Q}\right)\cdot\Lambda\cdot\left(\mathbf{Q}^{-1}\mathbf{I}_\mathrm{v}\right). \tag{2.56}$$

Now we define $\mathbf{I}_\mathrm{u} = \mathbf{Q}^{-1}\mathbf{I}_\mathrm{v} \implies \dot{\mathbf{I}}_\mathrm{u} = \mathbf{Q}^{-1}\dot{\mathbf{I}}_\mathrm{v}$, then we end up with $\dot{\mathbf{I}}_\mathrm{u}(t) = -\Lambda\cdot\mathbf{I}_\mathrm{u}$. This equation is a first-order ODE whose solution is

$$I_\mathrm{u}^j(t) = I_\mathrm{u}^j(0)\,e^{-\lambda_j t} = \alpha_j\,e^{-\lambda_j t} \quad \text{for} \quad j = 1, 2, \ldots, n_\mathrm{v} \tag{2.57}$$

Therefore, the solution $\mathbf{I}_\mathrm{v}(t)$ is

$$\mathbf{I}_\mathrm{v}(t) = \mathbf{Q}\mathbf{I}_\mathrm{u} = \mathrm{V}\mathrm{e}^{-\Lambda t}\alpha = \sum_{j=1}^{n_\mathrm{v}} \alpha_j \mathbf{q}_\mathrm{u}^j \mathrm{e}^{-\lambda_j t} \tag{2.58}$$

where $\mathbf{q}_\mathrm{u}^j$ is the eigenvector in the j-th column of $\mathbf{Q}$. The left panel on Figure 2.5 shows the sorted eigenvalues of the vacuum vessel while the right panel shows their respective eigenvectors. One can notice that the first eigenmode that has the slowest decay has only a positive contribution to the vessel currents, while the others have both positive and negative contributions.

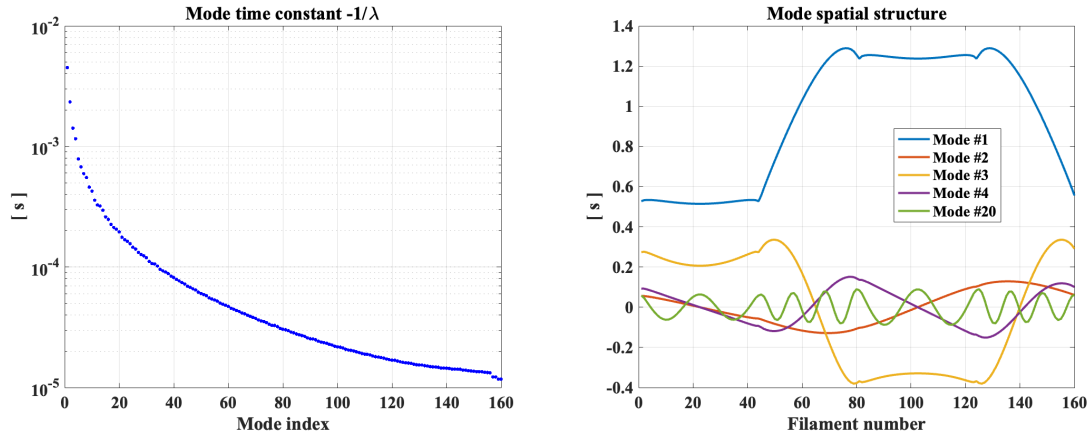

Figure 2.5: Vacuum vessel (left) eigenvalues and (right) eigenvectors.

2.3.3 Modeling the plasma

The plasma is modelled as a rigid body toroidal conductor carrying a electric current I_p. This current is distributed according to a known electric current density distribution $J_\phi(R,Z)$, i.e., $I_p = \iint J_\phi(R,Z)\,dR\,dZ$, as it can be seen in Figure 2.6.

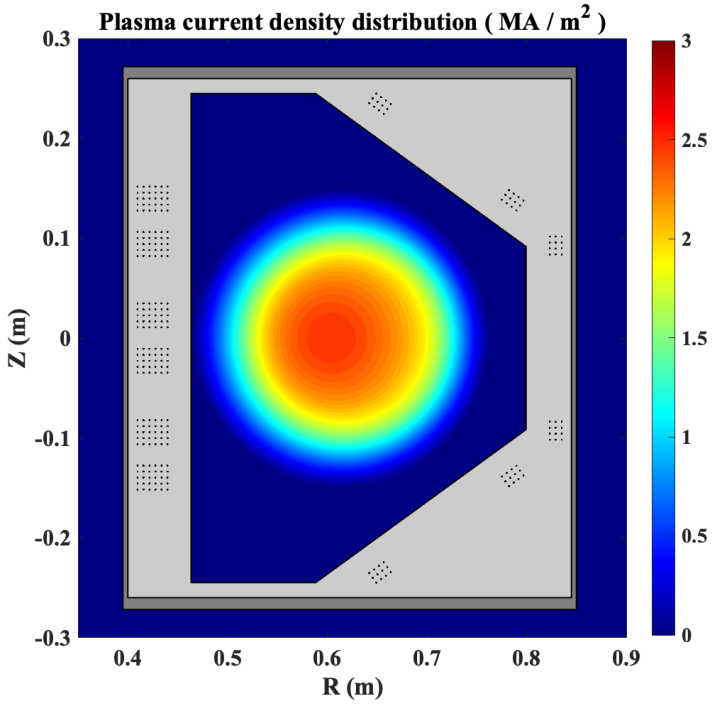

Figure 2.6: Example of a toroidal current distribution $J_\phi(R,Z)$ for TCABR with $I_p = 90$ kA.

The problem we seek to solve is how to calculate the mutual inductance between the plasma

and the current carrying elements - active coils and vacuum vessel filaments. For that, we let J_ϕ be modelled with a current distribution vector $\mathbf{I_x}$ of currents on a (R, Z) grid, with mutual inductance matrix $\mathbf{M_{xx}}$. We then approximate the mutual inductance between the plasma and other conductors as:

$$M_{p\,c_k} = \frac{\sum_x M(r_x, z_x, c_k)\, j_\phi(r_x, z_x)\, \Delta r\, \Delta z}{\sum_x j_\phi(r_x, z_x)\, \Delta r\, \Delta z}, \tag{2.59}$$

with $M(r_x, z_x, c_k)$ being the mutual inductance between the current carrying element c_k and the filament on the grid at the point (r_x, z_x), and $\Delta r\, \Delta z$ is the surface area. Also, since the plasma is treated as a rigid toroidal conductor, it has also a self-inductance feature that can be calculated according to

$$L_p = \frac{\mathbf{I_x}^T \mathbf{M_{xx}}\, \mathbf{I_x}}{I_p^2}. \tag{2.60}$$

Since the plasma is the only conductor that can change its shape, any mutual inductance involving the plasma and the self-inductance itself might change as well. Therefore, the circuit equation for the plasma is then

$$0 = R_p I_p + L_p \dot{I}_p + \dot{L}_p I_p + \mathbf{M_{pa}}\dot{\mathbf{I}}_\mathbf{a} + \dot{\mathbf{M}}_\mathbf{pa}\mathbf{I_a} + \mathbf{M_{pv}}\dot{\mathbf{I}}_\mathbf{v} + \dot{\mathbf{M}}_\mathbf{pv}\mathbf{I_v}, \tag{2.61}$$

where R_p is the plasma resistance which depends on the voltage induced by the ohmic system.

Combining the circuit equations for the active coils, vacuum vessel and the plasma, we obtain

$$\begin{pmatrix} \mathbf{V_a} \\ \mathbf{0} \\ 0 \end{pmatrix} = \begin{pmatrix} \mathbf{M_{aa}} & \mathbf{M_{av}} & \mathbf{M_{ap}} \\ \mathbf{M_{va}} & \mathbf{M_{vv}} & \mathbf{M_{vp}} \\ \mathbf{M_{pa}} & \mathbf{M_{pv}} & L_p \end{pmatrix} \cdot \begin{pmatrix} \dot{\mathbf{I}}_\mathbf{a} \\ \dot{\mathbf{I}}_\mathbf{v} \\ \dot{I}_p \end{pmatrix} + \begin{pmatrix} \mathbf{R_a} & 0 & 0 \\ 0 & \mathbf{R_v} & 0 \\ \dot{\mathbf{M}}_\mathbf{pa} & \dot{\mathbf{M}}_\mathbf{pv} & \dot{L}_p + R_p \end{pmatrix} \cdot \begin{pmatrix} \mathbf{I_a} \\ \mathbf{I_v} \\ I_p \end{pmatrix}. \tag{2.62}$$

This electromagnetic model of a tokamak, coupled with an algorithm that solves Grad-Shafranov equation (Equation 2.30), ensures a better estimation of the time evolution of each coil current and voltage.

The inclusion of the vacuum vessel in the electromagnetic model allow us to predict its impact on the attenuation at the plasma region. In the existing codes, the induced currents are included to the problem a posteriori, while here it is include self-consistently.

3 Numerical methods

This chapter presents the numerical techniques used in this work. We describe the method for inverting the elliptic operator of Grad-Shafranov equation, based on [17]. A brief introduction on the Lagrange multiplier method is provided for which we seek to find the minimum solution for the PF coil currents. Finally, methods to find extremes on 2D surfaces and to solve a first-order differential equation in time are presented.

3.1 Solving the Grad-Shafranov equation

In the following, a technique for discretising Grad-Shafranov equation, Equation 2.30, is discussed to better understand how numerical elliptic equations always reduces to a discrete matrix equation.

Let us consider a common elliptic equation in two dimension (R, Z) for the unknown $\Psi(R, Z)$ in a rectangular domain Ω of the form

$$R^{-\ell}\frac{\partial}{\partial R}\left(R^{\ell}\frac{\partial \Psi}{\partial R}\right)+\frac{\partial^2 \Psi}{\partial Z^2}=S(R,Z), \tag{3.1}$$

where ℓ is a scalar number related with the geometry of the system, $S(R, Z)$ is a known source term, and we are assuming that Dirichlet boundary conditions are given. Since we are interested in a toroidal geometry, ℓ takes the value of -1, which yields the toroidal elliptic operator Δ^*, defined in Equation 2.18. We seek to solve for $\Psi(R, Z)$ in the interior of the domain Ω, given the boundary values

$$\begin{aligned} &\Psi(R_{\min}, Z),\ \Psi(R_{\max}, Z); && R_{\min} \le R \le R_{\max}, \\ &\Psi(R, Z_{\min}),\ \Psi(R, Z_{\max}); && Z_{\min} \le Z \le Z_{\max}. \end{aligned} \tag{3.2}$$

We divide Ω into N intervals of length $\Delta R = (R_{\max} - R_{\min})/N$ in the radial direction and $\Delta Z = (Z_{\max} - Z_{\min})/N$ in the vertical direction.

Now, we adopt the following notation for the discrete positions:

$$\begin{aligned} R_i &= R_{\min} + (i-1)\,\Delta R; & i &= 1, ..., N+1, \\ Z_j &= Z_{\min} + (j-1)\,\Delta Z; & j &= 1, ..., N+1, \\ \Psi_{i,j} &= \Psi(R_i, Z_j); & S_{i,j} &= S(R_i, Z_j). \end{aligned} \tag{3.3}$$

The second-order finite difference equation, accurate to second order in ΔR and ΔZ, derived by a Taylor series expansion, is given by

$$\Psi_{i,j+1} + a_i \Psi_{i+1,j} + b_i \Psi_{i-1,j} - (2 + c_i)\Psi_{i,j} + \Psi_{i,j-1} = \Delta Z^2 S_{i,j}, \tag{3.4}$$

where we define the coefficients

$$\begin{aligned} a_i &= \left(\frac{\Delta Z}{\Delta R}\right)^2 \left(1 - \frac{\Delta R/2}{R_i}\right), \\ b_i &= \left(\frac{\Delta Z}{\Delta R}\right)^2 \left(1 + \frac{\Delta R/2}{R_i}\right), \\ c_i &= a_i + b_i. \end{aligned} \tag{3.5}$$

Equation 3.4 forms a tri-diagonal matrix, where it has only three diagonal bands of non-zero matrices. To visualise that, for each j index, we define a vector of length $N+1$ that contains the unknowns with the same j as follows:

$$\vec{\Psi}_j = \begin{bmatrix} \Psi_{1,j} \\ \Psi_{2,j} \\ \vdots \\ \Psi_{N+1,j} \end{bmatrix} \quad \rightarrow \quad \Psi = \begin{bmatrix} \Psi_{1,1} & \Psi_{1,2} \dots \Psi_{1,N+1} \\ \Psi_{2,1} & \Psi_{2,2} \dots \Psi_{2,N+1} \\ \vdots & \ddots \\ \Psi_{N+1,1} & \Psi_{N+1,2} \dots \Psi_{N+1,N+1} \end{bmatrix} \tag{3.6}$$

Therefore, Equation 3.4 can be written in the block form

$$\mathbf{A}_j \cdot \vec{\Psi}_{j+1} - \mathbf{B}_j \cdot \vec{\Psi}_j + \mathbf{C}_j \cdot \vec{\Psi}_{j-1} = \mathbf{D}_j. \tag{3.7}$$

Here, $\mathbf{B}_j$ is a tri-diagonal $N+1 \times N+1$ matrix involving the coefficients a_i, b_i, and c_i defined in Equation 3.5, $\mathbf{A}_j$ and $\mathbf{C}_j$ are both modified $N+1 \times N+1$ identity matrices, and $\mathbf{D}_j$ is a $N+1 \times 1$ vector that contains both Dirichlet boundary values and the source term. The matrices in Equation 3.7 are, therefore, of the form:

$$\mathbf{A}_j = \mathbf{C}_j = \begin{bmatrix} 0 & & \\ & [\mathbb{1}] & \\ & & 0 \end{bmatrix}, \quad \mathbf{B}_j = \begin{bmatrix} -1 & & & & & & \\ -b_2 & 2+c_2 & -a_2 & & & & \\ & -b_3 & 2+c_3 & -a_3 & & & \\ & & & \ddots & & & \\ & & & -b_N & 2+c_N & -a_N & \\ & & & & & -1 & \end{bmatrix}, \tag{3.8}$$

for $j = 2, ..., N$ and $[\mathbb{1}]$ is a $(N-1) \times (N-1)$ identity matrix. The boundary values, i.e. $j = 1$ and for $j = N$, are of the form: $\mathbf{A}_1 = \mathbf{A}_{N+1} = \mathbf{C}_1 = \mathbf{C}_{N+1} = \mathbb{O}$, and $\mathbf{B}_1 = \mathbf{B}_{N+1} = -\mathbb{1}$. For the $\mathbf{D}$ matrix, we choose its boundary values as being the known Dirichlet boundary conditions to Ψ, and its interior as being the right-hand-side of Equation 3.4. To solve Equation 3.7, we look to find the square $N+1 \times N+1$ matrices $\mathbf{E}_j$ and the $N+1 \times 1$ vectors $\mathbf{F}_j$ such that satisfy the first-order difference equation:

$$\vec{\Psi}_j = \mathbf{E}_j \cdot \vec{\Psi}_{j+1} + \mathbf{F}_j, \tag{3.9}$$

or, for $j \to j-1$,

$$\vec{\Psi}_{j-1} = \mathbf{E}_{j-1} \cdot \vec{\Psi}_j + \mathbf{F}_{j-1}. \tag{3.10}$$

Plugging $\vec{\Psi}_{j-1}$ from Equation 3.10 into Equation 3.7 we get

$$\vec{\Psi}_j = \left(\left[\mathbf{B}_j - \mathbf{C}_j \cdot \mathbf{E}_{j-1} \right]^{-1} \cdot \mathbf{A}_j \right) \cdot \vec{\Psi}_{j+1} + \left[\mathbf{B}_j - \mathbf{C}_j \cdot \mathbf{E}_{j-1} \right]^{-1} \cdot \left(\mathbf{C}_j \cdot \mathbf{F}_{j-1} - \mathbf{D}_j \right), \tag{3.11}$$

and comparing it with Equation 3.9, we find that $\mathbf{E}_j$ and $\mathbf{F}_j$ must obey the following recurrence relations:

$$\mathbf{E}_j = \left[\mathbf{B}_j - \mathbf{C}_j \cdot \mathbf{E}_{j-1} \right]^{-1} \cdot \mathbf{A}_j, \tag{3.12}$$

$$\mathbf{F}_j = \left[\mathbf{B}_j - \mathbf{C}_j \cdot \mathbf{E}_{j-1} \right]^{-1} \cdot \left(\mathbf{C}_j \cdot \mathbf{F}_{j-1} - \mathbf{D}_j \right). \tag{3.13}$$

Once calculated $\mathbf{E}$ and $\mathbf{F}$, one can manipulate the above equations in order to obtain

$$\vec{\Psi}_N = \mathbf{F}_N + \mathbf{E}_N \cdot \mathbf{D}_{N+1}, \tag{3.14}$$

and Equation 3.9 can be used to calculate the rest of the solution by backward calculations from $j = N-1$ to $j = 2$.

3.2 The Lagrange multipliers method

The method of Lagrange multipliers - named after the Italian mathematician Joseph-Louis Lagrange - is a technique in mathematical optimisation for finding the maxima and minima of a function subjected to some constraints on the input values.

Let $f(\mathbf{x})$ be a N_f-dimensional function subjected to N_c constraints $g_i(\mathbf{x}) = c_i$. The idea of the method is to look for points where the contour lines of the functions f and g are tangent to each other. Or, equivalently, to find where the gradient vectors of both functions are parallel to each other.

We start by defining the Lagrange function as

$$\mathscr{L}(\mathbf{x},\lambda) = f(\mathbf{x}) - \sum_{i=1}^{N_c} \lambda_i \left(g_i(\mathbf{x}) - c_i\right), \tag{3.15}$$

where λ is the Lagrange multipliers. In order to find the critical points of the Lagrange function, we calculate

$$\nabla\mathscr{L}(\mathbf{x},\lambda) = \left(\sum_{i=1}^{N_f} \frac{\partial\mathscr{L}}{\partial x_i} + \sum_{j=1}^{N_c} \frac{\partial\mathscr{L}}{\partial\lambda_j}\right)\hat{e}_{x_i} = 0. \tag{3.16}$$

After obtaining the solutions of Equation 3.16, which will look something like $(\mathbf{x}_0,\lambda_0)$, the one that gives the greatest/smallest value of the function $f(\mathbf{x}_0)$ provides actually its maximum/minimum, respectively. This technique will be used to calculate the minimum PF coil currents for a desired plasma scenario.

3.3 The Newton-Raphson method

After finding the solution of Grad-Shafranov equation for a given boundary condition, i.e. after finding $\Psi = \Psi(R,Z)$, we need to define the normalised poloidal flux, Ψ_N, defined by

$$\Psi_N = \frac{\Psi - \Psi_{\text{axis}}}{\Psi_{\text{LCFS}} - \Psi_{\text{axis}}}, \tag{3.17}$$

where Ψ_{axis} and Ψ_{LCFS} are the values of the poloidal flux at the magnetic axis and at the last closed flux surface, respectively. It is important to define this scalar quantity once the kinetic profiles will be defined later as functions of Ψ_N. The magnetic axis is obtained by finding the critical points that has the extrema of the solution. This is done by finding the points $(R_{\text{axis}}, Z_{\text{axis}})$ that satisfies

$$\begin{aligned} &\nabla\Psi\Big|_{(R_{\text{axis}},Z_{\text{axis}})} = 0 \\ &\det\mathscr{H}(\Psi)\Big|_{(R_{\text{axis}},Z_{\text{axis}})} > 0, \end{aligned} \tag{3.18}$$

with $\mathscr{H}(\Psi)$ being the Hessian of the solution, given by $\mathscr{H}(\Psi) \equiv \frac{\partial^2\Psi}{\partial R^2}\frac{\partial^2\Psi}{\partial Z^2} - \frac{\partial^2\Psi}{\partial R\partial Z}\frac{\partial^2\Psi}{\partial Z\partial R}$.

The last closed flux surface solution has two possible meanings, as explained in the introduction section. If the plasma is limited, the Ψ_{LCFS} is the flux on the limiter that reaches the maximum or minimum value, depending on the direction of the plasma current. For $I_p > 0$,

$$\Psi_{\text{LCFS}}(R_{\text{lim}}, Z_{\text{lim}}) = \max_{(R,Z)\in\partial\Omega_p} \Psi. \tag{3.19}$$

However, in a diverted plasma, the Ψ_{LCFS} is the flux that passes through a hyperbolic point

(saddle point or X-point). This is done by finding the points $(R_{\text{sep}}, Z_{\text{sep}})$ that satisfy

$$\begin{aligned} &\nabla\Psi\Big|_{(R_{\text{sep}},Z_{\text{sep}})} = 0 \\ &\det\mathscr{H}(\Psi)\Big|_{(R_{\text{sep}},Z_{\text{sep}})} < 0. \end{aligned} \tag{3.20}$$

Therefore, we need to find the points (R, Z) that satisfies $\nabla\Psi = 0$, i.e. one needs to find the roots of $\nabla\Psi$. One of the several methods for finding the roots of a two-dimensional function is the so-called Newton-Raphson's method, and its demonstration is based on [18].

Let $\mathbf{f}(R,Z) = f_R(R,Z)\hat{e}_R + f_Z(R,Z)\hat{e}_Z \equiv \nabla\Psi(R,Z)$ be the two variables vectorial function we seek to find its roots $(\mathbf{x}_0 = R_0, Z_0)$. Applying Taylor's expansion up to first order, we obtain

$$\begin{aligned} f_R(R,Z) &= f_R(\mathbf{x}_0) + (R-R_0)\frac{\partial f_R}{\partial R}\Big|_{\mathbf{x}_0} + (Z-Z_0)\frac{\partial f_R}{\partial Z}\Big|_{\mathbf{x}_0}, \\ f_Z(R,Z) &= f_Z(R_0,Z_0) + (R-R_0)\frac{\partial f_Z}{\partial R}\Big|_{\mathbf{x}_0} + (Z-Z_0)\frac{\partial f_Z}{\partial Z}\Big|_{\mathbf{x}_0}. \end{aligned} \tag{3.21}$$

The terms on the left-hand side are zero by definition. Denoting $\mathbf{x} = (R, Z)$, we obtain in matrix form,

$$\mathbf{0} = \mathbf{f}(\mathbf{x_0}) + \mathbf{F}(\mathbf{x_0}) \cdot (\mathbf{x} - \mathbf{x_0}), \tag{3.22}$$

where

$$\mathbf{F}(\mathbf{x_0}) = \begin{bmatrix} \frac{\partial f_R}{\partial R} & \frac{\partial f_R}{\partial z} \\ \frac{\partial f_Z}{\partial R} & \frac{\partial f_Z}{\partial z} \end{bmatrix}\Bigg|_{\mathbf{x}_0}$$

is the Jacobian matrix of $\mathbf{f}$ at $\mathbf{x_0}$. If the initial guess $\mathbf{x_0}$ is close enough to the actual root and $\det[\mathbf{F}(\mathbf{x_0})] \neq 0$, then

$$\mathbf{x} = \mathbf{x_0} - \mathbf{F}^{-1}(\mathbf{x_0}) \cdot \mathbf{f}(\mathbf{x_0}) \equiv \mathbf{x_1} \tag{3.23}$$

$\mathbf{x_1}$ is an improvement on $\mathbf{x_0}$. Therefore, this leads to an iterative method

$$\mathbf{x}_{n+1} = \mathbf{x}_n - \mathbf{F}_n^{-1} \cdot \mathbf{f}_n \tag{3.24}$$

that converges when $|\nabla\Psi(\mathbf{x}_{n+1})|$ is numerically zero.

3.4 The Crank-Nicholson method

When we derived the electromagnetic model for TCABR (Equation 2.62), we gathered three main systems: the plasma, the vacuum vessel and the active coils. The latter being the Ohmic system and the PF coils. As said previously, we calculate the currents in the PF coils using the Lagrange method, where we find the solution that minimises their currents. Here, we seek to solve the time evolution of the Ohmic and vacuum vessel currents. For that, we deploy

the short-circuit equations, i.e., the plasma and vacuum vessel equations. We start by first denoting the sub-index a representing only the active PF coils. Therefore, the circuit equation for the plasmas becomes

$$0 = R_p I_p + L_p \dot{I}_p + M_{p,OH}\dot{I}_{OH} + \dot{M}_{p,OH} I_{OH} + M_{p,a}\dot{I}_a + \dot{M}_{p,a} I_a + M_{p,v}\dot{I}_v + \dot{M}_{p,v} I_v, \quad (3.25)$$

and the circuit equation for the vessel

$$0 = R_v I_v + M_{v,v}\dot{I}_v + M_{v,OH}\dot{I}_{OH} + M_{v,a}\dot{I}_a + M_{v,p}\dot{I}_p + \dot{M}_{v,p} I_p. \quad (3.26)$$

In matrix form, the above equation becomes

$$\begin{bmatrix} M_{p,OH} & M_{p,v} \\ M_{v,OH} & M_{v,v} \end{bmatrix} \cdot \begin{bmatrix} \dot{I}_{OH} \\ \dot{I}_v \end{bmatrix} + \begin{bmatrix} \dot{M}_{p,OH} & \dot{M}_{p,v} \\ 0 & R_v \end{bmatrix} \cdot \begin{bmatrix} I_{OH} \\ I_v \end{bmatrix} = \begin{bmatrix} -R_p I_p - L_p \dot{I}_p - M_{p,a}\dot{I}_a - \dot{M}_{p,a} I_a \\ -M_{v,a}\dot{I}_a - M_{v,p}\dot{I}_p - \dot{M}_{v,p} I_p \end{bmatrix}. \quad (3.27)$$

We realize that this equation can be written in a more appropriate way such as

$$\dot{\mathbf{I}} = -\left(\mathbf{M}^{-1} \cdot \mathbf{R}\right) \mathbf{I} + \mathbf{M}^{-1} \cdot \mathbf{S}, \quad (3.28)$$

where

$$\mathbf{I} = \begin{bmatrix} I_{OH} \\ I_v \end{bmatrix}, \quad \mathbf{M} = \begin{bmatrix} M_{p,OH} & M_{p,v} \\ M_{v,OH} & M_{v,v} \end{bmatrix}, \quad \mathbf{R} = \begin{bmatrix} \dot{M}_{p,OH} & \dot{M}_{p,v} \\ 0 & R_v \end{bmatrix}, \quad \text{and}$$

$$\mathbf{S} = \begin{bmatrix} -R_p I_p - L_p \dot{I}_p - M_{p,a}\dot{I}_a - \dot{M}_{p,a} I_a \\ -M_{v,a}\dot{I}_a - M_{v,p}\dot{I}_p - \dot{M}_{v,p} I_p \end{bmatrix}.$$

To solve this first-order differential equation, we can use the Crank-Nicholson method, which is based on the Euler method (forward and backwards), and it is described as follows. Suppose an ordinary differential equation such as

$$\frac{dy}{dt} = F\left(y, t\right). \quad (3.29)$$

The forward Euler method relates the solution at the $n+1$ time step, given the previous one

$$\frac{y^{n+1} - y^n}{\Delta t} = F^n(y, t), \quad (3.30)$$

while the backward Euler method relates the solution given the source term also at the $n+1$ time step,

$$\frac{y^{n+1} - y^n}{\Delta t} = F^{n+1}(y, t). \quad (3.31)$$

Therefore, combining both methods, we obtain

$$\frac{y^{n+1}-y^n}{\Delta t} = \frac{1}{2}\left[F^{n+1}(y,t)+F^n(y,t)\right]. \tag{3.32}$$

This is an implicit method, meaning that in order to get the next solution of y in time, one must solve a system of algebraic equation. Let us now apply this method to Equation 3.28. We start by denoting $\mathbf{A} \equiv \mathbf{M}^{-1}\cdot\mathbf{R}$ and $\mathbf{B} \equiv \mathbf{M}^{-1}\cdot\mathbf{S}$. Then, our equation becomes

$$\frac{\mathbf{I}^{n+1}-\mathbf{I}^n}{\Delta t} = \frac{1}{2}\left(-\mathbf{A}^{n+1}\mathbf{I}^{n+1}+\mathbf{B}^{n+1}-\mathbf{A}^n\mathbf{I}^n+\mathbf{B}^n\right) \Longrightarrow$$

$$\left(\mathbb{1}+\frac{\Delta t}{2}\mathbf{A}^{n+1}\right)\mathbf{I}^{n+1} = \left(\mathbb{1}-\frac{\Delta t}{2}\mathbf{A}^n\right)\mathbf{I}^n+\frac{\Delta t}{2}\left(\mathbf{B}^{n+1}+\mathbf{B}^n\right),$$

and, therefore, we obtain

$$\mathbf{I}^{n+1} = \left(\mathbb{1}+\frac{\Delta t}{2}\mathbf{A}^{n+1}\right)^{-1}\left(\mathbb{1}-\frac{\Delta t}{2}\mathbf{A}^n\right)\mathbf{I}^n+\frac{\Delta t}{2}\left(\mathbb{1}+\frac{\Delta t}{2}\mathbf{A}^{n+1}\right)^{-1}\left(\mathbf{B}^{n+1}+\mathbf{B}^n\right). \tag{3.33}$$

Solving this equation will give us the evolution of the Ohmic and vacuum vessel currents. As an example, Figure 3.1 shows the solution of Equation 3.33 for the Ohmic and first four vacuum vessel eigenmode currents (see Figure 2.5 for details).

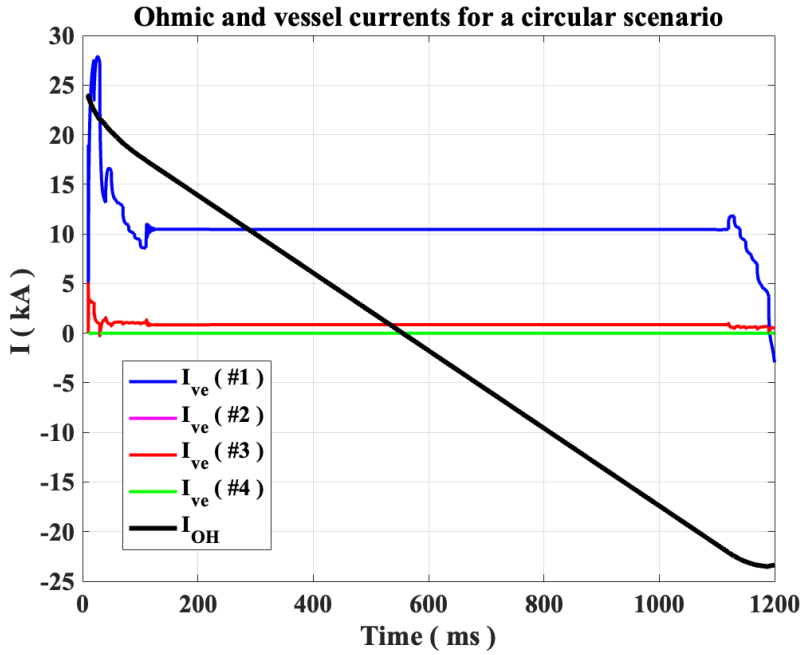

Figure 3.1: Time evolution of the Ohmic and vacuum vessel currents for a circular plasma scenario.

4 The Plasma Scenario Design code

Over the years, different types of codes have been written for solving the MHD equilibrium problem. This chapter serves to introduce some of the possible Grad-Shafranov solvers and to describe in detail the Plasma Scenario Design (PSD) code, an inverse Grad-Shafranov solver fully developed in the Plasma Physics Laboratory of the Institute of Physics of the University of São Paulo using the MATLAB software to determine the evolution of the active coil currents and voltages for several plasma shapes.

4.1 Computational domains

For a better understanding, it is useful to specify the sub-domains of the (R, Z) plane used in this work, Table 4.1.

Ω	(R, Z) plane
Ω_c	Computational domain
Ω_{pl}	Plasma region
Ω_v	Vessel region
Ω_a	Active coils region
Ω_{vac}	Vacuum region within Ω_c

Table 4.1

The computational domain, Ω_c, is where the Grad-Shafranov equation (Equation 2.30) is sought and it is represented with a rectangular grid enclosed by its boundary $\partial\Omega_c$. The plasma region, Ω_{pl}, is contained within the LCFS, already defined in the Section 1.2. The vessel and active coils regions $(\Omega_v + \Omega_a)$ are the regions that contain toroidal electric current outside the plasma domain. Finally, the vacuum region, Ω_{vac}, is the one that do not contain toroidal electric current. All the above domains can be seen in Figure 4.1.

As mentioned before, the Grad Shafranov equation is a second-order partial differential equation. Therefore, to solve it, the profiles $p'(\Psi)$ and $FF'(\Psi)$ and the boundary conditions at

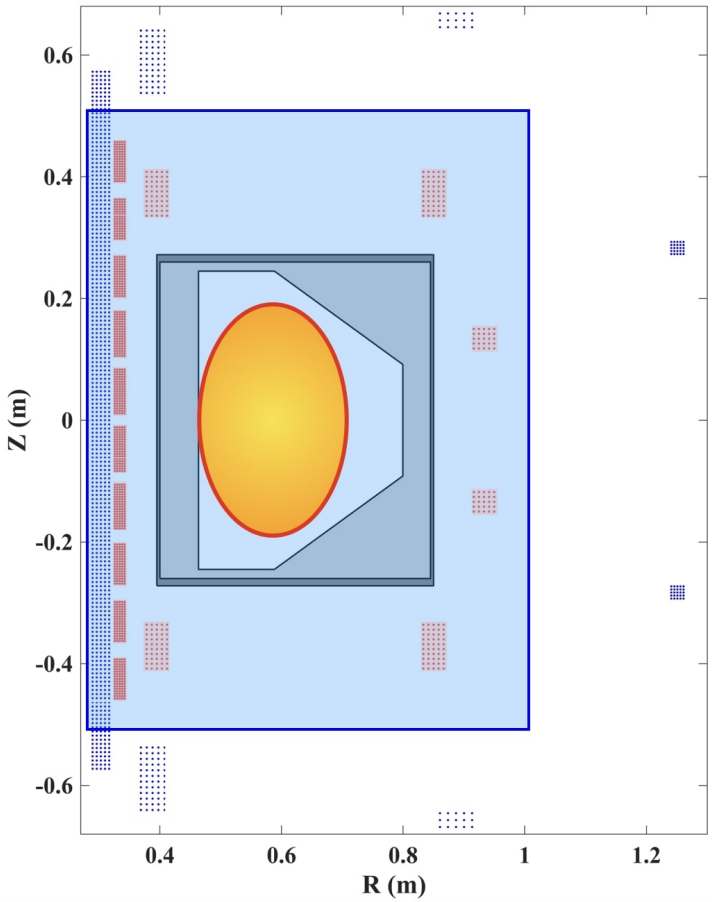

Figure 4.1: Computational domains in the poloidal plane of TCABR: Plasma domain Ω_{pl} (yellowish region) delimited by the LCFS (continuous red line); The computational domain Ω_c (blueish region) composed by the plasma and the vacuum vessel (dark-grey region) domains, and delimited by its boundary (continuous blue line); Active coils region (reddish region).

the computational boundary must be specified. One can distinguish between two cases: the so-called free-boundary case, where the LCFS location is found as part of the solution, and the so-called fixed-boundary case, where the location of the LCFS is prescribed. In the following section, an iterative method to solve Grad-Shafranov and the three types of problems one might be interested is presented.

4.2 Iterative Picard method

A popular method to treat the non-linearity in the Grad-Shafranov equation is to successively iterate between the current distribution and the poloidal flux distribution. The method starts, let us say, at the step $[n-1]$ with a given plasma current density $J_\phi^{[n-1]}$ and external active and passive currents embedded in $I_e^{[n-1]}$. The next step $[n]$ is obtained by the following steps:

1. Compute the boundary flux $\Psi_b = \Psi_{b,p}\left(j_\phi^{[n-1]}\right) + M_{b,e}\, I_e^{[n-1]}$ on $\partial\Omega_c$;

2. Solve the Grad-Shafranov equation (Equation 2.20) $\Delta^* \Psi^{[n]} = -2\pi\mu_0 R j_\phi^{[n-1]}$ in Ω_c using the technique described in Section 3.1;

3. Find the plasma domain Ω_{pl}, i.e. calculate the Ψ_{axis} and Ψ_{LCFS} using the techniques described in Section 3.3;

4. Update the external currents $I_e^{[n]}$ and kinetic profiles $p'^{[n]}$, $FF'^{[n]}$.

5. Update the plasma current density $j_\phi^{[n]} = 2\pi \left[R p' \left(\Psi^{[n]} \right) + FF' \left(\Psi^{[n]} \right) / \left(\mu_0 R \right) \right]$;

6. Test the convergence criteria.

The fourth step of the Picard iteration can be adapted to fit a specific goal of the equilibrium solver as we will see in the following.

Equilibrium reconstruction

This solver takes as input the measurements, such as flux loops, magnetic probes, poloidal field coil currents, diamagnetic flux, among others, and provides the kinetic profiles $p'(\Psi)$ and $FF'(\Psi)$, and the magnetic equilibrium $\Psi(R, Z)$. Usually, this is done by solving a least-square problem of the type

$$\chi = \min_{p', FF', \mathbf{I_a}, \mathbf{I_v}} \left\{ \sum_j \left| \mathbf{y_j} - \mathbf{h_j} \left[\Psi(R, Z) \right] \right|^2 \right\},$$

where $\mathbf{y_j}$ is a vector containing real measurements and $\mathbf{h_j} \left[\Psi(R, Z) \right]$ contains synthetic measurements. In many tokamaks, equilibrium reconstruction is commonly solved during or after discharges to reconstruct the plasma equilibrium evolution in time during an experiment [22].

Fixed boundary equilibrium solver

This solver takes as input the exact plasma boundary $\partial\Omega_{\text{pl}}$ and the kinetic profiles $p'(\Psi)$ and $FF'(\Psi)$. Its output is the plasma equilibrium solution $\Psi(R, Z, t)$. This allows for the study of equilibrium stability, controller design, among others.

Free boundary equilibrium solver

This solver takes as input the desired plasma boundary $\partial\Omega_{\text{pl}}$ and provides the minimum required PF coil currents. This approach is used during the preparation of an experiment to determine the sequence of $\mathbf{I_a}$ to get the desired plasma shape at a sequence of pre-defined times. Typically it is assumed a nearly steady-state equilibrium. During the Picard iterations, the PF coil currents are updated by solving a least-square problem as will be explained later in this section, and the kinetic profiles are chosen to satisfy some constraints based on some scalar equilibrium features. Additional constraints can be added in the optimisation process

[23]. This is the solver we are interested in this work and it will be explained in details in the following.

4.3 The free boundary equilibrium solver

In this Section, a detailed description of each step of the free boundary equilibrium solver is given. For convenience, it is divided into subsections. For our case, we will adapt the general Picard algorithm as follows:

1. Prescribe boundary points along the desired LCFS;
2. Provide an initial guess for the plasma current density $j_\phi^{[n-1]}(R,Z)$ and calculate the associated poloidal flux;
3. Adjust the PF coil currents to obtain the prescribed LCFS;
4. Compute the boundary flux $\Psi_b = \Psi_{b,p}\left(j_\phi^{[n-1]}\right) + M_{b,e}\, I_e^{[n-1]}$ on $\partial\Omega_c$;
5. Solve the Grad-Shafranov equation (Equation 2.20) $\Delta^*\Psi^{[n]} = -2\pi\mu_0 R j_\phi^{[n-1]}$ in Ω_c;
6. Find the plasma domain in order to calculate the normalised flux Ψ_N;
7. Parameterise the kinetic profiles as functions of the normalised flux, i.e. $p(\Psi_N)$, and $F(\Psi_N)$ to update the plasma current density.
8. Test the convergence criteria.

4.3.1 Prescribing the plasma boundary and constraint points

The boundary of the plasma can be parameterised from an analytical expression of the LCFS [19] by prescribing the elongation, κ, the triangularity, δ, and the squareness, ζ:

$$\begin{aligned} R_b(\theta) &= R_0 + a\cos\left(\theta + \delta\sin\theta - \zeta\sin 2\theta\right), \\ Z_b(\theta) &= Z_0 + \kappa a\sin\left(\theta + \zeta\sin 2\theta\right), \end{aligned} \tag{4.1}$$

where (R_0, Z_0), a, and θ are the location of the plasma magnetic axis, the plasma minor radius, and a poloidal angle, respectively. Figure 4.2 shows some examples of boundary shapes obtained from Equation 4.1.

The confinement time and global plasma performance are intrinsically connected with the plasma shape. For instance, high values of κ allows higher plasma current and, consequently, extends the ideal MHD stability limits [20]. However, elongated plasmas are vertically unstable, requiring a robust control system to create such configurations. Besides prescribing the plasma boundary using Equation 4.1, one can also set exact points in the (R,Z) plane where we impose some constraints to the magnetic field.

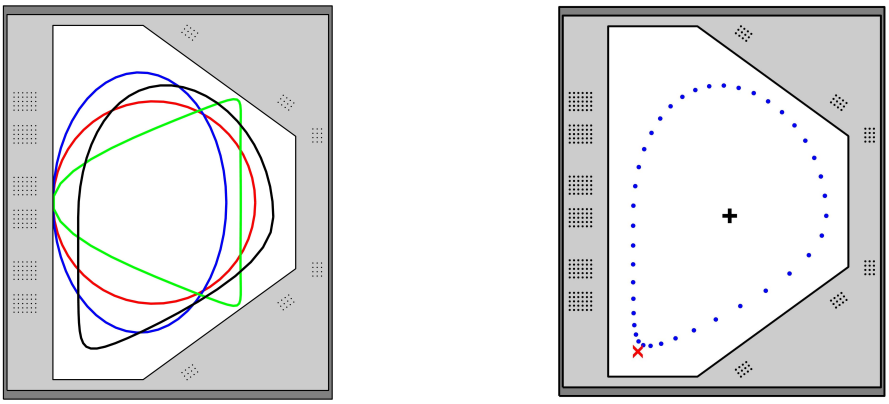

(a) (b)

Figure 4.2: (a) Examples of plasma boundaries obtained from Equation 4.1: circular (red line), elongated (blue line), with negative triangularity (green line) and with an X-point (black line). (b) Example of a prescribed plasma boundary with an X-points imposed (red cross).

Below one can find a few examples of constraints:

- Vertical tangency (outboard or inboard midplane) at $(R_\mathrm{r}, Z_\mathrm{r})$:

$$B_R(R_\mathrm{r}, Z_\mathrm{r}) = -\frac{1}{2\pi R}\frac{\partial \Psi}{\partial Z}\bigg|_{(R_\mathrm{r}, Z_\mathrm{r})} = 0;$$

- Horizontal tangency (plasma bottom or top) at (R_z, Z_z):

$$B_Z(R_\mathrm{z}, Z_\mathrm{z}) = \frac{1}{2\pi R}\frac{\partial \Psi}{\partial R}\bigg|_{(R_\mathrm{z}, Z_\mathrm{z})} = 0;$$

- First order null-point (magnetic axis or X-point) at $(R_\mathrm{xp}, Z_\mathrm{xp})$:

$$B_R(R_\mathrm{xp}, Z_\mathrm{xp}) = -\frac{1}{2\pi R}\frac{\partial \Psi}{\partial Z}\bigg|_{(R_\mathrm{xp}, Z_\mathrm{xp})} = 0 \quad \text{and} \quad B_Z(R_\mathrm{xp}, Z_\mathrm{xp}) = \frac{1}{2\pi R}\frac{\partial \Psi}{\partial R}\bigg|_{(R_\mathrm{xp}, Z_\mathrm{xp})} = 0;$$

- Second order null-point (snowflake) at $(R_\mathrm{sf}, Z_\mathrm{sf})$:

$$B_R(R_\mathrm{sf}, Z_\mathrm{sf}) = -\frac{1}{2\pi R}\frac{\partial \Psi}{\partial Z}\bigg|_{(R_\mathrm{sf}, Z_\mathrm{sf})} = 0 \quad \text{and} \quad B_Z(R_\mathrm{sf}, Z_\mathrm{sf}) = \frac{1}{2\pi R}\frac{\partial \Psi}{\partial R}\bigg|_{(R_\mathrm{sf}, Z_\mathrm{sf})} = 0;$$
$$\frac{\partial B_R}{\partial R}\bigg|_{(R_\mathrm{sf}, Z_\mathrm{sf})} = 0 \quad \text{and} \quad \frac{\partial B_R}{\partial Z}\bigg|_{(R_\mathrm{sf}, Z_\mathrm{sf})} = 0;$$

To have a second order null-point one must have $B_R = B_Z = \nabla B_R = \nabla B_Z = 0$. For that, one can use the fact that $\nabla \times \mathbf{B} = 0$ and $\nabla \cdot \mathbf{B} = 0$ at the null-point to find out that one just have to impose $\partial B_R/\partial R = \partial B_R/\partial Z = 0$, in addition to $B_R = B_Z = 0$, to have a second order null-point.

4.3.2 Initial guess for the plasma current density and its poloidal magnetic flux

With the boundary points given by Equation 4.1 in hand, we can prescribe an initial guess for the plasma current density within the desired LCFS. In our case, we set the initial guess for the plasma current density as a flat profile across the LCFS domain, Figure 4.3a, such that its integral over the two-dimensional grid yields the prescribed plasma current, i.e.

$$I_p = \iint_{\Omega_p} J_\phi^0(R,Z)\, dR\, dZ.$$

With this initial guess, we can calculate the associated poloidal flux using the Green's functions

$$\Psi_p(R,Z) = \int M(R,Z;R',Z')\, J_\phi^0(R',Z')\, dR'\, dZ' \tag{4.2}$$

where $M(R,Z;R',Z')$ is given by Equation 2.46. Figure 4.3b shows an example of the associated poloidal flux due to the current density shown in Figure 4.3a.

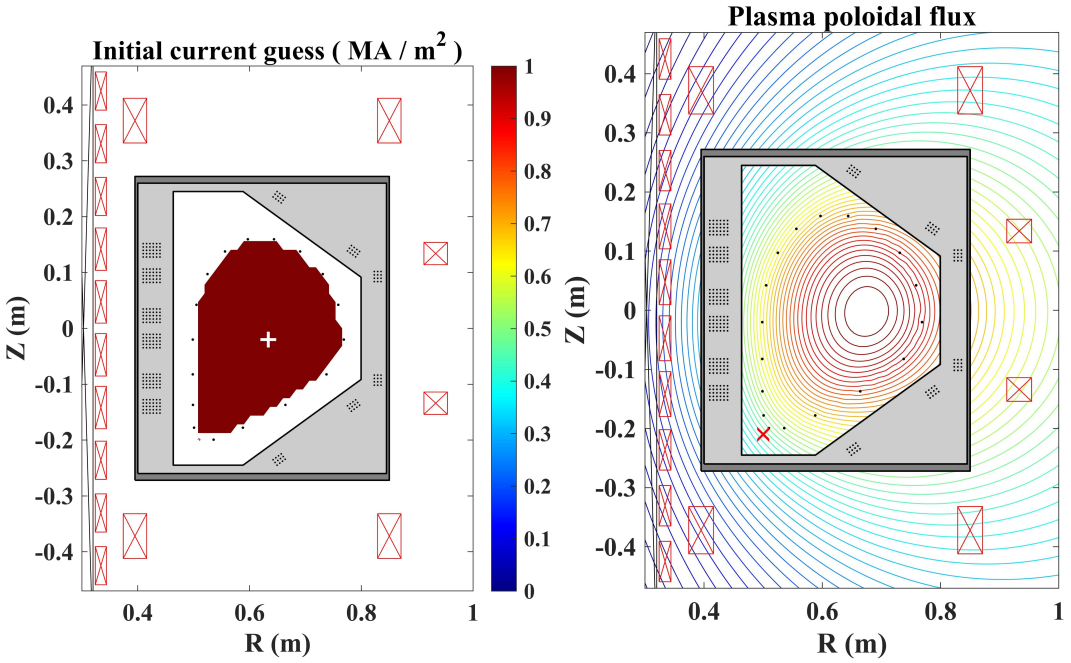

(a) (b)

Figure 4.3: (a) Example of an initial guess of plasma current density. (b) Poloidal flux distribution produced by the plasma current density shown in (a) and the prescribed boundary points (blue dots) and X-point (red cross).

Note that the calculated $\Psi_p(R,Z)$ shown in Figure 4.3b is not an iso-flux at the prescribed boundary points. Therefore, additional poloidal fluxes are required to adjust that and also to have $\mathbf{B_{pol}} = 0$ at the X-point. This is obtained by turning on and adjusting the PF coil currents.

4.3.3 The optimisation method for obtaining the PF coil currents

The 16 independently powered PF coils that will operate in the TCABR will provide a great plasma shaping flexibility. These coils are also known as "shaping coils" as they are responsible to deform the flux surfaces in order to obtain a particular plasma shape. One might end up finding an infinite set of possible solutions for the PF coil currents that gives the desired plasma shape. However, we are interested in the solution that provides the minimum set of PF coil current amplitudes. For that, it is necessary to derive an optimisation process to minimise a cost function made of the following terms:

- Power dissipation in the PF coils: it minimises the currents in each coil:

$$P_R = \sum_a R_a I_a^2, \tag{4.3}$$

- Dipoles at the PF coils: it minimises the difference in current amplitude between neighbour PF coils:

$$D = \sum_{a,a'} I_a D_{aa'} I_{a'}, \tag{4.4}$$

- Flux error on approximate boundary points (R_k, Z_k):

$$\epsilon_\Psi = \sum_k \left[\left(M_{k,a} \cdot I_a + \Psi_{kp} + M_{k,oh} \cdot I_{oh} + M_{k,v} \cdot I_v \right) - \Psi_b \right]^2, \tag{4.5}$$

The final cost function, with pre-selected weights, is given by

$$\chi^2 = W_R \sum_a R_a I_a^2 + W_D \sum_{a,a'} I_a D_{aa'} I_{a'} + W_\Psi \sum_k (\Psi_k - \Psi_b)^2 \tag{4.6}$$

with $\Psi_k = M_{k,a} \cdot I_a + \Psi_{kp} + M_{k,oh} \cdot I_{oh} + M_{k,v} \cdot I_v$. One can notice that it is possible to write the above equation in a matrix form such as

$$\chi^2 = \mathbf{x}^t \cdot \mathbf{P} \cdot \mathbf{x} + (\mathbf{A} \cdot \mathbf{x} + \mathbf{b})^t \cdot \mathbf{W} \cdot (\mathbf{A} \cdot \mathbf{x} + \mathbf{b}). \tag{4.7}$$

where $\mathbf{x} = [\mathbf{I_a} \;\; \Psi_b]^t$ is a vector containing the PF coil currents and the value of the poloidal flux at the plasma boundary, $\mathbf{P}$ is a matrix that gathers Equations 4.3 and 4.4 and has the last column equals to zero. The matrix $\mathbf{A}$ relates the first and last terms of Equation 4.5 while the vector $\mathbf{b}$ relates the other terms. Until this point, we have not imposed any of the constraints mentioned in the previous section. We can cast these constraints as follows:

$$\mathbf{C} \cdot \mathbf{x} = \mathbf{d}, \tag{4.8}$$

where $\mathbf{C}$ are the Green's functions of the PF coils at the prescribed constraint points and $\mathbf{d}$ is the vector containing the values of the calculated poloidal flux of the plasma, Ohmic system and vacuum vessel, all at the prescribed constraint points.

We now define the Lagrange function

$$\mathscr{L}(\mathbf{x},\lambda) = \mathbf{x}^t \cdot \mathbf{P} \cdot \mathbf{x} + (\mathbf{A}\cdot\mathbf{x}+\mathbf{b})^t \cdot \mathbf{W} \cdot (\mathbf{A}\cdot\mathbf{x}+\mathbf{b}) - (\mathbf{C}\cdot\mathbf{x}-\mathbf{d})^t\ \lambda, \tag{4.9}$$

where λ are the Lagrange multipliers, as explained in Section 3.2. The solution of the minimisation is obtained by finding the values of $\mathbf{x}$ and λ that satisfies

$$\frac{\partial \mathscr{L}}{\partial \mathbf{x}} = 0, \quad \frac{\partial \mathscr{L}}{\partial \lambda} = 0. \tag{4.10}$$

The first equation yields

$$\left(\mathbf{P} + \mathbf{A}^t \cdot \mathbf{W} \cdot \mathbf{A}\right)\mathbf{x} - \frac{\mathbf{C}^t}{2}\lambda = -\mathbf{A}^t \cdot \mathbf{W} \cdot \mathbf{b}, \tag{4.11}$$

while the second one yields the constraint equation (Equation 4.8). Then, Equation 4.10 can be written in matrix form as

$$\begin{bmatrix} \mathbf{P} + \mathbf{A}^t \cdot \mathbf{W} \cdot \mathbf{A} & -\mathbf{C}^t/2 \\ \mathbf{C} & \mathbf{0} \end{bmatrix} \cdot \begin{bmatrix} \mathbf{x} \\ \lambda \end{bmatrix} = \begin{bmatrix} -\mathbf{A}^t \cdot \mathbf{W} \cdot \mathbf{b} \\ \mathbf{d} \end{bmatrix}. \tag{4.12}$$

Therefore, the solution for the PF coil currents, contained in the $\mathbf{x}$ vector, is obtained by

$$\begin{bmatrix} \mathbf{x} \\ \lambda \end{bmatrix} = \begin{bmatrix} \mathbf{P} + \mathbf{A}^t \cdot \mathbf{W} \cdot \mathbf{A} & -\mathbf{C}^t/2 \\ \mathbf{C} & \mathbf{0} \end{bmatrix}^{-1} \cdot \begin{bmatrix} -\mathbf{A}^t \cdot \mathbf{W} \cdot \mathbf{b} \\ \mathbf{d} \end{bmatrix}. \tag{4.13}$$

Figure 4.4 shows the third step of the Picard algorithm after the calculation of the poloidal magnetic flux due to the initial current guess shown in Figure 4.3.

The imposed constraint here is to have a null-point at the red cross shown. The first panel of Figure 4.4 shows the boundary points and the constraint for the poloidal magnetic field. The second and third panels shows the currents in each PF coils and the produced poloidal magnetic flux, respectively. Finally, the last panel shows the total poloidal magnetic flux.

4.3.4 Parameterisation of the kinetic profiles

Until now, we have not considered the effect of the Picard iterations on the kinetic profiles that are used to construct the p' term in the Grad-Shafranov equation. This is done in the 7^{th} step of the Picard algorithm described in Section 4.3, where we need to update the plasma current density given by

$$J_\phi(R,Z) = 2\pi\left(R\,p' + \frac{FF'}{\mu_0\,R}\right). \tag{4.14}$$

In the following, a description on how parameterise each of the kinetic profiles is given.

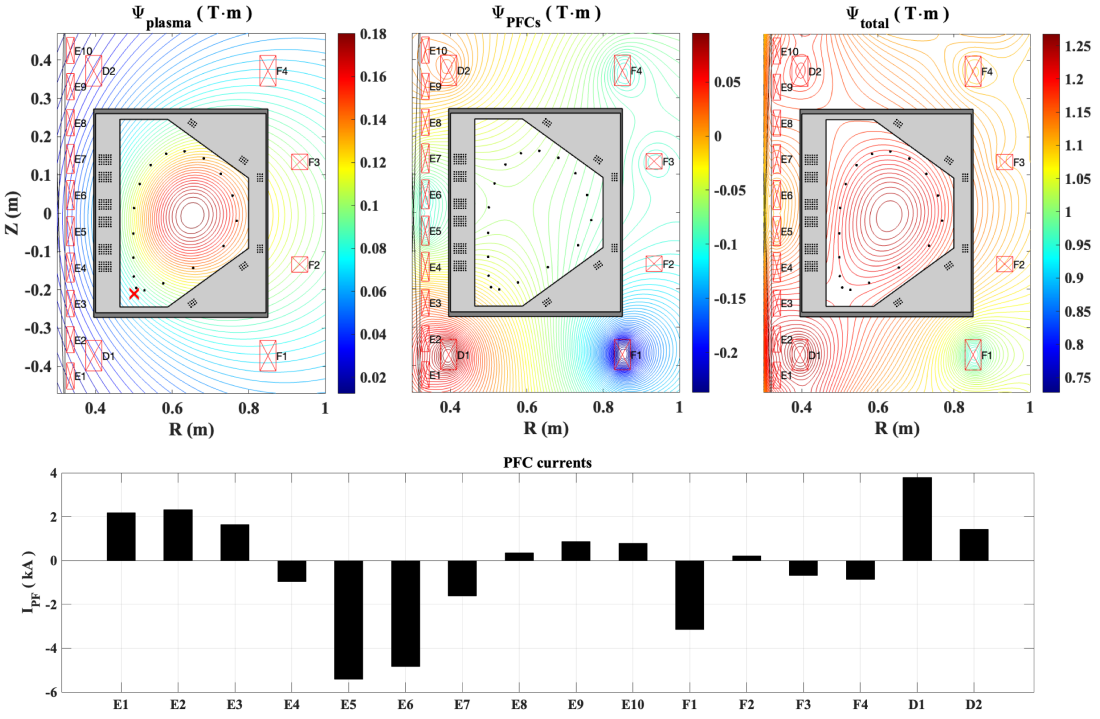

Figure 4.4: Poloidal fluxes: (left) due to the plasma, (centre) due to the PF coil currents and (right) total. Electric current estimated in each coil to have the shape as in the right-top panel

Total plasma pressure

Tokamaks can be operated in basically two types of confinement mode: the low confinement mode (L-mode), which is characterised by relatively high levels of turbulence, and the high confinement mode (H-mode), which is characterised by relatively low levels of the turbulence that, in turn, causes an increase in energy confinement time typically by a factor of 2 [21]. The main feature of H-mode plasmas is the presence of a pedestal in the electron temperature, density and, consequently, pressure profiles at the plasma edge. These profiles can be modelled as [21]:

$$f(\Psi_N) = f_{\text{sep}} + a_0 \left\{ \tanh\left[\frac{2(1-\Psi_{\text{mid}})}{\Delta}\right] - \tanh\left[\frac{2(\Psi_N-\Psi_{\text{mid}})}{\Delta}\right] \right\} + a_1 \left[1 - \left(\frac{\Psi_N}{\Psi_{\text{ped}}}\right)^{\alpha_1}\right]^{\alpha_2}. \quad (4.15)$$

Here, f represents either density or temperature as a function of normalised flux Ψ_N, f_{sep} is the value of f at the LCFS, Δ is the pedestal width, Ψ_{mid} is the location of the centre of the pedestal, and Ψ_{ped} is the location of the pedestal top.

The second term on the RHS controls the pedestal region while the last term controls the profile shape in the core region. The pressure profile for each species can be calculate via:

$$p_\alpha = 16.02\, n_{\alpha,20}\, T_{\alpha,keV} \quad \text{(kPa)}, \quad (4.16)$$

where p_α is given in kPa if $T_{\alpha,\text{keV}}$ is given in keV and $n_{\alpha,20}$ given in units of 10^{20} m^{-3}.

Therefore, the total pressure is the sum of the pressures of all species. For the TCABR:

$$p_{\text{tot}} = p_{\text{e}} + p_{\text{i}} + p_{\text{C}} + p_{\text{Fe}}, \tag{4.17}$$

where p_{e} is the electron pressure, p_{i} is the ion pressure, p_{C} is the carbon impurity pressure, and p_{Fe} is the iron impurity pressure. Depending on the choices of the free parameters a_0, a_1, α_1, and α_2 in Equation 4.15, we can model profiles that represents plasma in the low or in the high confinement mode. Figure 4.5 shows the pressure, temperature, and density profiles as function of normalised poloidal flux. One can notice the increase of the quantities at the plasma core and the presence of the pedestal structure in all the H-mode profiles.

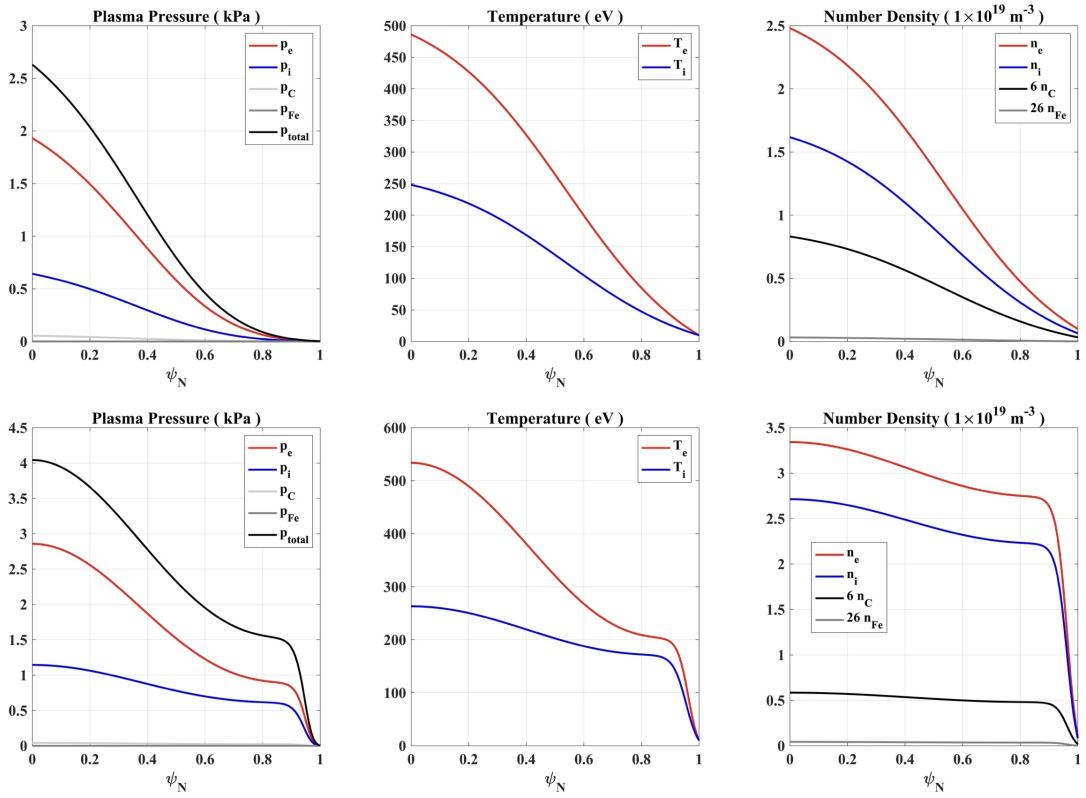

Figure 4.5: Examples of L-mode (first row) and H-mode (second row) pressure, temperature and density radial profiles, for different species, obtained from Equations 4.15, 4.16 and 4.17.

Poloidal current function

The internal profile related with the poloidal current, FF', is supposed to be a linear combination of a set of basis functions of the normalised poloidal flux

$$FF'(\Psi_N) = \sum_{k=0}^{N_p-1} \alpha_k g_k(\Psi_N), \tag{4.18}$$

where α_k are free parameters obtained by the N_p imposed physical constraints. Let us manipulate Equation 4.18 in order to obtain the poloidal current function F:

$$FF'(\Psi_N) = F\frac{dF}{d\Psi}(\Psi_N) = \frac{1}{2}\frac{dF^2}{d\Psi}, \tag{4.19}$$

but, from the definition of normalised poloidal flux, given by Equation 3.17, we have that

$$\frac{d}{d\Psi} = \frac{d\Psi_N}{d\Psi}\frac{d}{d\Psi_N} = \frac{1}{\Delta\Psi}\frac{d}{d\Psi_N},$$

where $\Delta\Psi = \Psi_{\text{LCFS}} - \Psi_{\text{axis}}$. Therefore,

$$FF'(\Psi_N) = \frac{1}{2\Delta\Psi}\frac{dF^2}{d\Psi_N} \implies \frac{dF^2}{d\Psi_N} = 2\Delta\Psi\sum_{k=0}^{N_p-1}\alpha_k g_k(\Psi_N). \tag{4.20}$$

Integrating the above equation from $\Psi'_N = 1$ to $\Psi'_N = \Psi_N$

$$\int_1^{\Psi_N}\frac{dF^2}{d\Psi'_N}d\Psi'_N = 2\Delta\Psi\sum_{k=0}^{N_p-1}\alpha_k\int_1^{\Psi_N} g_k(\Psi_N)\,d\Psi'_N \implies$$

$$\implies F(\Psi_N) = \sqrt{F_1^2 + 2\Delta\Psi\sum_{k=0}^{N_p-1}\alpha_k\int_1^{\Psi_N} g_k(\Psi_N)\,d\Psi'_N}, \tag{4.21}$$

where $F_1 = R_0 B_0$, with R_0 being the major radius of the tokamak and B_0 the amplitude of the vacuum toroidal field at R_0. Per definition, the poloidal current function $F = R B_\phi$ depends on the toroidal magnetic field. Therefore, if there is no plasma, the toroidal magnetic field is the one produced by the toroidal field coils ($B_\phi = R_0 B_0/R$) and, therefore, F will be constant inside the vacuum vessel, as

$$F = R B_\phi(R) = R\frac{R_0 B_0}{R} = R_0 B_0.$$

Note that the poloidal current function determines if the plasma will have a diamagnetic or a paramagnetic behaviour.

5 Simulations of plasma scenarios in TCABR

In this chapter, we show the results for the design of some of the plasma scenarios envisaged for TCABR, Figure 5.1. The parameters that define the equilibrium are also presented here.

5.1 Magnetic configuration for plasma breakdown

The poloidal magnetic field configuration plays an important role during the plasma start-up phase. In regions with smaller poloidal magnetic field, the connection length is longer and, as shown in Equation 2.7, breakdown occurs more easily in these regions. The flexibility provided by the 16 independent powered PF coils of TCABR allows for the creation of a poloidal field null-point with different properties at various locations within the vacuum vessel. Since plasma elongation, triangularity and squareness is usually negligible during the early ramp-up phase, we start with a small circular plasma ($a \approx 5$ cm) centred at $(R_{\rm br}, Z_{\rm br})$. The technique used to impose the magnetic configuration during the breakdown phase is the one described in Section 4.3.3, with the slight change that we need to set $\mathbf{A} = \mathbf{0}$ and $\mathbf{b} = \mathbf{0}$ since at this time there is no plasma yet. For the breakdown configuration then, Equation 4.13 becomes

$$\begin{bmatrix} \mathbf{x} \\ \lambda \end{bmatrix} = \begin{bmatrix} \mathbf{P} & -\mathbf{C}^t/2 \\ \mathbf{C} & \mathbf{0} \end{bmatrix}^{-1} \cdot \begin{bmatrix} \mathbf{0} \\ \mathbf{d} \end{bmatrix}, \tag{5.1}$$

where $\mathbf{x}$ is a vector containing the PF coil currents, $\mathbf{P}$ is a diagonal matrix containing the electric resistances of each PF coil, $\mathbf{C}$ contains the imposed constraints on the magnetic field and $\mathbf{d}$ is a vector containing the values of the calculated poloidal flux due to the Ohmic current at the prescribed constraint point. The breakdown magnetic configuration is obtained by imposing a second order null-point at $(R_{\rm br}, Z_{\rm br})$, i.e. by imposing the following constraints for the poloidal magnetic field

$$\left(B_R = B_Z = \frac{\partial B_R}{\partial R} = \frac{\partial B_R}{\partial Z} \right) \Bigg|_{(R_{\rm br}, Z_{\rm br})} = 0. \tag{5.2}$$

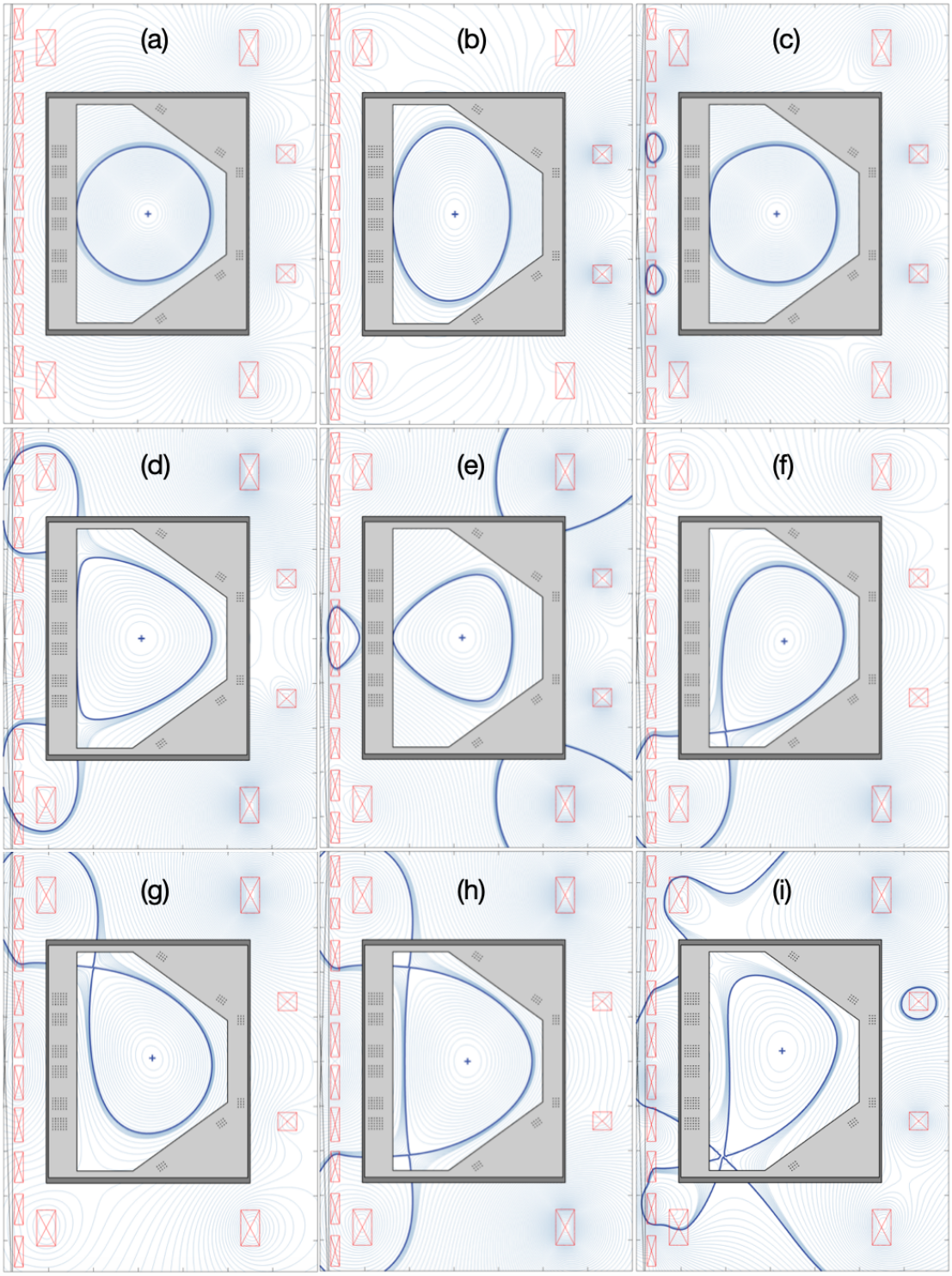

Figure 5.1: Plasma shapes envisaged for TCABR. Limited configurations: (a) circular, (b) elongated, (c) with squareness, (d) positive triangularity and (e) negative triangularity. Diverted configurations: (f) lower single-null, (g) upper single-null, (h) double-null, and (i) snowflake.

The results for the breakdown, which can be seen in Figure 5.2, will be used in the beginning of all plasma scenarios, since all of them start as a small limited circular plasma.

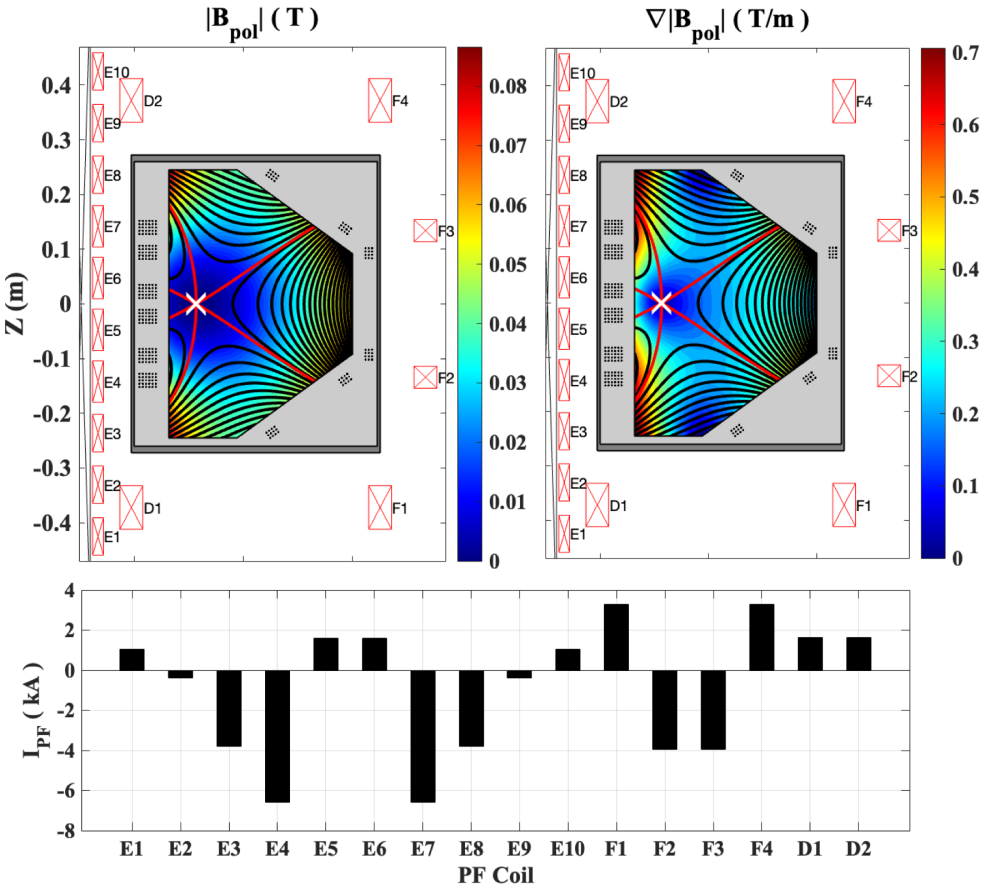

Figure 5.2: Magnetic configuration used for inducing breakdown at $(R_{\mathrm{br}}, Z_{\mathrm{br}})$ = (0.51 , 0) m and I_{OH} = 24 kA with a second order null-point at that location.

5.2 The kinetic profiles

This section describes how the kinetic profiles described in Section 4.3.4 are calculated based on three imposed constraints: one for the plasma pressure and two for the poloidal current function.

5.2.1 Total plasma pressure

An important macroscopic plasma quantity used as a figure of merit for a tokamak plasma performance is the normalised plasma pressure,

$$\beta = \frac{\langle p \rangle}{\langle B^2 \rangle / 2\mu_0}, \tag{5.3}$$

where $\langle p \rangle = \frac{1}{V}\int_V p\, dV$ is the volume averaged plasma pressure and $\langle B^2 \rangle = \langle B_\theta^2 \rangle + B_0^2$. The parameter β measures the ratio between the kinetic and magnetic energy. Another normalisation of the plasma pressure used to express the proximity to a plasma stability limit is [9]

$$\beta_N = \frac{\beta[\%]\, a[\mathrm{m}]\, B_0[\mathrm{T}]}{I_p[\mathrm{MA}]}, \tag{5.4}$$

By prescribing β_N, we can re-scale the pressure profile, given by Equation 4.16 and shown in the first panel of Figure 4.5. Denoting this given pressure profile as $\tilde{p}$, the scaled one becomes $p = f_p\, \tilde{p}$, and we calculate f_p by using Equations 5.3 and 5.4.

$$\frac{\langle p \rangle}{\langle B^2 \rangle / 2\mu_0} = \frac{I_p[\mathrm{MA}]\, \beta_N}{a[\mathrm{m}]\, B_0[\mathrm{T}]} \implies \langle p \rangle = \langle f_p\, \tilde{p} \rangle = \frac{I_p[\mathrm{MA}]\, \beta_N\, \langle B^2 \rangle / 2\mu_0}{a[\mathrm{m}]\, B_0[\mathrm{T}]} \implies$$

$$\implies f_p = \frac{I_p[\mathrm{MA}]\, \langle B^2 \rangle\, \beta_N}{2\mu_0\, a[\mathrm{m}]\, B_0[\mathrm{T}]\, \langle \tilde{p} \rangle}. \tag{5.5}$$

Therefore, since the kinetic profiles are prescribed in the second iteration of Picard algorithm, the averaged values in the RHS of Equation 5.5 can be calculated from the previous step, while the other terms are initially prescribed.

5.2.2 Poloidal current function

We defined the internal kinetic profile, FF', as a linear combination of a set of basis functions of the normalised poloidal flux. For this present work, we impose two physical constraints: one on the plasma current I_p and the other on the averaged toroidal plasma current, given by Equation 2.37. Here, we assume that FF' is a linear function of Ψ_N and, therefore, Equation 4.18 is truncated at $N_p = 2$,

$$FF'(\Psi_N) = \alpha_0 + \alpha_1\, \Psi_N. \tag{5.6}$$

The goal now is to obtain both coefficients, α_0 and α_1, using the imposed constraints.

The first constraint comes from the definition of the plasma current density, Equation 4.14. If we integrate this equation in the poloidal plane, we obtain

$$\iint \frac{FF'}{R} dR\, dZ = \mu_0 \left(\frac{I_p}{2\pi} - \iint R\, p'\, dR\, dZ \right) \implies$$

$$\implies \alpha_0 \iint \frac{1}{R} dR\, dZ + \alpha_1 \iint \frac{\Psi_N}{R} dR\, dZ = \mu_0 \left(\frac{I_p}{2\pi} - \iint R\, p'\, dR\, dZ \right). \tag{5.7}$$

The second one comes from imposing $J_{\text{tor}}(\Psi_N = 1) = 0$,

$$0 = R_0\, p'\Big|_{\Psi_N=1} + \frac{FF'}{\mu_0 R_0}\left\langle \frac{R_0^2}{R^2}\right\rangle\Big|_{\Psi_N=1} \implies FF'\Big|_{\Psi_N=1} = -\frac{\mu_0 R_0^2 p'}{\left\langle R_0^2/R^2\right\rangle}\Big|_{\Psi_N=1},$$

which means that the plasma current is restricted inside of the last close flux surface. Therefore, we obtain the second equation for the coefficients

$$\alpha_0 + \alpha_1 = -\frac{\mu_0}{\Delta\Psi}\left(\frac{1}{\langle R^{-2}\rangle}\frac{dp}{d\Psi_N}\right)\Big|_{\Psi_N=1}. \tag{5.8}$$

Solving these linear system of equations yields the coefficients of Equation 5.6, and we can easily integrate it to obtain

$$F(\Psi_N) = \sqrt{F_1^2 + 2\Delta\Psi\,(\Psi_N - 1)\left[\alpha_0 + \frac{\alpha_1}{2}\,(\Psi_N + 1)\right]} \tag{5.9}$$

5.2.3 Effect of the kinetic profiles on the PF coil currents and diamagnetism

By simulating five different single-null diverted plasma with $I_p = 105\,\text{kA}$, $\beta_N[\%] = 0.35$ and with five different pressure profiles (shown in panel (a) of Figures 5.3, 5.4, 5.5, 5.6 and 5.7), two important results are obtained regarding the impact of the kinetic profiles on the PF coil currents and on the magnetic response of the plasma to the externally applied toroidal field.

The first result shows that changes in the pressure profile, while keeping β_N constant, does not cause significant changes in the PF coil currents, pictured on panel (b) of the figures below. For the L-mode profiles, the maximum difference are of the order of just $\Delta I_a \approx 80\,\text{A}$. However, for the H-mode profile, the maximum difference can be as high as $\Delta I_a \approx 2.0\,\text{kA}$ compared with those in the the L-mode profiles. The second result comes from the monotonic poloidal current function profiles, panels (d) on the figures below. We notice that $F(0) < F(1)$, which is expected because with our prescribed β_N and toroidal magnetic field, it yields a $\beta_{\text{pol}} = 2\mu_0\langle p\rangle/\langle B_\theta^2\rangle$ smaller than unit, i.e. the gyro-orbits of the charged particles being such as to reduce the toroidal magnetic field inside the plasma. Panel (e) on Figures 5.3, 5.4, 5.5, 5.6, and 5.7 show this diamagnetic effect. For the cases of $\beta_{\text{pol}} > 1$, the plasma would react such that to increase the toroidal magnetic field inside it, and therefore, it would be paramagnetic.

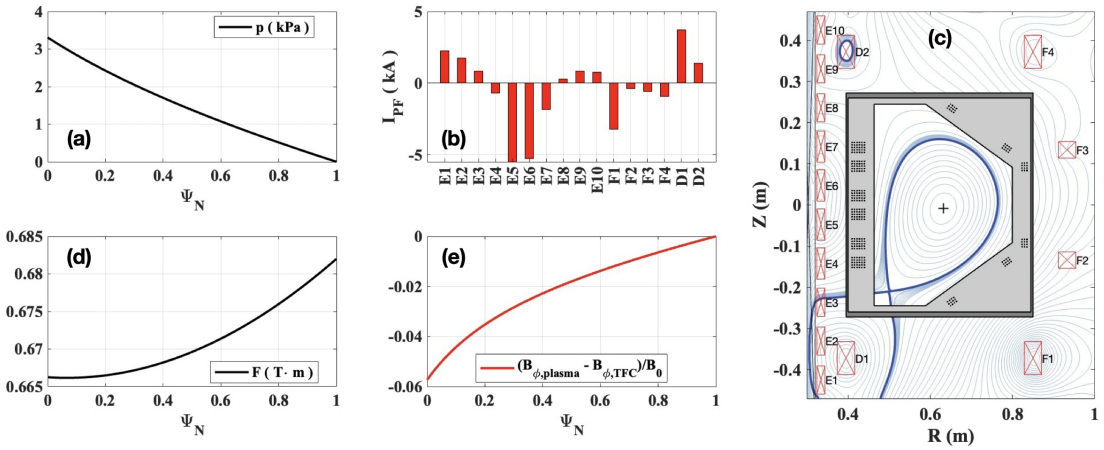

Figure 5.3: Static simulation for a prescribed pressure profile given by $p(\Psi_N) = p_0\left(\frac{1}{1+\Psi_N} - \frac{\Psi_N}{2}\right)$.

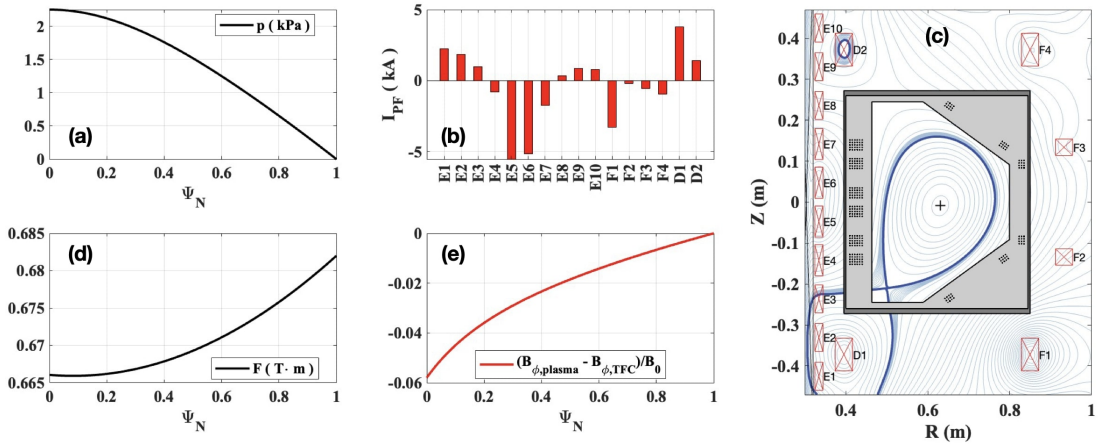

Figure 5.4: Static simulation for a prescribed pressure profile given by $p(\Psi_N) = p_0\left(\frac{1}{1+\Psi_N^2} - \frac{\Psi_N^2}{2}\right)$.

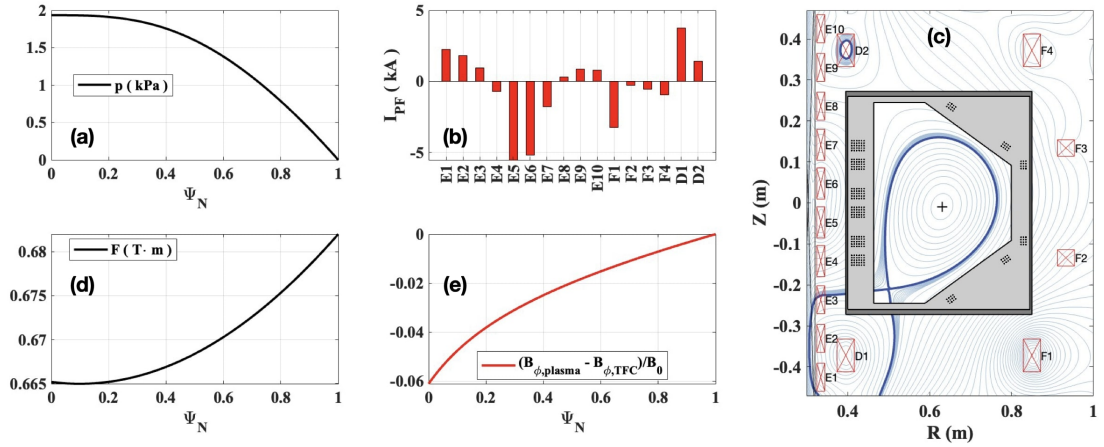

Figure 5.5: Static simulation for a prescribed pressure profile given by $p(\Psi_N) = p_0\left(\frac{1}{1+\Psi_N^3} - \frac{\Psi_N^3}{2}\right)$.

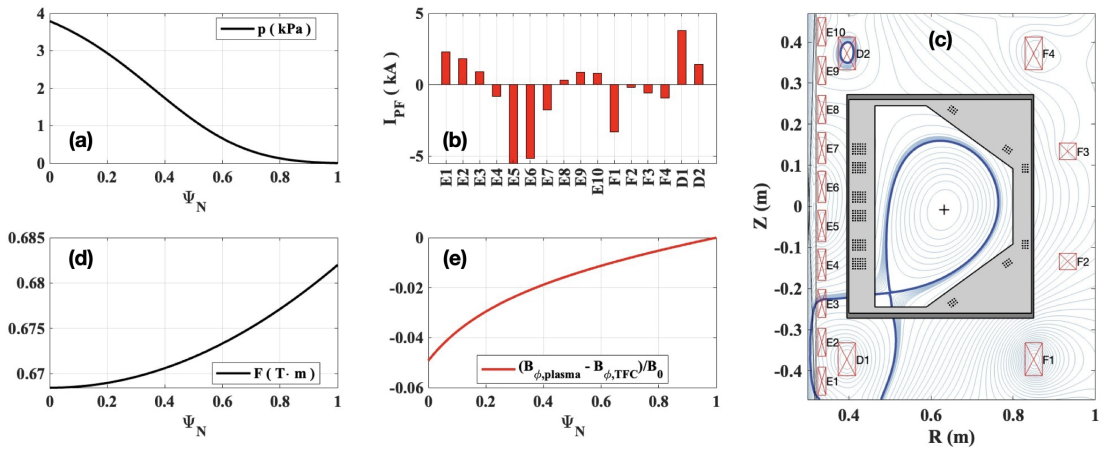

Figure 5.6: Static simulation for a characteristic L-mode pressure profile.

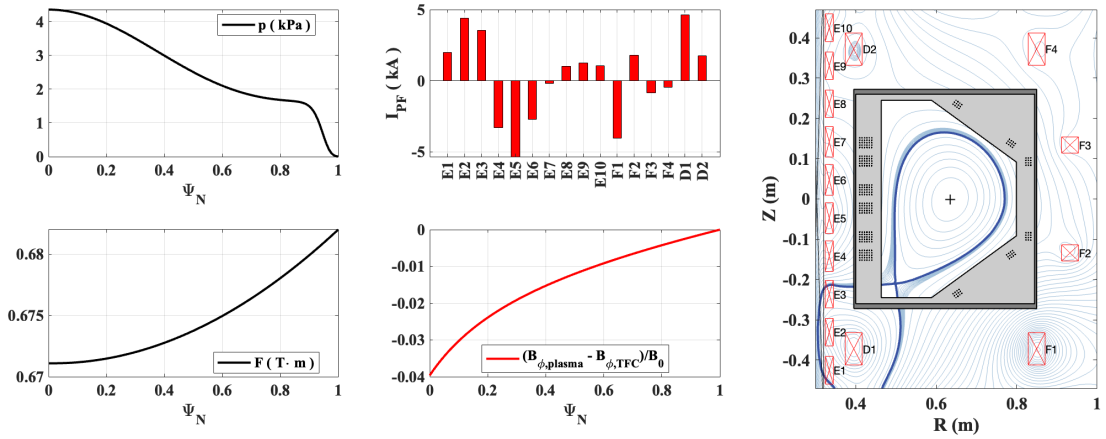

Figure 5.7: Static simulation for a characteristic H-mode pressure profile.

5.3 Time evolution of plasma scenarios

In this Section, the simulation of nine TCABR plasma scenarios is presented. In these scenarios, the plasma current is ramped-up to achieve its prescribed flat-top value and then ramped-down until the plasma is terminated. The entire discharge is expected to last around 1200 ms: 100 ms of current ramp-up, 1000 ms of current flat-top phase and 100 ms of current ramp-down. These three phases can be seen in Figure 5.8. Each point in the operational space of the simulated experiment is assumed to be in an MHD equilibrium, i.e. the plasma shape and currents in the system evolves from one Grad-Shafranov solution to another. Therefore, the three phases just mentioned will be divided into 10 equilibria each, totalling 30 points for the entire discharge simulation., but these are arbitrary numbers, one can change the number of points in the operational space.

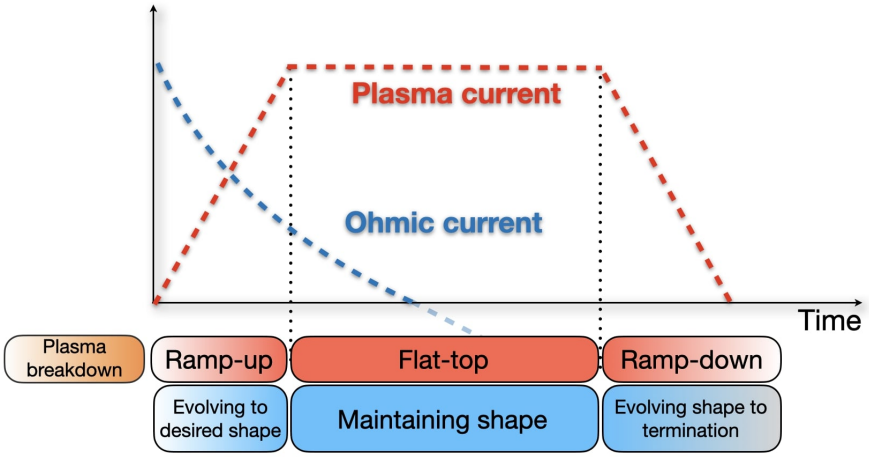

Figure 5.8: Schematic of a typical tokamak discharge. The magnetic configuration of breakdown is expected to occur at $t_0 = 0$ s where the Ohmic coil is charged with a current $I_{\mathrm{OH}}(t_0) \neq 0$.

To have induced vacuum vessel currents included self-consistently in the calculations, we linearise all the electrical parameters in Equation 3.27 that are related to the plasma, such as plasma resistance, self-inductance and mutual inductances of the plasma with any other part of the system. For example, let $f(t)$ be any of these electrical parameters, then

$$f^{(n)}(t) = f^{(n-1)} + \frac{df^{(n)}}{dt}\left(t^{(n)} - t_{\mathrm{eq}}^{(n)} + \Delta t^{(n)}\right), \tag{5.10}$$

where $t_{\mathrm{eq}}^{(n)}$ is the time of the n-th equilibrium, $t^{(n)} \in \left[t_{\mathrm{eq}}^{(n)} - \Delta t^{(n)},\ \Delta t^{(n)}\right]$ is the linearisation time, $\Delta t^{(n)} = t_{\mathrm{eq}}^{(n)} - t_{\mathrm{eq}}^{(n-1)}$ is the time step, and $\frac{df^{(n)}}{dt} = \frac{(f^{(n)} - f^{(n-1)})}{dt^{(n)}}$. The parameter β_N, Equation 5.4, is set to $\beta_N[\%] = 0.35$, a factor of around 10 smaller than the Troyon limit [9]. Therefore, the scaling factor f_p will change for each MHD equilibrium during the discharge as I_p, a and $\langle B^2 \rangle$ changes from equilibrium to equilibrium. The plasma current at the flat-top is chosen to be $I_p \leq 120$ kA to avoid $q_{\mathrm{edge}} \leq 2$ kink instabilities.

5.3.1 Limited plasmas

Here, the simulation of five wall-limited plasma scenarios is presented. The simulation include the time evolution of each coil current and voltage needed to create the desired plasma shape evolution. Limited plasmas are characterised by having having the LCFS defined by the intersection of the plasma with a physical material wall. In these simulations, the plasma starts at the breakdown position with a current of $I_p = 10$ kA and with the Ohmic coil charged with $I_{\mathrm{OH}} = 24$ kA.

Circular plasma

The circular plasma is modeled to achieve a plasma current at the flat-top with $I_p = 90\,\text{kA}$ and with maximum minor radius of $a = 15\,\text{cm}$. The plasma current is ramped-up until it reaches the flat-top value along with its final circular shape. The simulation of this limited plasma is shown in Figures 5.9. The first row of this figure shows the prescribed plasma current, followed by the calculated evolution of the Ohmic current pictured on the second row and the evolution of the plasma shape on the last row. We notice that to induce the prescribed plasma current, the Ohmic system will have to operate with currents of $I_{\text{OH}} = \pm 24\,\text{kAcc}$ and voltages varying from $V_{\text{OH}} \approx 0.8\,\text{kV}$ to $V_{\text{OH}} \approx -1.2\,\text{kV}$, as shown in Figure 5.10. To obtain the evolution of the circular shape, the PF coil power supplies will have to provide currents and voltages of up to $|I_a| = 2.0\,\text{kAcc}$, and $|V_a| = 200\,\text{V}$, respectively. These results are presented in Figure 5.11.

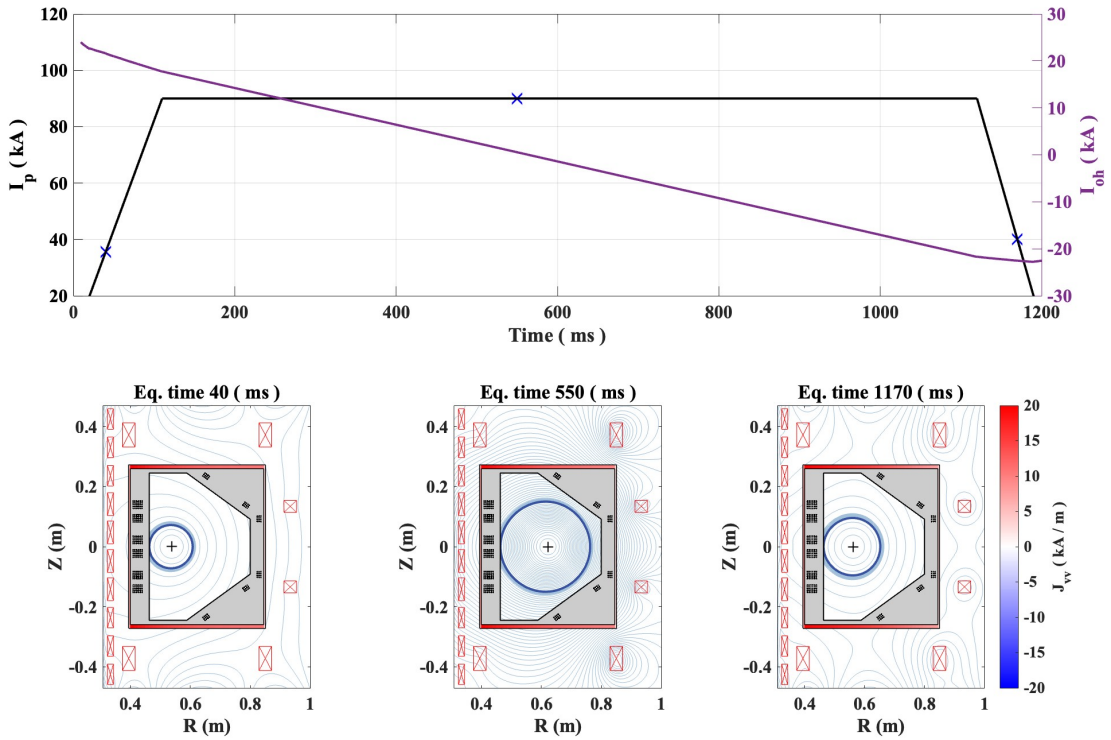

Figure 5.9: Time evolution of a circular plasma at three points in time.

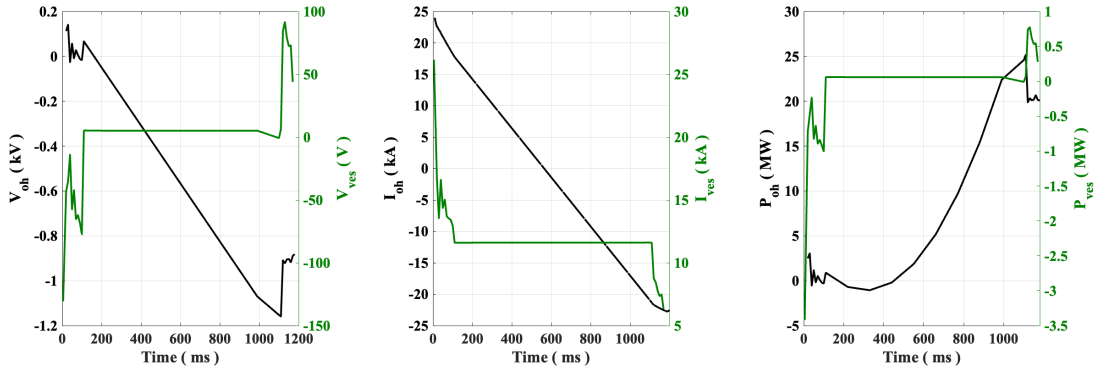

Figure 5.10: Time evolution of the voltage, current, and power on the Ohmic and vacuum vessel (induced) for a circular plasma.

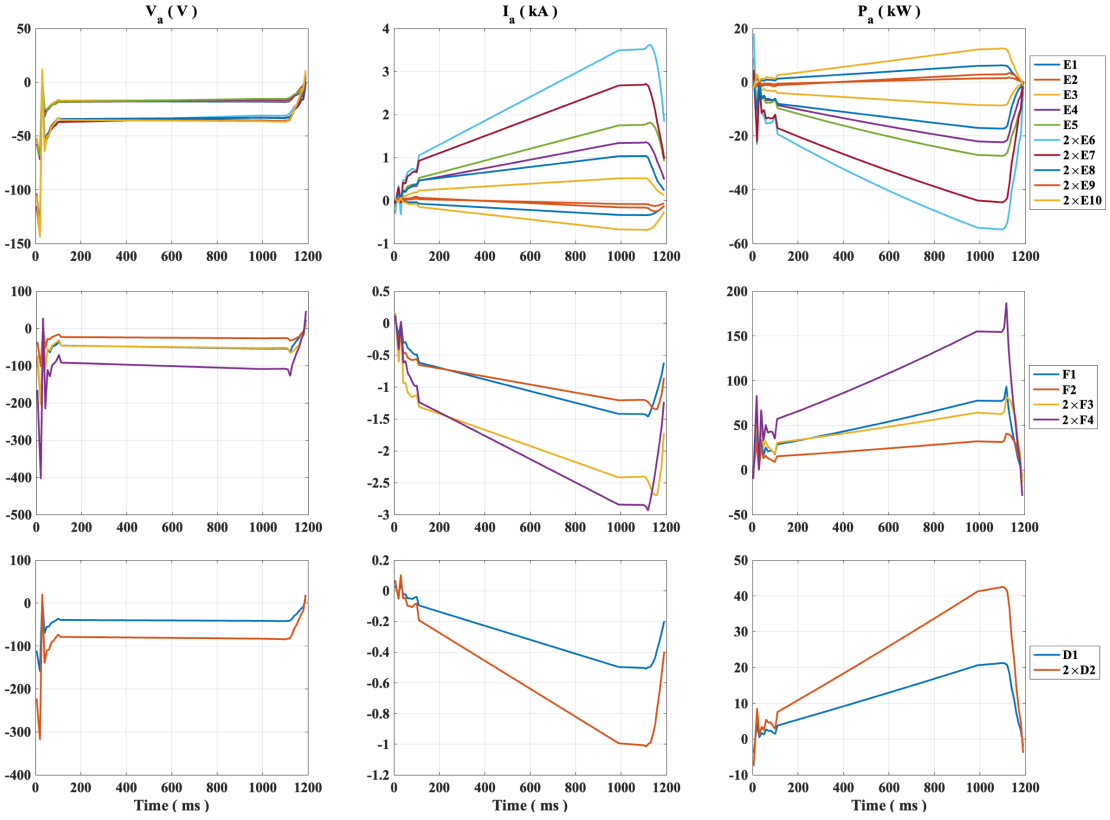

Figure 5.11: Time evolution of the voltage, current, and power on each PF coil for a circular plasma.

Elongated plasma

The elongated plasma is modeled to achieve a plasma current at the flat-top with $I_p = 100\,\text{kA}$ and with maximum elongation of $\kappa = 1.5$. The current is ramped-up until it reaches this flat-top value along with its final elongated shape. The simulation of this limited plasma is shown in Figure 5.12. The first row of this figure shows the prescribed plasma current, followed by the calculated evolution of the Ohmic current pictured on the second row and the evolution of the plasma shape on the last row. We notice that, to induce the prescribed plasma current, the Ohmic system have to operate with currents of $I_{\text{OH}} = \pm 24\,\text{kA}$ and voltages varying from $V_{\text{OH}} \approx 0.5\,\text{kV}$ to $V_{\text{OH}} \approx -1.2\,\text{kV}$, as shown in Figure 5.13. To obtain the evolution of the elongated shape, the PF coil currents will have to provide currents and voltages up to $|I_a| = 4.0\,\text{kA}$, and $|V_a| = 200\,\text{kV}$, respectively. These results are presented in Figure 5.14.

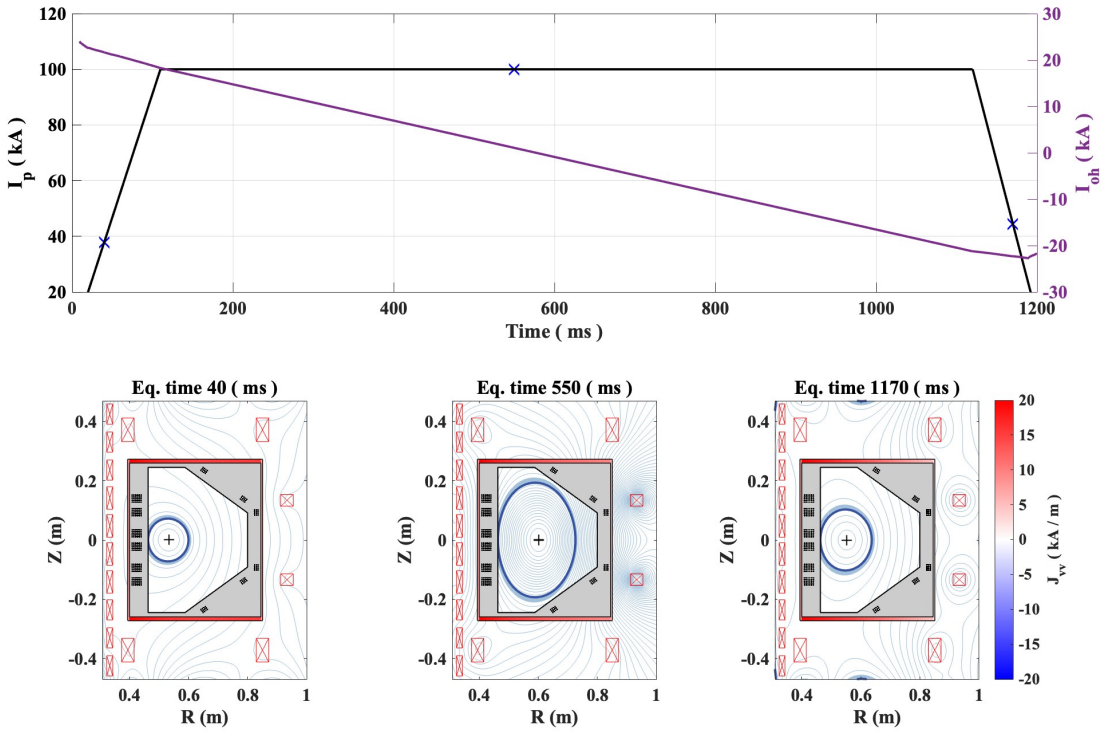

Figure 5.12: Time evolution of an elongated plasma at three points in time.

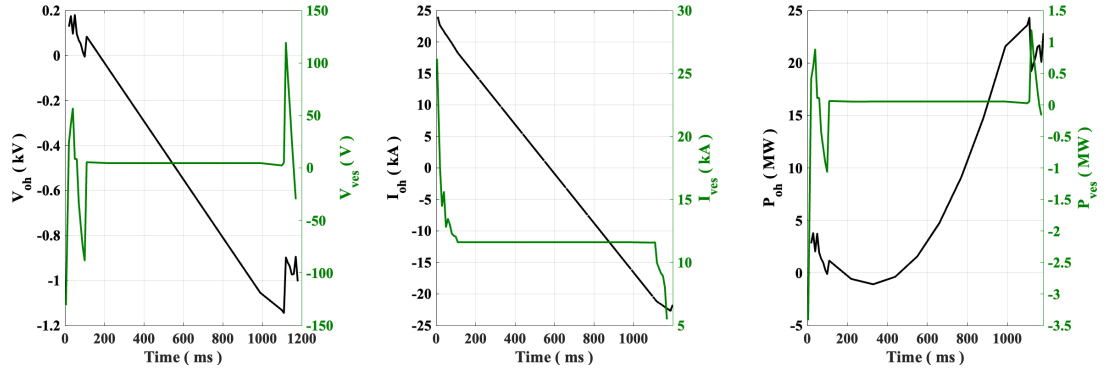

Figure 5.13: Time evolution of the voltage, current, and power on the Ohmic and vacuum vessel (induced) for an elongated plasma.

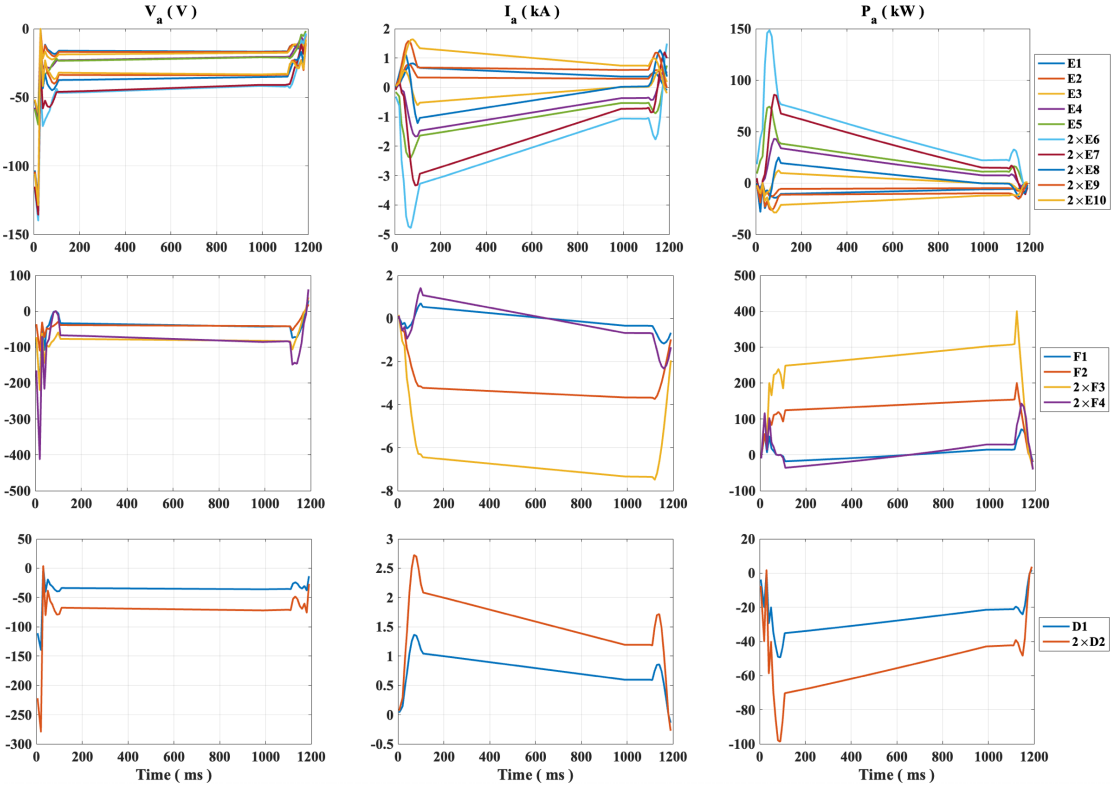

Figure 5.14: Time evolution of the voltage, current, and power on each PF coil for an elongated plasma.

Positive triangularity plasma

The plasma with positive triangularity is modeled to achieve a plasma current at the flat-top with $I_p = 100\,\text{kA}$ and with elongation of $\kappa = 1.4$ and with triangularity of $\delta = 1.5$. The current is ramped-up until it reaches this flat-top value along with its final triangular shape. The simulation of this limited plasma is shown in Figure 5.15. The first row of this figure shows the prescribed plasma current, followed by the calculated evolution of the Ohmic current pictured on the second row and the evolution of the plasma shape on the last row. We notice that, to induce the prescribed plasma current, the Ohmic system have to operate with currents of $I_{\text{OH}} = \pm 24\,\text{kA}$ and voltages varying from $V_{\text{OH}} \approx 0.3\,\text{kV}$ to $V_{\text{OH}} \approx -2.3\,\text{kV}$, as shown in Figure 5.16. To obtain the evolution of the shape, the PF coil currents will have to provide currents and voltages up to $|I_a| = 7.0\,\text{kA}$, and $|V_a| = 300\,\text{V}$, respectively. These results are presented in Figure 5.17.

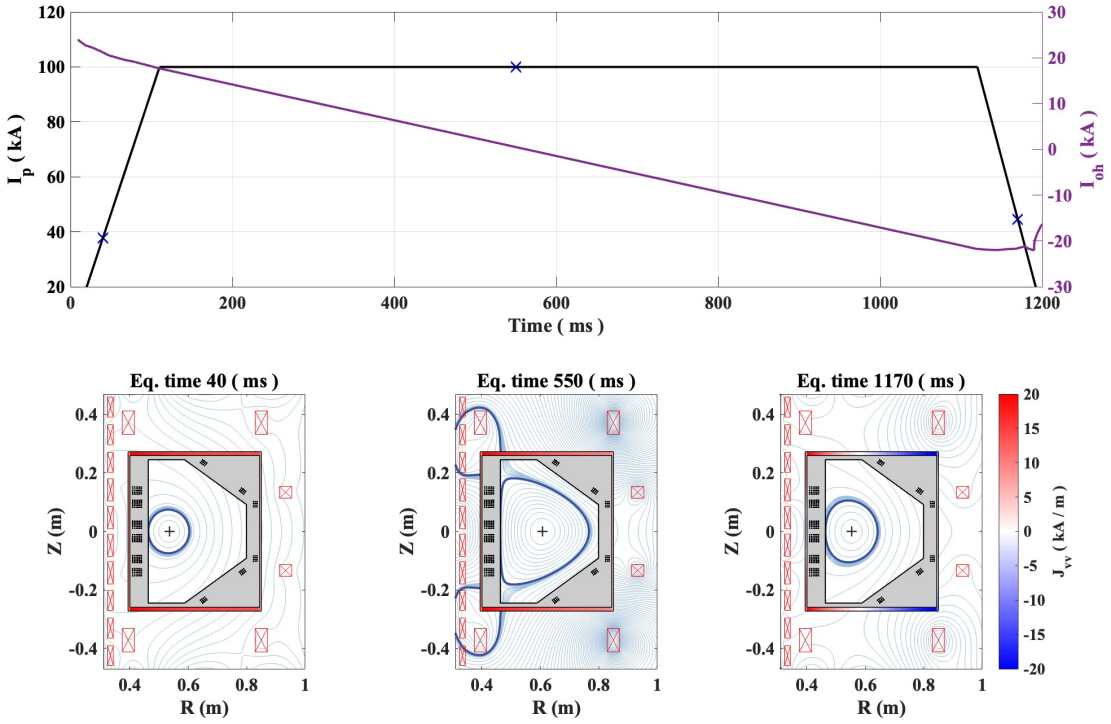

Figure 5.15: Time evolution of a limited plasma with positive triangularity at three points in time.

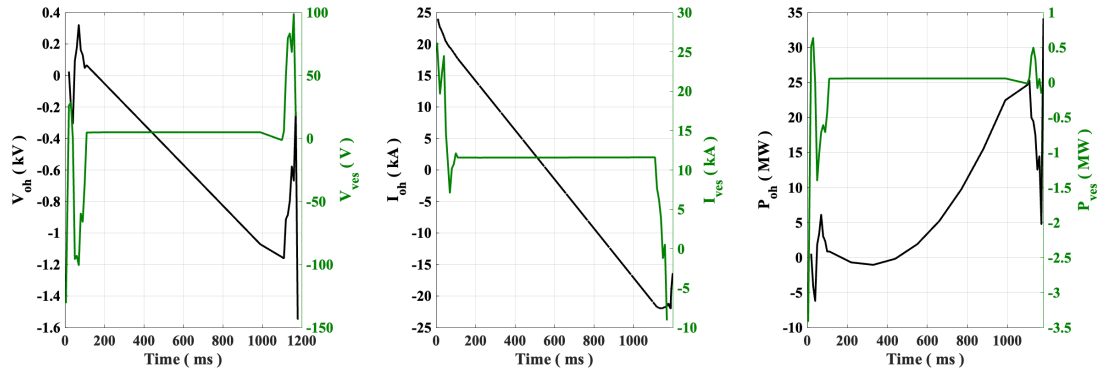

Figure 5.16: Time evolution of the voltage, current, and power on the Ohmic and vacuum vessel (induced) for a plasma with positive triangularity.

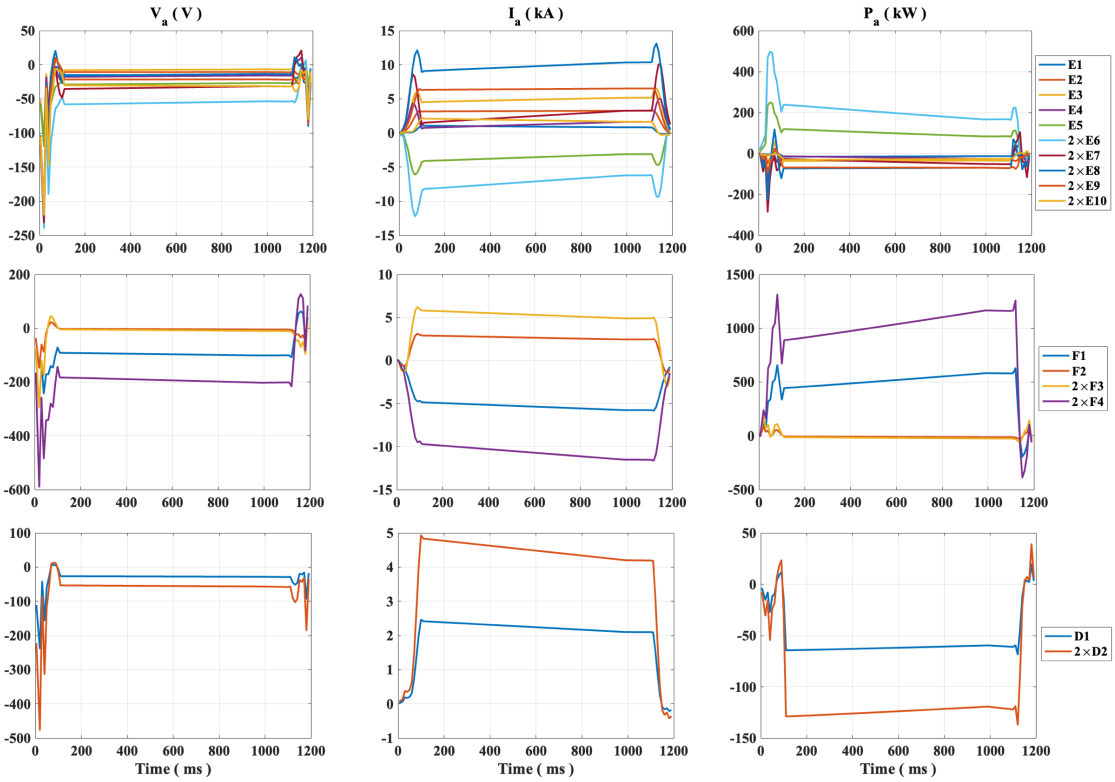

Figure 5.17: Time evolution of the voltage, current, and power on each PF coil for a plasma with positive triangularity.

Negative triangularity plasma

The plasma with negative triangularity is modeled to achieve a plasma current at the flat-top with $I_p = 80\,\text{kA}$ and with elongation of $\kappa = 1.1$ and with triangularity of $\delta = -1.2$. The current is ramped-up until it reaches this flat-top value along with its final triangular shape. The simulation of this limited plasma is shown in Figure 5.18. The first row of this figure shows the prescribed plasma current, followed by the calculated evolution of the Ohmic current pictured on the second row and the evolution of the plasma shape on the last row. We notice that, to induce the prescribed plasma current, the Ohmic system have to operate with currents of $I_{\text{OH}} = \pm 24\,\text{kA}$ and voltages varying from $V_{\text{OH}} \approx 0.1\,\text{kV}$ to $V_{\text{OH}} \approx -1.2\,\text{kV}$, as shown in Figure 5.19. To obtain the evolution of the shape, the PF coil currents will have to provide currents and voltages up to $|I_a| = 7.5\,\text{kA}$, and $|V_a| = 150\,\text{V}$, respectively. These results are presented in Figure 5.20.

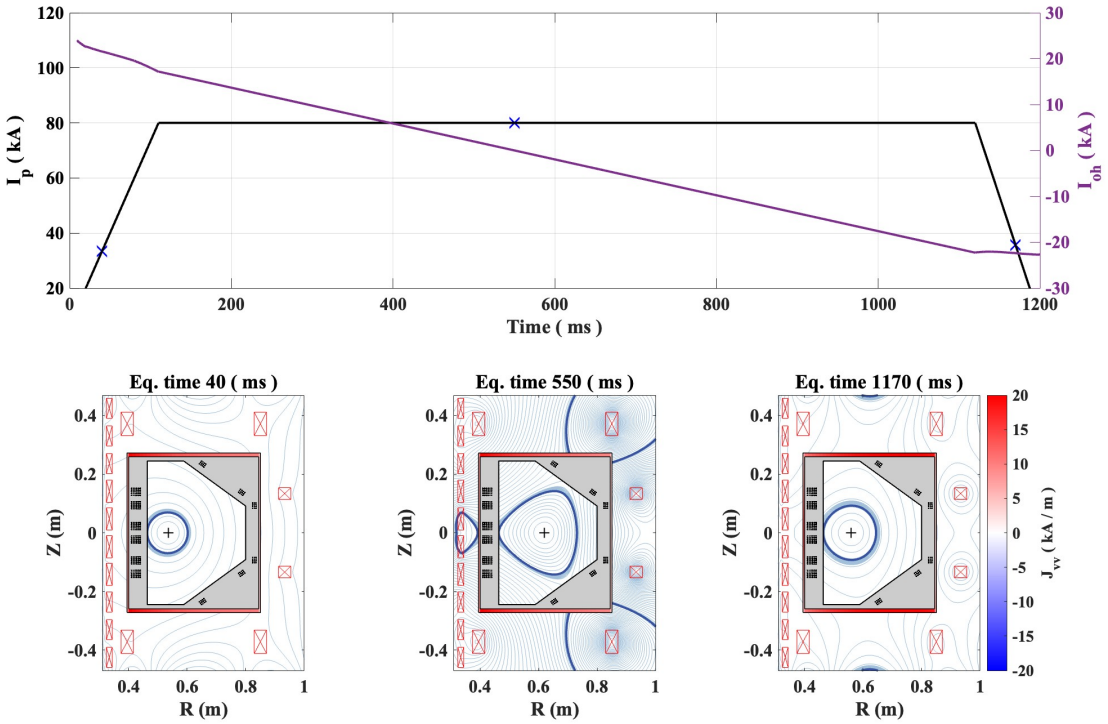

Figure 5.18: Time evolution of a limited plasma with negative triangularity at three points in time.

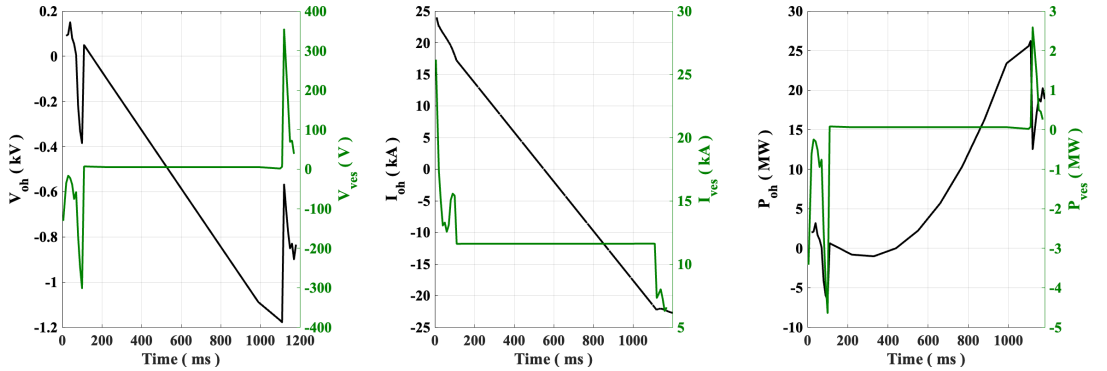

Figure 5.19: Time evolution of the voltage, current, and power on the Ohmic and vacuum vessel (induced) for a plasma with negative triangularity.

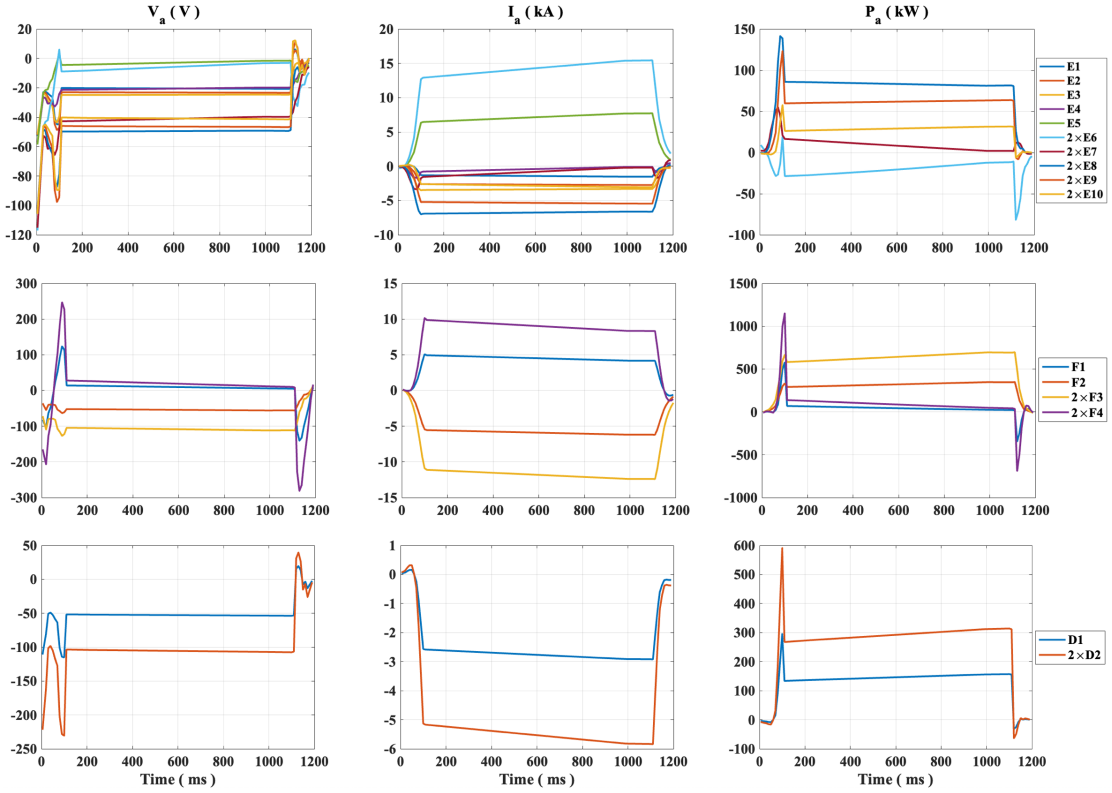

Figure 5.20: Time evolution of the voltage, current, and power on each PF coil for a plasma with negative triangularity.

Squared plasma

The squared plasma is modeled to achieve a plasma current at the flat-top with $I_p = 100\,\text{kA}$ and with squareness of $\zeta = 1.0$. The plasma current is ramped-up until it reaches the flat-top value along with its final squared shape. The simulation of this limited plasma is shown in Figures 5.21. The first row of this figure shows the prescribed plasma current, followed by the calculated evolution of the Ohmic current pictured on the second row and the evolution of the plasma shape on the last row. We notice that to induce the prescribed plasma current, the Ohmic system will have to operate with currents of $I_{\text{OH}} = \pm 24\,\text{kA}$ and voltages varying from $V_{\text{OH}} \approx 0.3\,\text{kV}$ to $V_{\text{OH}} \approx -2.2\,\text{kV}$, as shown in Figure 5.22. To obtain the evolution of the circular shape, the PF coil power supplies will have to provide currents and voltages of up to $|I_a| = 7.5\,\text{kA}$, and $|V_a| = 250\,\text{V}$, respectively. These results are presented in Figure 5.23.

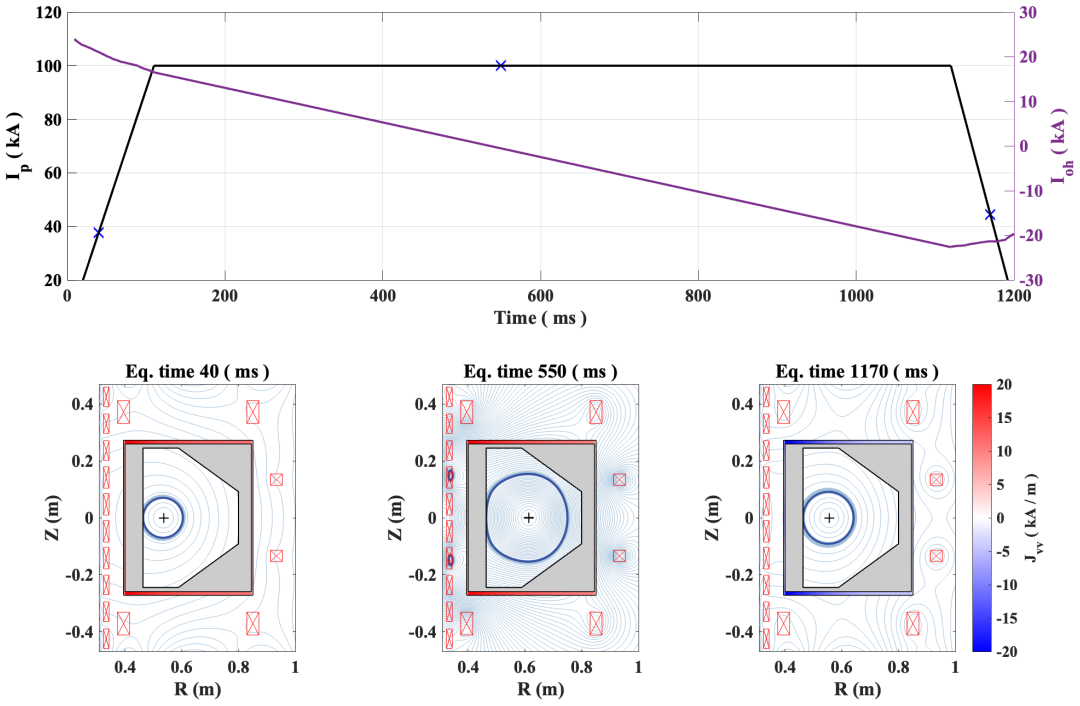

Figure 5.21: Time evolution of a squared plasma at three points in time.

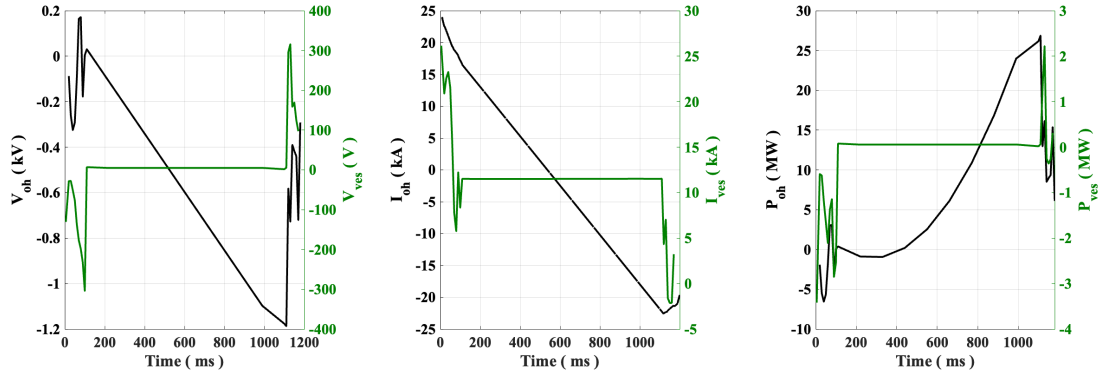

Figure 5.22: Time evolution of the voltage, current, and power on the Ohmic and vacuum vessel (induced) for a squared plasma.

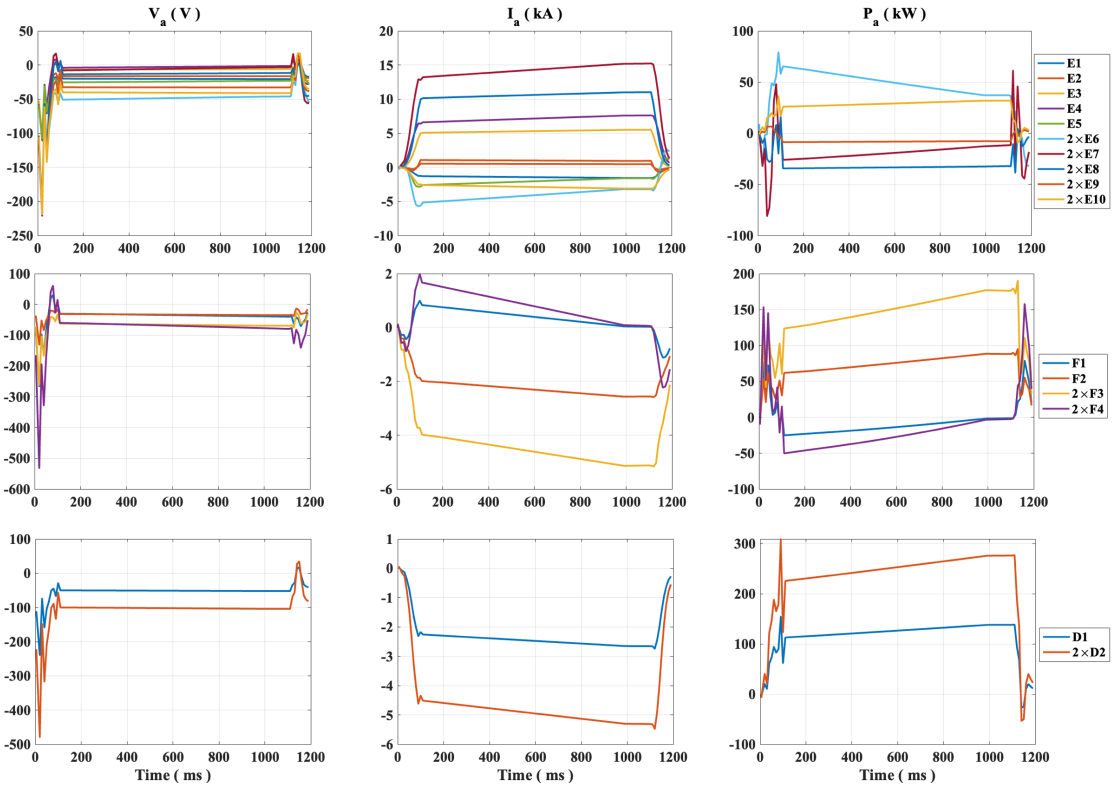

Figure 5.23: Time evolution of the voltage, current, and power on each PF coil for a squared plasma.

5.3.2 Diverted plasmas

In this section, the design of three diverted scenarios is presented with the time evolution of each coil current and voltage needed to prescribe the desired LCFS. Diverted plasmas are characterized by the LCFS being the one that passes through an X-point. The plasma is started at the breakdown position with a current $I_p = 10$ kA and Ohmic current $I_{OH} = 24$ kA.

Lower single-null plasma

The single-null plasma with a negative Z position is modeled to achieve a plasma current at the flat-top $I_p = 105$ kA, with elongation $\kappa = 1.35$, lower triangularity $\delta_\ell = 1.0$ and upper triangularity $\delta_u = 0.1$. The plasma current is ramped-up until it reaches the flat-top value along with its final circular shape. The simulation of this limited plasma is shown in Figures 5.24. The first row of this figure shows the prescribed plasma current, followed by the calculated evolution of the Ohmic current pictured on the second row and the evolution of the plasma shape on the last row. We notice that to induce the prescribed plasma current, the Ohmic system will have to operate with currents $I_{\mathrm{OH}} = \pm 24$ kA and voltages varying from $V_{\mathrm{OH}} \approx 0.75$ kV to $V_{\mathrm{OH}} \approx -1.5$ kV, Figure 5.25. To obtain the evolution of the diverted shape, the PF coil power supplies will have to provide currents and voltages of up to $|I_a| = 6.0$ kA, and $|V_a| = 250$ V, respectively. These results are presented in Figure 5.26.

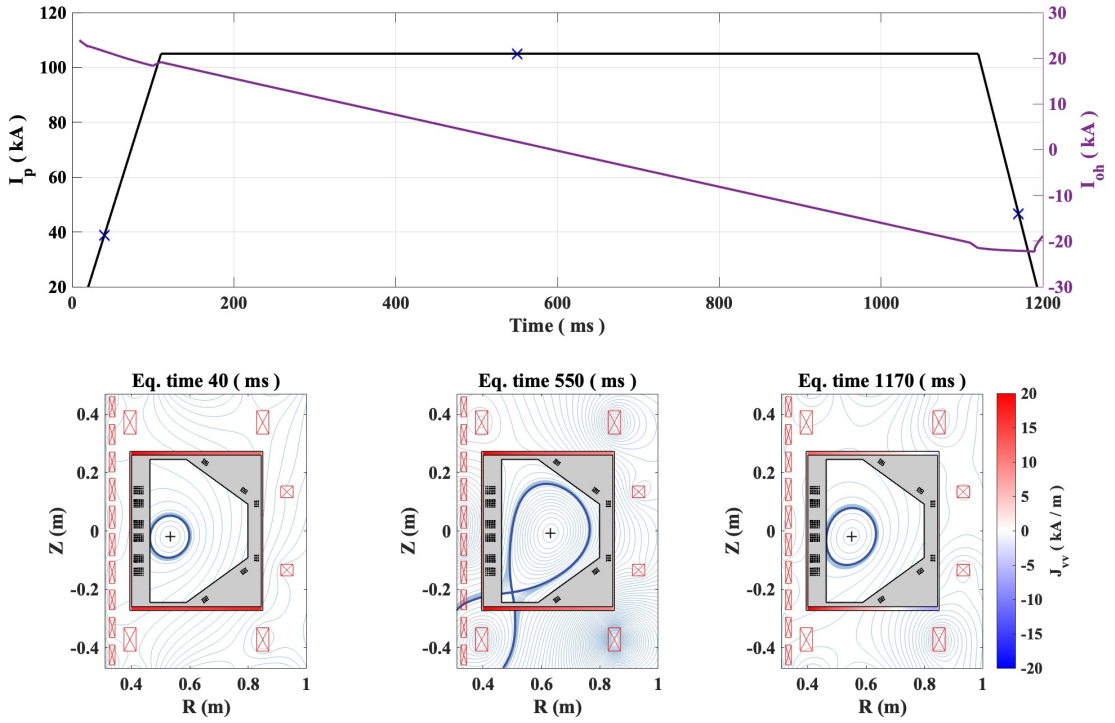

Figure 5.24: Time evolution of a diverted plasma at three points in time.

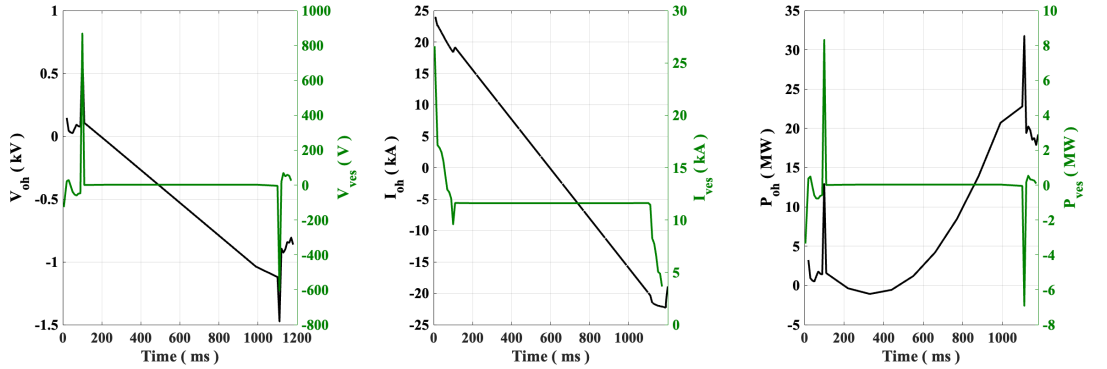

Figure 5.25: Time evolution of the voltage, current, and power on the Ohmic and vacuum vessel (induced) for a diverted plasma.

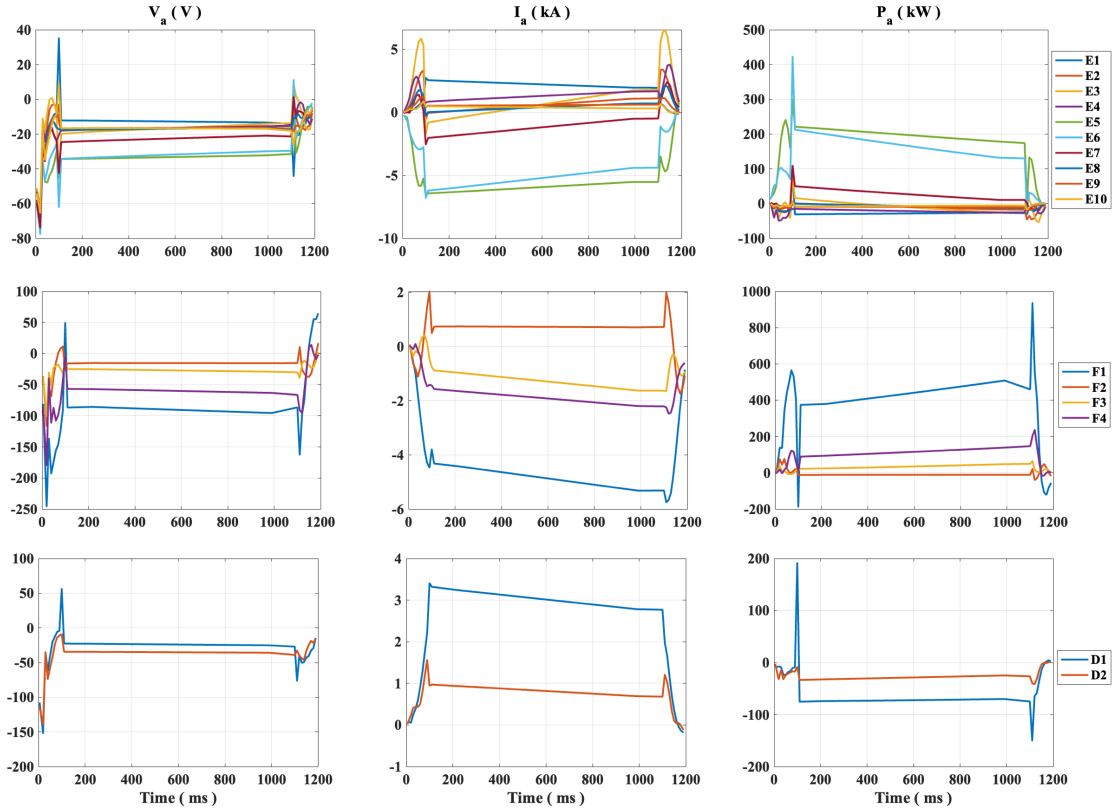

Figure 5.26: Time evolution of the voltage, current, and power on each PF coil for a diverted plasma.

Upper single-null plasma

The diverted plasma with a single-null with a positive Z position is modeled to achieve a plasma current at the flat-top with I_p = 105 kA with elongation of κ = 1.35, lower triangularity of δ_ℓ = 0.1 and upper triangularity of δ_u = 1.0. The plasma current is ramped-up until it reaches the flat-top value along with its final circular shape. The simulation of this limited plasma is shown in Figures 5.27. The first row of this figure shows the prescribed plasma current, followed by the calculated evolution of the Ohmic current pictured on the second row and the evolution of the plasma shape on the last row. We notice that to induce the prescribed plasma current, the Ohmic system will have to operate with currents of $I_{\mathrm{OH}} = \pm 24$ kA and voltages varying from $V_{\mathrm{OH}} \approx 0.75$ kV to $V_{\mathrm{OH}} \approx -1.5$ kV, as shown in Figure 5.28. To obtain the evolution of the diverted shape, the PF coil power supplies will have to provide currents and voltages of up to $|I_a| = 6.0$ kA, and $|V_a| = 250$ V, respectively. These results are presented in Figure 5.29.

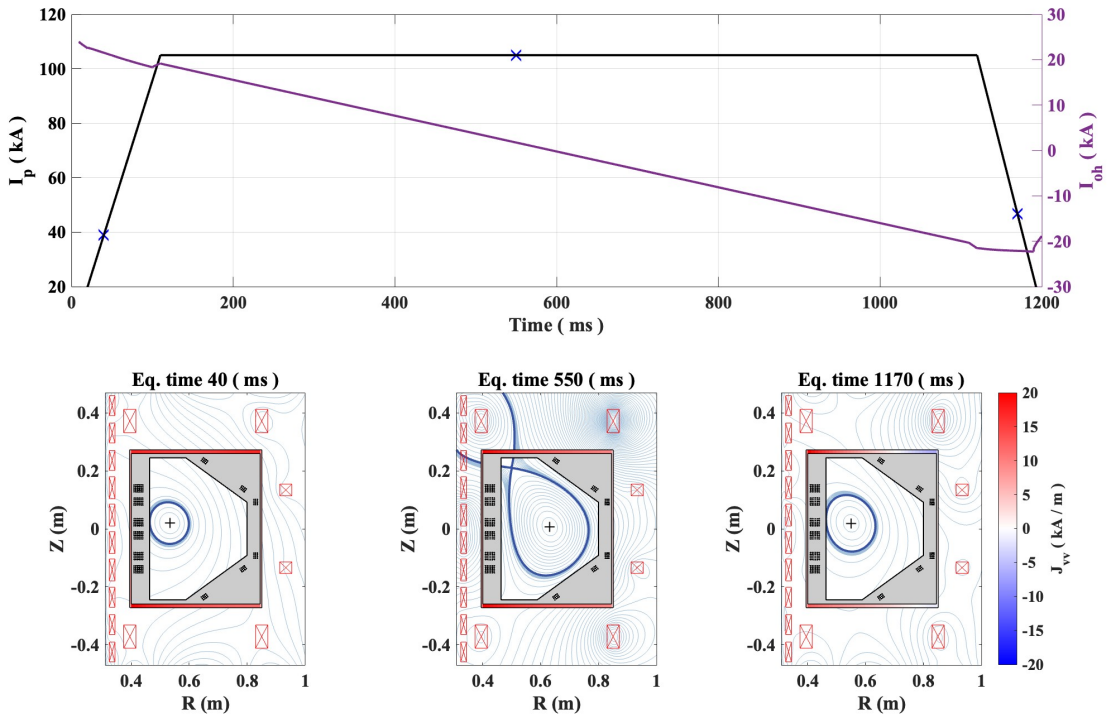

Figure 5.27: Time evolution of a diverted plasma at three points in time.

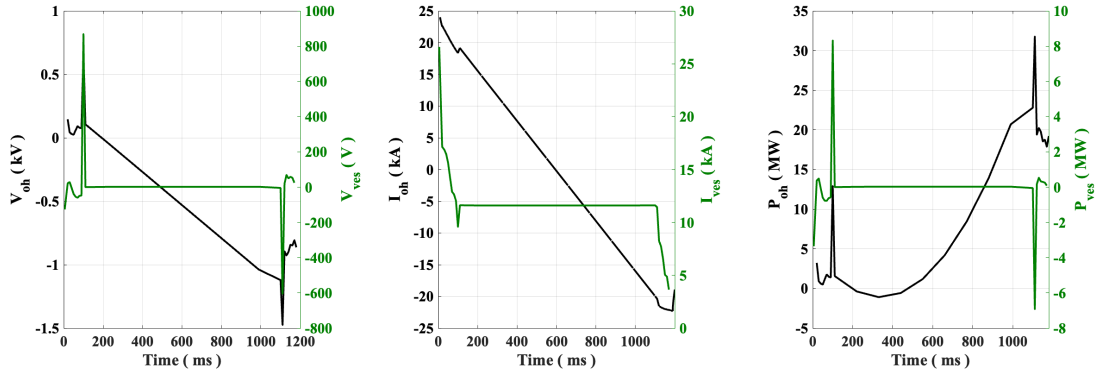

Figure 5.28: Time evolution of the voltage, current, and power on the Ohmic and vacuum vessel (induced) for a diverted plasma.

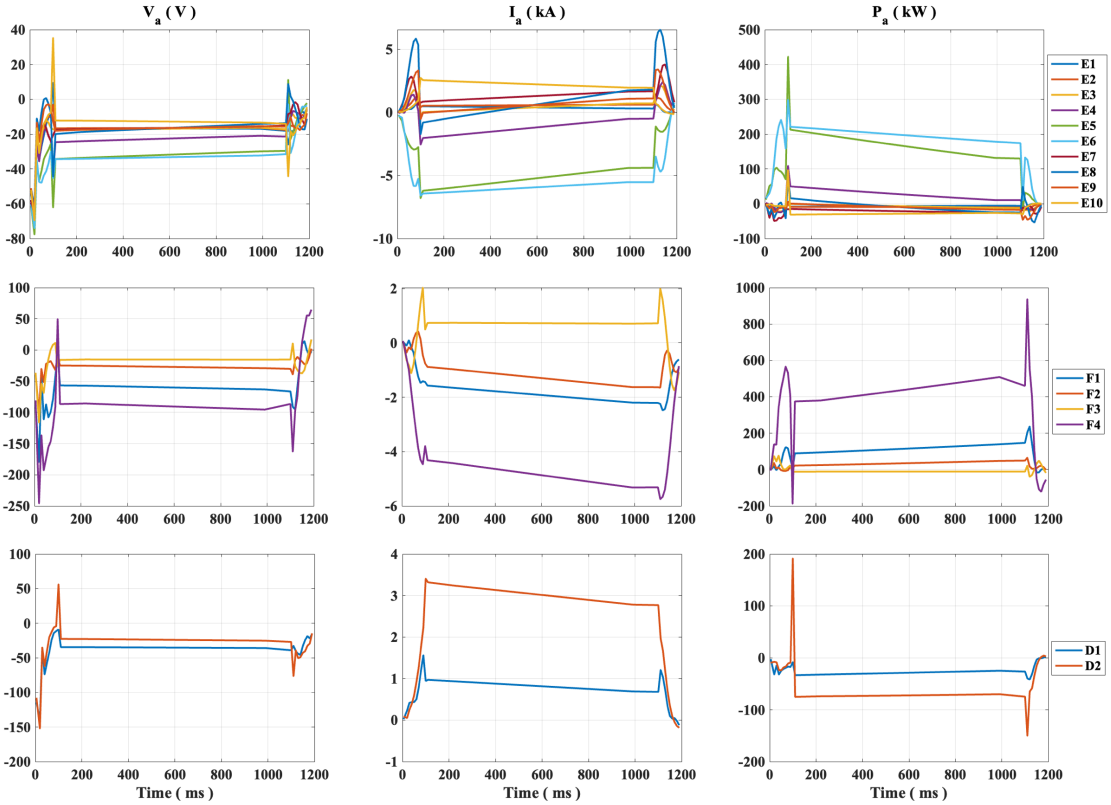

Figure 5.29: Time evolution of the voltage, current, and power on each PF coil for a diverted plasma.

Double-null plasma

The diverted plasma with a double-null is modeled to achieve a plasma current at the flat-top with $I_p = 110\,\text{kA}$ with elongation of $\kappa = 1.4$, lower and upper triangularities of $\delta = 0.8$. The plasma current is ramped-up until it reaches the flat-top value along with its final circular shape. The simulation of this limited plasma is shown in Figures 5.30. The first row of this figure shows the prescribed plasma current, followed by the calculated evolution of the Ohmic current pictured on the second row and the evolution of the plasma shape on the last row. We notice that to induce the prescribed plasma current, the Ohmic system will have to operate with currents of $I_{\text{OH}} = \pm 24\,\text{kA}$ and voltages varying from $V_{\text{OH}} \approx 1.0\,\text{kV}$ to $V_{\text{OH}} \approx -1.5\,\text{kV}$, as shown in Figure 5.31. To obtain the evolution of the diverted shape, the PF coil power supplies will have to provide currents and voltages of up to $|I_a| = 9.0\,\text{kA}$, and $|V_a| = 250\,\text{V}$, respectively. These results are presented in Figure 5.32.

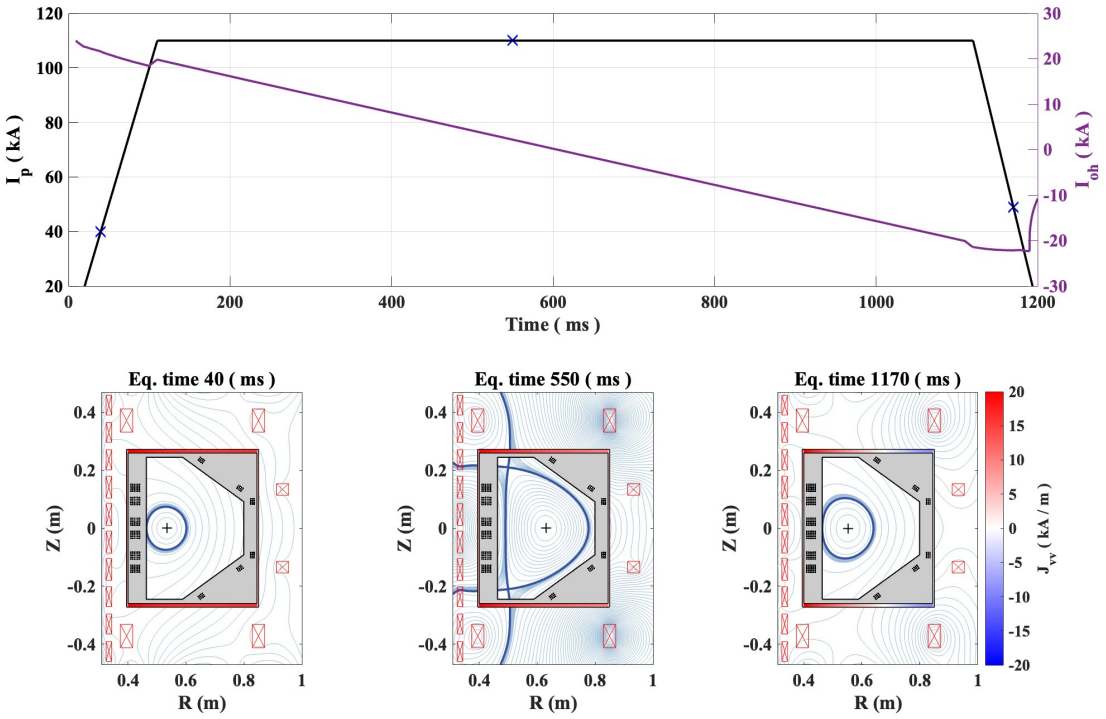

Figure 5.30: Time evolution of a diverted plasma at three points in time.

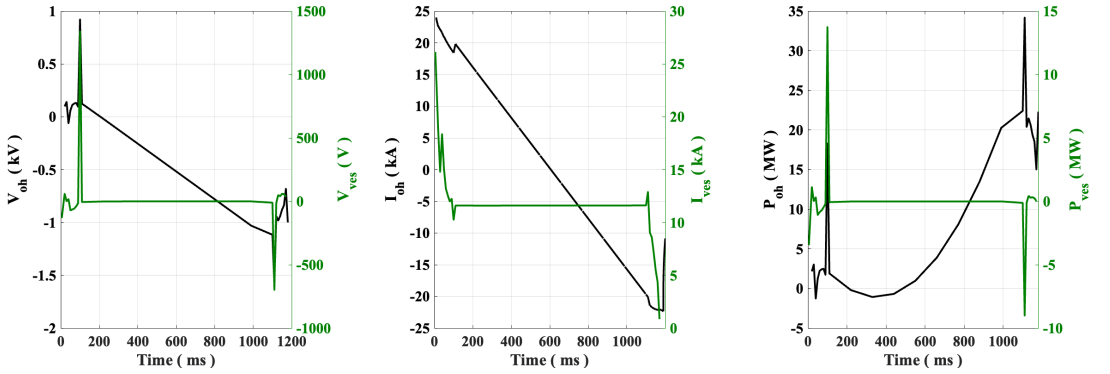

Figure 5.31: Time evolution of the voltage, current, and power on the Ohmic and vacuum vessel (induced) for a diverted plasma.

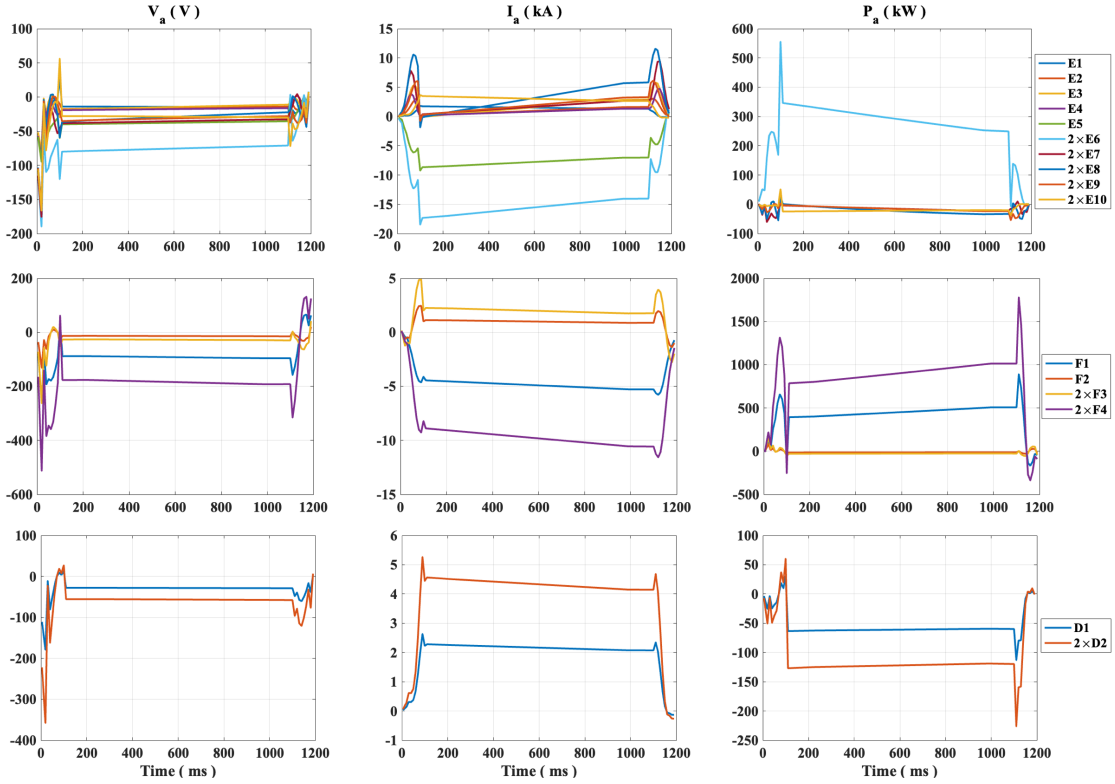

Figure 5.32: Time evolution of the voltage, current, and power on each PF coil for a diverted plasma.

Snowflake plasma

The snowflake plasma with a second order null-point is modeled to achieve a plasma current at the flat-top with $I_p = 80\,\text{kA}$ with elongation of $\kappa = 1.35$, lower triangularity of $\delta_\ell = 1.0$ and upper triangularity of $\delta_\ell = 0.5$. The plasma current is ramped-up until it reaches the flat-top value along with its final circular shape. The simulation of this limited plasma is shown in Figures 5.33. The first row of this figure shows the prescribed plasma current, followed by the calculated evolution of the Ohmic current pictured on the second row and the evolution of the plasma shape on the last row. We notice that to induce the prescribed plasma current, the Ohmic system will have to operate with currents of $I_{\text{OH}} = \pm 24\,\text{kA}$ and voltages varying from $V_{\text{OH}} \approx 4.0\,\text{kV}$ to $V_{\text{OH}} \approx -4.0\,\text{kV}$, as shown in Figure 5.34. To obtain the evolution of the diverted shape, the PF coil power supplies will have to provide currents and voltages of up to $|I_a| = 25.0\,\text{kA}$, and $|V_a| = 300\,\text{V}$, respectively. These results are presented in Figure 5.35.

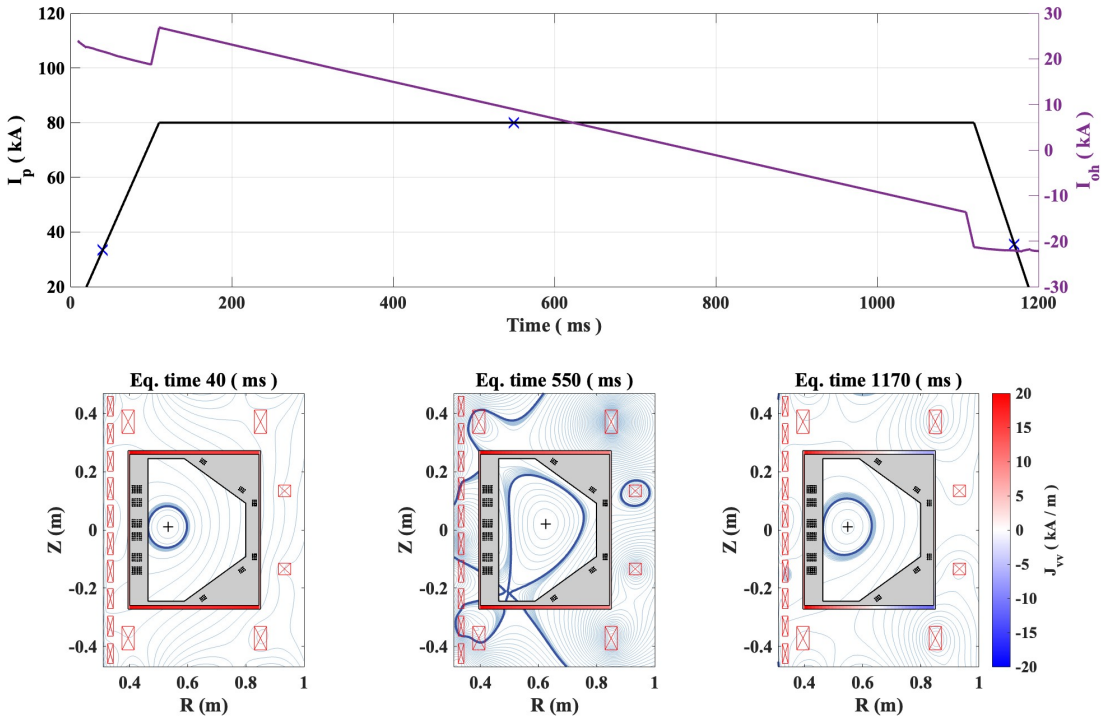

Figure 5.33: Time evolution of a snowflake plasma at three points in time.

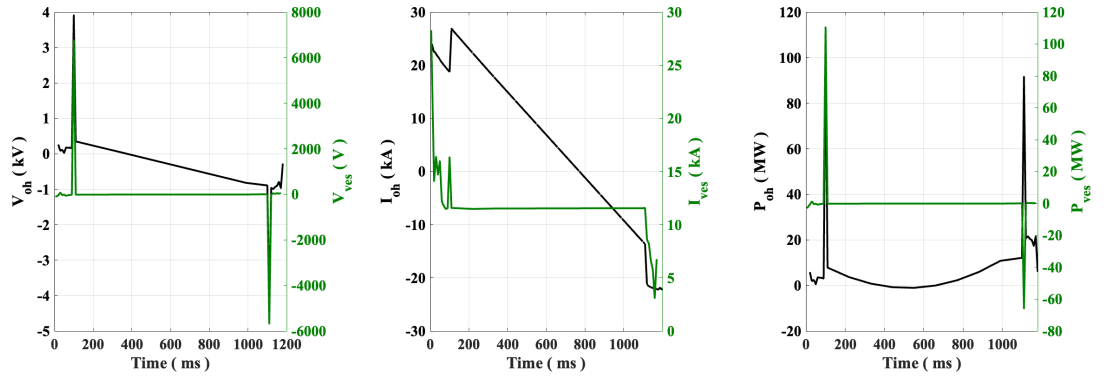

Figure 5.34: Time evolution of the voltage, current, and power on the Ohmic and vacuum vessel (induced) for a snowflake plasma.

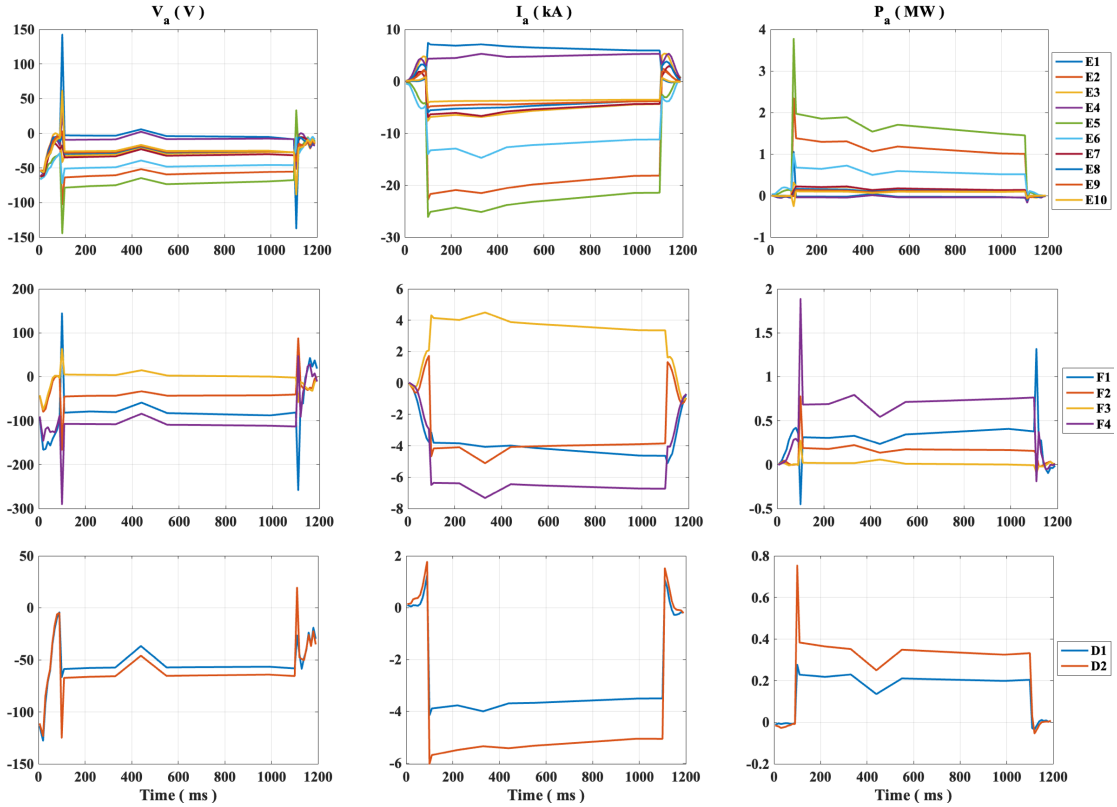

Figure 5.35: Time evolution of the voltage, current, and power on each PF coil for a snowflake plasma.

5.3.3 The impact of the vacuum vessel on the PFC currents

At each step of the Picard iteration, the induced currents in the vacuum vessel was calculated by linearising the electrical parameters related to the plasma and active coils, as described in Section 5.3. The inclusion of the vacuum vessel in a self-consistent way, allowed the prediction of its impact on the plasma shape, which was compensated by the PF coil currents, since, as observed on the second row of Figures 5.10, 5.13, 5.16, 5.19, 5.22, 5.25, 5.28, 5.31, and 5.34, the induced vacuum vessel currents are of the order of 10 kA during the flat-top phase.

In the following, we present the difference in the PF coil currents for the circular scenario when the vacuum vessel is included and when it is neglected, although the results are also valid for the eight developed scenarios. We observe from the results presented in Figures 5.36 and 5.37 a maximum difference of the order of 0.2 kA on the time evolution of the PF coil currents when the vacuum vessel is include self-consistently. This corresponds to an error of around 10% in the PF coils when the induced vessel currents are not take into account.

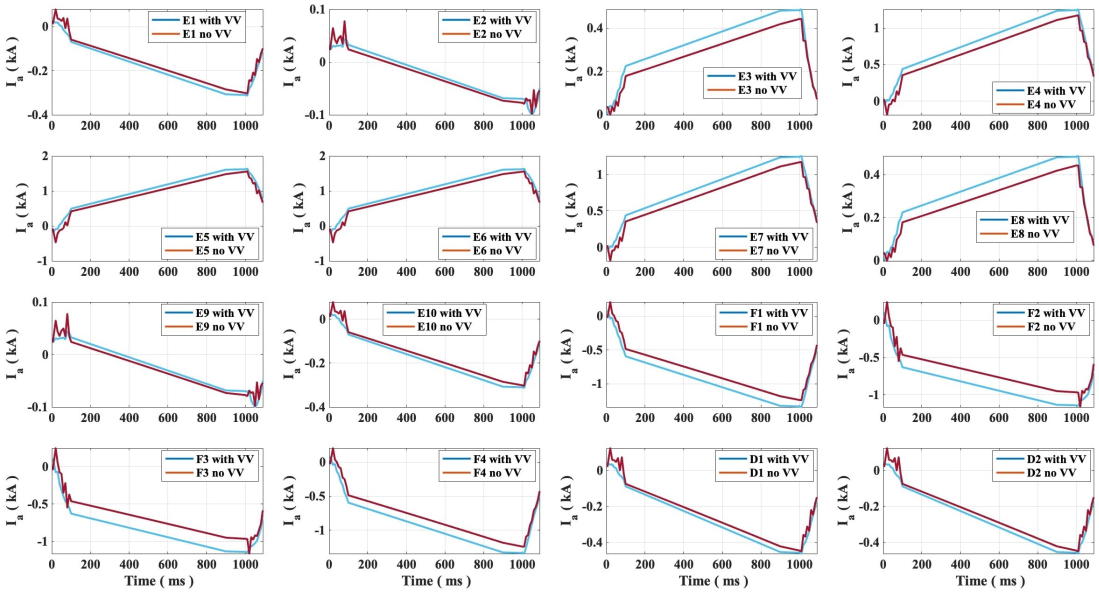

Figure 5.36: PF coil currents with and without the inclusion of the vacuum vessel for the circular plasma

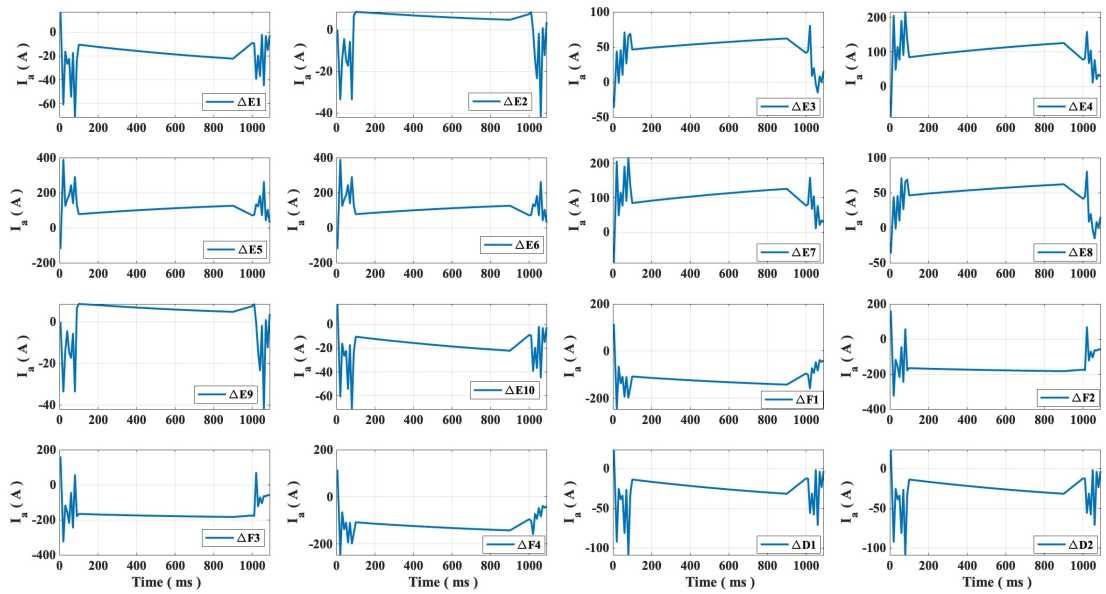

Figure 5.37: Difference on the PF coil currents when the vacuum vessel is included. Here $\Delta = I_{\text{with VV}} - I_{\text{no VV}}$.

5.3.4 Summary and discussion

The results regarding the voltages and currents in the active coils for different plasma scenarios were presented. One main observation that is present on all Ohmic and PF coil voltages, and also on the PF coil currents is a rapid change on the amplitudes when the plasma changes from the ramp-up to the flat-top phase (at $t = 100$ ms) and from the flat-top to the ramp-down phase (at $t = 1110$ ms). This is a numerical phenomena related to the derivative of the plasma current at that point. It changes relatively fast and therefore it induces a large voltage in the Ohmic system and imposes also a peaked voltage in the PF coils. This phenomena is also present in the diverted plasmas and it appears to be stronger because the X-point (and even stronger for the snowflake configuration) is created at these transitions, i.e., the currents in the PF coils must suddenly yield a magnetic field that helps creating a null in the total poloidal magnetic field at that point (and a second order null-point for the SF). One way to surpass this rapid change would be simulate a smoother transition from ramp-up to flat-top phase, and also from flat-top to ramp-down phase, and imposes a smoothly decrease on the poloidal magnetic field component during the ramp-up phase til it reaches zero at flat-top.

Another interesting result that can be seen during the flat-top phase of all plasma scenarios is that the currents in the PF coils change in time even though the plasma shape is kept fixed. This is because in order to keep the plasma current constant, it is necessary to vary the current in the ohmic system during the entire flat-top phase. This will affect the impact of the poloidal flux produced by the ohmic system on the plasma, and consequently, would change its shape.

6 Conclusions and outlook

In this work, a computational tool for designing the evolution of plasma scenarios in TCABR was developed. The main goal was to estimate the time evolution of each coil current and voltage for some of the main plasma scenarios envisaged for TCABR. The simulations show that the power supplies acting on the Ohmic and PF coils systems will have to operate in the four quadrants of a current-voltage operational space and provide voltages and currents of up to $V_{\mathrm{OH}} = \pm 2.3\,\mathrm{kV}$/ $I_{\mathrm{OH}} = \pm 24\,\mathrm{kA}$, and $V_a = \pm 300\,\mathrm{V}$/ $I_a = \pm 9.0\,\mathrm{kA}$. The maximum positive values of voltage for the Ohmic system and PF coils would have been obtained if we had simulated plasmas with negative currents. These results are valid for all the developed plasma scenarios apart from the snowflake configuration, which required relatively high voltages and currents on the PF coils. Therefore, its feasibility still requires some further development.

Regarding the simulations at a specific point in the operational space, one interesting result that one observed, just by imposing a few physical constraints, was the diamagnetic property of the plasma. In order to fully explain this phenomena, it would require a detailed study of the transport equations. However, it is important to mention that the choice of the kinetic profiles have a direct impact on the equilibrium and, consequently, on the calculation of the currents and voltages on the PF coils. Depending on the choice of the pressure profile, the plasma could behave as paramagnetic, i.e. it would increase the toroidal magnetic field within its domain.

It is important to note that, although we demonstrated that the kinetic profiles are not so important for the calculation of the PF coil currents, provided that they obey the imposed constraints, prescribing a realistic (or as closed as possible) pressure and poloidal current function profiles are necessary for characterizing the stability of an envisaged TCABR plasma scenario. Additionally, the inclusion of the vacuum vessel in a self-consistent way was demonstrated to have a small impact on the PF coil currents but its account turn the problem more realistic.

Finally, this work serves as a guideline study for prospect students who want to work with plasma scenarios and equilibrium simulations, since it presents the basic aspects of the Plasma Scenario Development (PSD) code.

A Magnetic flux coordinates in a torus

As seen throughout this work, we have deployed a axissymetric orthonormal cylindrical coordinate system (R,ϕ,Z) to describe our magnetic equilibrium configuration and kinetic profiles, once $\Psi = \Psi(R,Z)$. But there is also another convenient way to define our space which is to use coordinates defined by the magnetic field itself. In addition to simplifying of the magnetic field, this approach can also provide a general theory for all the toroidal devices.

We start by introducing the general coordinates $(\psi(\mathbf{r}),\theta(\mathbf{r}),\zeta(\mathbf{r}))$, as shown in Fig. (A.1).

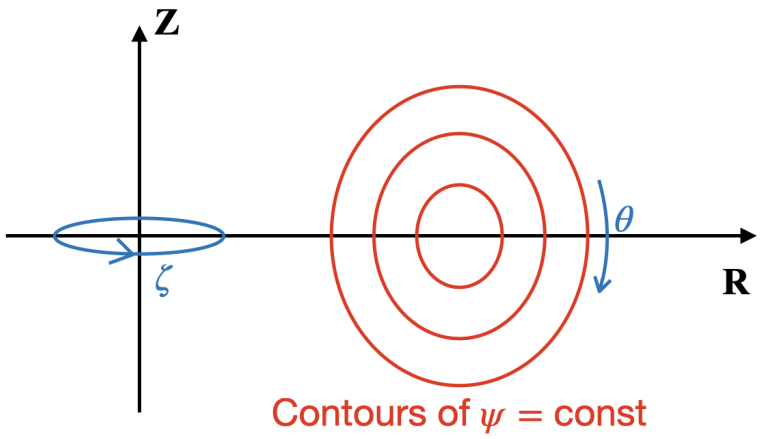

Figure A.1: General toroidal coordinates

Here, surfaces of constant ψ consist of nested tori where its axis is represented by the contour with $\psi_{\text{axis}} = \max\{\psi\}$. The θ and ζ are the general poloidal and toroidal angles, respectively.

Defined the coordinate system with non-coplanar gradients, the Jacobian is given by

$$\mathscr{J}^{-1} = \left(\nabla\psi \times \nabla\theta\right)\cdot\nabla\zeta. \tag{A.1}$$

In order these to be a magnetic flux coordinate system that represents a tokamak, we choose

ψ and ζ to be such that

$$\mathbf{B}\cdot\nabla\psi = 0, \text{ and } \frac{\partial}{\partial\zeta} = 0. \tag{A.2}$$

A.1 Metric element

We have introduced the coordinate functions $\psi = \psi(R,Z)$ and $\theta = \theta(R,Z)$ and now we have the inverse relation $R = R(\psi,\theta)$ and $Z = Z(\psi,\theta)$. Therefore,

$$\nabla R = \frac{\partial R}{\partial\psi}\nabla\psi + \frac{\partial R}{\partial\theta}\nabla\theta, \tag{A.3}$$

$$\nabla Z = \frac{\partial Z}{\partial\psi}\nabla\psi + \frac{\partial Z}{\partial\theta}\nabla\theta. \tag{A.4}$$

Inverting the above relations we end up with

$$\nabla\psi = \frac{R}{\mathscr{J}}\left(-\frac{\partial Z}{\partial\theta}\nabla R + \frac{\partial R}{\partial\theta}\nabla Z\right), \tag{A.5}$$

$$\nabla\theta = \frac{R}{\mathscr{J}}\left(\frac{\partial Z}{\partial\psi}\nabla R - \frac{\partial R}{\partial\psi}\nabla Z\right). \tag{A.6}$$

One important relation that can be derived from the above equations is the arc length along a constant ψ contour, $d\ell$, defined as

$$\frac{d\ell}{d\theta} = \sqrt{\left(\frac{\partial R}{\partial\theta}\right)^2 + \left(\frac{\partial Z}{\partial\theta}\right)^2}. \tag{A.7}$$

Using the Eq. (A.5), we can rewrite $d\ell$ in a more convenient way

$$d\ell = \frac{|\nabla\psi|\,\mathscr{J}}{R}d\theta, \tag{A.8}$$

that will be used in the following.

A.2 Flux averages

In order to derive some important quantities of tokamak physics, such as safety factor and surface averages, our magnetic flux coordinate system needs to represent a tokamak, i.e., it

must satisfy Eq. (A.2). We start by introducing the volume within a flux surface defined as

$$V(\psi) = \int d\tau = \underbrace{\int_0^{2\pi} d\zeta}_{\text{can be calculated}} \int_{\psi_0}^{\psi} d\psi' \int_0^{2\pi} d\theta \, \mathscr{J}, \Rightarrow$$

$$\Rightarrow V(\psi) = 2\pi \int_{\psi_0}^{\psi} d\psi' \int_0^{2\pi} d\theta \, \mathscr{J}. \tag{A.9}$$

Differentiating with respect to the upper ψ limit gives the differential volume

$$V'(\psi) \equiv \frac{dV}{d\psi} = 2\pi \int_0^{2\pi} d\theta \, \mathscr{J}, \tag{A.10}$$

and using Eq.(A.8) we get

$$V'(\psi) = 2\pi \oint \frac{R}{|\nabla\psi|} d\ell. \tag{A.11}$$

Given any scalar quantity $Q = Q(\psi, \theta)$, we can define a flux average, or surface average, of Q over a constant ψ contour as

$$\langle Q \rangle = \frac{2\pi}{V'} \int_0^{2\pi} d\theta \, \mathscr{J} \, Q = \frac{2\pi}{V'} \oint \frac{R}{|\nabla\psi|} Q \, d\ell. \tag{A.12}$$

If our magnetic flux coordinate ψ is the poloidal magnetic flux, i.e. $\psi = \Psi$, we have that

$$\mathbf{B}_\theta = \frac{1}{2\pi R} \nabla\psi \times \hat{e}_\phi \Rightarrow |\mathbf{B}_\theta| = \frac{1}{2\pi R} |\nabla\psi| \Rightarrow \frac{R}{|\nabla\psi|} = \frac{1}{2\pi} \frac{1}{|\mathbf{B}_\theta|} \tag{A.13}$$

and therefore, we can rewrite the surface average now in terms of the poloidal component of the magnetic field as

$$\langle Q \rangle = \frac{\oint \frac{Q}{|\mathbf{B}_\theta|} d\ell}{\oint \frac{d\ell}{|\mathbf{B}_\theta|}}. \tag{A.14}$$

A.3 Safety factor

The safety factor is define as the number of toroidal turns a magnetic field line needs to go around the torus in order to close up on itself. Mathematically, can be described as the derivative of the toroidal magnetic flux, Φ, with respect to the poloidal magnetic flux $\psi = \Psi$, i.e.

$$q = -\frac{d\Phi}{d\psi}. \tag{A.15}$$

The toroidal magnetic flux is defined as

$$\Phi = \iint_{S_{\text{tor}}} \mathbf{B} \cdot d\mathbf{S}, \text{ with } d\mathbf{S} = dR\, dZ\, \hat{e}_\phi.$$

Manipulating the above equation

$$\Phi = \iint_{S_{\text{tor}}} \underbrace{\left(\mathbf{B} \cdot \frac{\hat{e}_\phi}{R}\right)}_{\mathbf{B}\cdot\nabla\phi} R\, dR\, dZ \frac{1}{2\pi} \underbrace{2\pi}_{\int_0^{2\pi} d\phi} = \frac{1}{2\pi} \iiint \underbrace{(\mathbf{B}\cdot\nabla\phi)}_{F(\psi)/R^2} \underbrace{R\, dR\, dZ\, d\phi}_{\mathscr{J}\, d\psi\, d\theta\, d\phi} \Rightarrow$$

$$\Rightarrow \Phi = \frac{1}{2\pi} \int_{\psi_0}^{\psi} d\psi' \int_0^{2\pi} d\phi \int_0^{2\pi} \frac{F(\psi)}{R^2} \mathscr{J}\, d\theta = \frac{1}{2\pi} \int_{\psi_0}^{\psi} d\psi'\, F(\psi') \left(2\pi \int_0^{2\pi} d\theta\, \mathscr{J} \frac{1}{R^2}\right).$$

By using Eq. (A.12) we obtain

$$\Phi(\psi) = \frac{1}{2\pi} \int_{\psi_0}^{\psi} d\psi'\, F(\psi') \frac{dV}{d\psi'} \left\langle \frac{1}{R^2} \right\rangle. \tag{A.16}$$

Finally, differentiating the above equation with respect to the upper limit ψ, we get the safety factor

$$q(\psi) = -\frac{1}{2\pi} F(\psi) \frac{dV}{d\psi} \left\langle \frac{1}{R^2} \right\rangle. \tag{A.17}$$

Bibliography

[1] FROCHTZWAJG, J.. *The secretive, billionaire-backed plans to harness fusion*, 2016. Available from: https://www.bbc.com/future/article/20160428-the-secretive-billionaire-backed-plans-to-harness-fusion Accessible at: April 28, 2016.

[2] Office of Nuclear Energy. *Fission and Fusion: What is the Difference?*, 2021. Available from: https://www.energy.gov/ne/articles/fission-and-fusion-what-difference Accessible at: April 1, 2021.

[3] COWLEY, S.C. *The quest for fusion power*, 2016.Available from: https://www.nature.com/articles/nphys3719.Accessible at: March 04,2021.

[4] BISHOP, B. *National Ignition Facility experiment puts researchers at threshold of fusion ignition.*, 2021. Avaliable from: https://www.llnl.gov/news/national-ignition-facility-experiment-puts-researchers-threshold-fusion-ignition?fbclid=IwAR2r-VVqWX0LumsF5jAKyKzhTlP7N9jlZcPZiAHVVWxtFfsi19mAPe_xTo0. Accessible at: August 18, 2021.

[5] WESSON, J. A.. *Tokamaks*, 2nd. ed. Oxford: Clarendon Press, 1997.

[6] BICKERTON, R. J., *et al. Diffusion driven plasma currents and bootstrap tokamak. Nature Physical Science*, 229:110-111, 1971. Available from: https://www.nature.com/nature-physci/journal/v229/n4/abs/physci229110a0.html.

[7] SAUTER, O. *et al. Steady-state fully noninductive current driven by electron cyclotron waves in a magnetically confined plasma. Physical Review Letters*, 88:3322-3325,2000. Available from: http://link.aps.org/doi/10.1103/PhysRevLett.84.3322.

[8] ONGENA, J., ZOHM, H. *et al. Magnetic-confinement fusion. Nature Physics*, 398–410. doi:10.1038/nphys3745. Available from: https://www.nature.com/articles/nphys3818. Accessible at: May 03, 2016.

[9] ZOHM, H.. *Magnetohydrodynamic Stability of Tokamaks*. Weinheim: Wiley-VCH, 2015.

[10] ARIOLA, M., PIRONTI, A.. *Magnetic Control of Tokamak Plasmas*. Springer, 2016.

[11] Lichtenberg A.J., Lieberman M.A.. *Regular and Chaotic Motion*, 2nd Ed. Springer Verlag, 1992.

[12] TOWNSEND, J. *The Conductivity produced in Gases by the Motion of Negatively-charged Ions*. Nature **62**, 340–341 (1900). https://doi.org/10.1038/062340b0

[13] SINHA, J..Thesis nº 7925, Swiss Plasma Center - École Polytechnique Fédérale de Lausanne, *Plasma breakdown and current formation in sigle core and doublet configurations on TCV*

[14] SAUTER, O. *et al. Neoclassical conductivity and bootstrap current formulas for general axisymmetric equilibria and arbitrary collisionality regime*. Physics of Plasmas, 6(7):2834–2839, 1999. http://scitation.aip.org/content/aip/journal/pop/6/7/10.1063/1.873240.

[15] Cheetham A.D., Heym A. *et al. The TCA Tokamak - project report 1979. Infoscience EPFL scientific publications*. Avaliable from: https://infoscience.epfl.ch/record/120713

[16] BITTENCOURT, J. A.. *Fundamentals of plasma physics*. New York: Springer Verlag,2004.

[17] JARDIN, S..*Computational Methods in Plasma Physics*. Chapman & Hall/CRC Computational Science Series

[18] ATINKSON, K. E.. *An introduction to numerical analysis*. John Wiley & Sons, 1989.

[19] SAUTER, O. *Geometric formulas for system codes including the effect of negative triangularity*, Fusion Engineering and Design 112 (2016) 633–645.

[20] WEISEN, H., MARTIN, Y. and MORET J.-M., "*On the dependence of energy confinement on elongation in single null plasmas*", Nucl. Fusion, vol. 42, p. L5, 2002.

[21] SNYDER, P. B., and WILSON, H. R.. *Ideal magnetohydrodynamic constraints on the pedestal temperature in tokamaks*. Plasma Physics and Controlled Fusion, 45(9):1671–1687, September 2003.

[22] FELICI, F. *et al. Real-time physics-model-based simulation of the current density profile in tokamak plasmas*. 2011 Nucl. Fusion 51 083052

[23] HOFMANN, F., *et al. FBT - A FREE-BOUNDARY TOKAMAK EQUILIBRIUM CODE FOR HIGHLY ELONGATED AND SHAPED PLASMAS*. 1988 Nuclear Fusion 28 1871